

Atomic X-ray Spectroscopy of Accreting Black Holes

D.A. Liedahl and D.F. Torres

Abstract: Current astrophysical research suggests that the most persistently luminous objects in the Universe are powered by the flow of matter through accretion disks onto black holes. Accretion disk systems are observed to emit copious radiation across the electromagnetic spectrum, each energy band providing access to rather distinct regimes of physical conditions and geometric scale. X-ray emission probes the innermost regions of the accretion disk, where relativistic effects prevail. While this has been known for decades, it also has been acknowledged that inferring physical conditions in the relativistic regime from the behavior of the X-ray continuum is problematic and not satisfactorily constraining. With the discovery in the 1990s of iron X-ray lines bearing signatures of relativistic distortion came the hope that such emission would more firmly constrain models of disk accretion near black holes, as well as provide observational criteria by which to test general relativity in the strong field limit. Here we provide an introduction to this phenomenon. While the presentation is intended to be primarily tutorial in nature, we aim also to acquaint the reader with trends in current research. To achieve these ends, we present the basic applications of general relativity that pertain to X-ray spectroscopic observations of black hole accretion disk systems, focusing on the Schwarzschild and Kerr solutions to the Einstein field equations. To this we add treatments of the fundamental concepts associated with the theoretical and modeling aspects of accretion disks, as well as relevant topics from observational and theoretical X-ray spectroscopy.

PACS Nos.: 32.30.Rj, 32.80.Hd, 95.30.Dr, 95.30.Sf, 95.85.Nv, 97.10.Gz, 97.80.Jp, 98.35.Mp, 98.62.Mw

1. Introduction

The publication of Einstein's General Theory of Relativity (GR) in 1915 was the culmination of several years of effort that began as early as 1907, when Einstein began to address the incompatibility between the Special Theory of Relativity and Newtonian gravitation. The nature of the inconsistency is clear. For example, Newton's formulation of gravitation is embodied in the Poisson equation for the gravitational potential, $\nabla^2\phi = 4\pi G\rho$, where the source term ρ is the mass density, and it is implied that the field responds instantaneously to changes in ρ , thereby violating special relativity. To Einstein, this inconsistency foreshadowed a complete revision of gravitation theory.

For a relativistic theory of gravity, the characteristic length scale for physical effects near a mass M , on dimensional grounds, is GM/c^2 , which is known as the *gravitational radius*. In assessing the magnitude of GR effects in the vicinity of a mass M , at a distance r from the mass, one compares r with this characteristic length scale. Therefore, we expect only small perturbations to Newtonian physics whenever $GM/rc^2 \ll 1$. This is just the case for the first proposed tests of GR, and in fact, for

D.A. Liedahl. Lawrence Livermore National Laboratory, 7000 East Ave, L-473, Livermore, CA 94550, U.S.A.
D.F. Torres. Lawrence Livermore National Laboratory, 7000 East Ave, L-413, Livermore, CA 94550, U.S.A.

all possible terrestrial and solar system experiments. Most notable were the problem of the precession of the perihelion of Mercury and the prediction of the bending of starlight as it grazed the Sun. In both cases, $GM/rc^2 \ll 1$, and the magnitude of the effects are indeed subtle.

The advance of Mercury's perihelion is 574 arcseconds per century, only 43 of which are left unexplained by Newton's $1/r^2$ law after accounting for perturbations of Mercury's orbit caused by the other planets. In 1914, using the nearly completed GR theory, Einstein found that the rate of advance of the perihelion $\Delta\omega \approx (3GM/c^2 r_{\text{orbit}}) \omega_{\text{orbit}}$, which works out to 43 arcseconds per century. Einstein was thus able to account for a discrepancy that had been known for sixty years, and was delighted, being moved to exclaim:

For a few days, I was beside myself with joyous excitement.

The quantitative confirmation of the deviation of a ray of Sun-grazing starlight brought worldwide acclaim to Einstein (an authoritative discussion can be found in [1]). In 1911, again before the final version of GR was in hand, Einstein predicted that the deflection should amount to $2GM/R_{\odot}c^2 = 0.87$ arcsec, where R_{\odot} is the radius of the Sun. This result could not have been especially satisfactory to Einstein, since it can be derived from Newtonian mechanics, if one assumes that light is corpuscular, composed of particles with a mass equivalent E/c^2 . The result is referred to as the “Newton value,” and is one half of the revised value derived by Einstein in 1915 (1.74 arcsec). In 1919, the result of a measurement of the deflection that confirmed Einstein's prediction was announced to the Prussian Academy, after which Einstein's reputation soared, both inside and outside academic circles, and the notions of warped space and time – warped spacetime – found their way into mainstream physics.

The revolutionary implications of GR forced dramatic revisions of the concepts of space and time, not the least of which was the abandonment of the action-at-a-distance model of gravity. By contrast, the applications of GR in the early 1900s could be regarded as subtle corrections to Newtonian theory. However, discoveries of the 1960s — the discovery of compact X-ray binary sources [2], the recognition of the nature of quasars [3], and the discovery of radio pulsars [4] — provided examples of environments for which general relativity constituted substantially more than a gentle correction to Newtonian physics.

The succession of rapid-fire astronomical discoveries of the 1960s marks the birth of relativistic astrophysics. Perhaps the most remarkable idea to present itself during that era was that black holes could exist in nature. In §2, a brief history of the black hole concept is presented. Here, we remark only that, in 1916, only a few months after Einstein published his final version of GR, Karl Schwarzschild discovered the solution to the field equations corresponding to the exterior of a spherically symmetric mass distribution. This solution is the starting point for the study of black holes. Prior to the 1960s, however, references in the scientific literature to what eventually came to be called black holes were sporadic and met with skepticism.

Taken alone, GR does not prescribe a minimum black hole mass. However, those objects currently identified as black holes are believed to have formed from the catastrophic collapse of massive stars, and, combining GR with the equations of stellar structure, a minimum mass of about $3M_{\odot}$ is required [5] [6]. According to GR, a classical theory, matter undergoing gravitational collapse to form a black hole is crushed inexorably until it ends up in a point, known as the *singularity*. The singularity is enshrouded by a mathematical surface known as the *event horizon*, within which matter and light are trapped, destined to merge with the singularity. The event horizon has a radius $2GM/c^2$ (about 3 km per solar mass), if the black hole is not spinning. The event horizon can be as small as GM/c^2 , in the case of a black hole spinning at its maximum rate. A black hole is a simple object, in the sense that spacetime outside its event horizon can be described entirely by its mass, spin, and charge. Therefore, black holes belong to a three-parameter family – absurdly simple compared to, say, main-sequence stars. And yet, black holes so violate one's physical intuition that even Einstein doubted that they could exist in nature. In the words of Igor Novikov [7]:

Of all conceptions of the human mind perhaps the most fantastic is the black hole. Black holes are neither bodies nor radiation. They are clots of gravity.

Outside the event horizon, the behavior of matter is dictated, in part, by the spacetime geometry. If radiating matter of sufficient quantity exists near the event horizon of a black hole, such that it is observable at Earth, then some of the effects of warped spacetime are observable, and we gain experimental access to physical environments for which GM/rc^2 is not negligibly small. This regime is known as the *strong field limit*, where relativistic effects are of fundamental importance. Nature has obliged us, by providing (at least) two classes of black hole systems – black hole X-ray binaries and active galactic nuclei (AGN) – in which prodigious quantities of matter are flowing “onto” the black hole, resulting in the release of copious electromagnetic radiation. In fact, detections of X-ray line radiation from regions where $GM/rc^2 \approx 1$ have been claimed.

The flow of material referred to above is called *accretion*, defined as the capture of matter by an object’s gravitational field, where it is presumed that the fate of the captured material is coalescence with the gravitating body, or, in the black hole case, passage through the event horizon. The physics of accretion has been an active area of research for over three decades. For the purposes of this paper, the importance of accretion is tied primarily to the role it plays in the conversion of gravitational potential energy into radiation. Owing to the prevalence of angular momentum in the cosmos, accretion often involves a disk. Accretion disks provide the means by which to dissipate angular momentum, allowing accretion, which is accompanied by the release of energy. The extraction of energy is especially efficient if the inner edge of the accretion disk extends to small radii, so that the ratio M/R_{inner} is large. This is the case for accretion onto compact objects – white dwarfs and, especially, neutron stars and black holes. The luminosities of the accreting compact objects that populate the Milky Way Galaxy range as high as $\sim 10^5 L_{\odot}^1$, while AGN can exceed that by seven, eight, even nine orders of magnitude [9].

Accretion disks present a number of theoretical challenges. The complexity of the problem, if one hopes eventually to work from first principles, is suggested by S. Shapiro and S. Teukolsky [10]:

In the general accretion case, one must solve the time-dependent, multi-dimensional, relativistic, magneto-hydrodynamic equations with coupled radiative transfer!”

Given the context of the earlier parts of this section, the above quote begs the question as to whether or not the strong field regime of GR can be tested through studies of accreting black holes. Considering that accretion onto black holes is one of the dominant light-producing mechanisms in the Universe, developing reliable working models of disk accretion is, from the astrophysics standpoint, likely to be considered a higher priority than testing GR, although the latter is certainly a long-term goal. Moreover, it is probably fair to say that, *at present*, discerning possible inadequacies in strong field GR, a “clean” theory, using “messy” accretion disk models is problematic. In the meantime, recognizing that GR has stood up to every test to which it has been subjected, the theory in full is generally taken as being correct, and incorporated into the array of theoretical tools used to study black hole accretion.

Accretion-powered objects are bright X-ray sources [2] [11]. The observed variability of the X-ray flux [12] [13] [14], rapid compared to variability at longer wavelengths, implies that X rays are produced preferentially in the inner regions of the disk.² The X-ray continuum spectra vary from source to source, and can vary in time as well, but for our purposes it is adequate to think of accreting black holes as exhibiting power-law continua that extend up to hard X-ray energies (\sim hundreds of

¹ The symbol \odot refers to the standard solar value of the subscripted quantity. Throughout the paper, we refer to the mass, radius, and bolometric luminosity of the Sun – $M_{\odot} = 1.99 \times 10^{33}$ g; $R_{\odot} = 6.96 \times 10^{10}$ cm; $L_{\odot} = 3.9 \times 10^{33}$ erg s⁻¹ [8].

² The time scale for appreciable variations in the observed flux is associated with the light-crossing time of the source, so that the linear extent of the source is given by $R \sim ct_{\text{cross}}$.

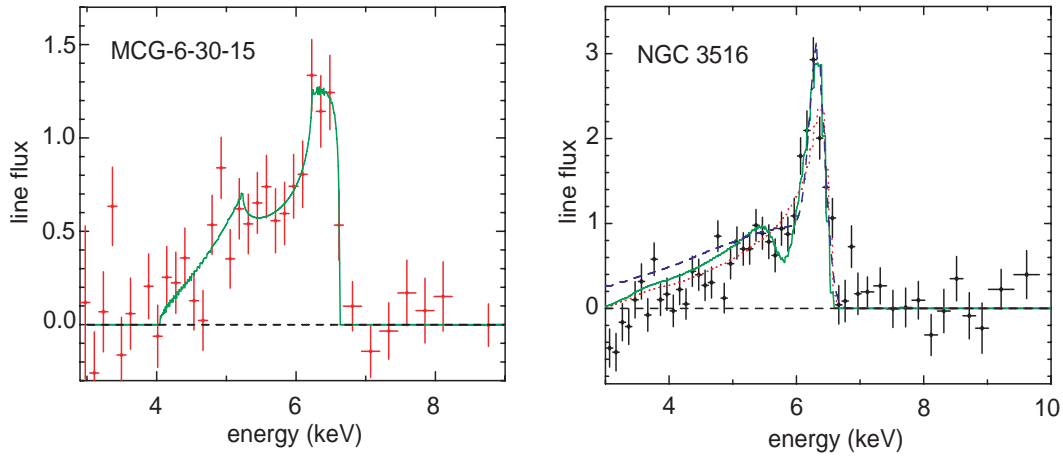


Fig. 1. Broad iron $K\alpha$ emission from two Seyfert 1 galaxies: MCG–6-30-15 (*left panel*) [26] and NGC 3516 (*right panel*) [126] as recorded with the ASCA Solid-State Imaging Spectrometer (*crosses*) following subtraction of a continuum model. The line flux is scaled in multiples of 10^{-4} photons $\text{cm}^{-2} \text{s}^{-1} \text{keV}^{-1}$. Line profiles consist of a narrow emission component at 6.4 keV, the approximate rest energy of near-neutral iron ions, and a broad redshifted wing, believed to result from relativistic effects within a few gravitational radii of a supermassive black hole. Figures courtesy of K. Nandra (see [20]).

keV) [15] [16]. If an optically thick accretion disk surrounds the compact object, and if the X-ray continuum flux irradiates the disk, then spectral signatures of the interaction of the X-ray continuum and the disk are expected to imprint themselves on the overall spectrum [17] [18] [19]. This imprinting is known as “reflection.” Among the expected reflection features are a blend of X-ray lines from iron lying in the 6.4-7.0 keV spectral range. These lines are produced as the result of $1s$ photoionization of multi-electron iron ions. It was also shown that, if the iron lines are generated very near a black hole, relativistic effects will skew the line, i.e., relativistic Doppler effects would broaden the line to several $\times 10,000 \text{ km s}^{-1}$, and the gravitational redshift would produce observed emission down to several hundred to a few thousand eV below the rest energy (see Fig. 1), depending on the radial extent of the disk and its inclination with respect to the plane of the sky [21]. Precedence for the possibility of observing relativistic effects in emission lines was set by observations of the elliptical galaxy Arp 102B in the visible band, where the shapes of $H\alpha$ and $H\beta$ emission lines were analyzed in the context of a relativistic accretion disk model [22]. Broad X-ray iron line emission was detected in the Galactic black hole X-ray sources Cyg X-1 [23] and 4U1543-47 [24], possibly implying relativistic broadening, although the poor spectral resolution available at that time made definitive conclusions problematic. Alternative mechanisms for producing broad lines were shown to be unlikely [25]. The breakthrough observation was that of the Seyfert 1 galaxy MCG–6-30-15, using the ASCA observatory, which exhibited evidence for highly-broadened and skewed iron line emission [26] [27].

The discovery of skewed iron line emission has motivated a great deal of theoretical research, and has intensified observational searches for more and better X-ray data of black hole systems. By the current paradigm of black hole accretion disks [28], the study of iron line emission from the inner orbits of the accretion disk surrounding black holes provides the most direct view of the region within a few gravitational radii of the central engine. Our intention is to provide a primer covering the three topics that unite this phenomenon: (1) black holes; (2) accretion theory and modeling; and (3) X-ray spectroscopy and spectral modeling. Having here presented a quick synopsis, in the following sections each is elaborated in turn. It is fair to note that the relativistic disk interpretation is not unanimously accepted. Not surprisingly, with far-reaching consequences at stake, alternative models for producing

the broadened line have been and are being investigated (e.g., [29], [30]). However, a comparison of the successes and failures of the various models would take us too far afield, and we focus here on the relativistic disk interpretation.

We also omit from detailed discussion the subjects of aperiodic and quasi-periodic variability in the X-ray emission from black hole systems, subjects that are extremely rich from a phenomenological standpoint, as evidenced by data collected with the *Rossi X-ray Timing Explorer (RXTE)*. In black hole X-ray binary systems, the observed time scales for variability are of the same order as the dynamical time scales expected for accretion flows near the black hole. Therefore, the temporal behavior of the X-ray emission provides another powerful view of the relativistic dynamics associated with the inner accretion disk. Although studies of the timing properties of black hole systems have, for the most part, constituted a somewhat “orthogonal” approach relative to spectroscopic analysis, there is a great deal of potential in analyzing the X-ray behavior of accreting black holes in the spectral and temporal domains when measured simultaneously. For reviews, see [13] [31] [32].

We have endeavored to provide the reader with a sufficient number of references to begin an exploration of the literature, but we make no claim of unbiased completeness. The collection of papers cited is a reflection of our own experience with the subject matter. We note that excellent reviews of this topic have recently appeared [33] [34]. We take a more tutorial approach in this paper, and hope that readers will find our paper to be complementary, although there is some unavoidable overlap.

The organization of the paper is as follows: In §2 we briefly sketch the historical development of the black hole concept, from Michell’s dark star to Schwarzschild’s solution of Einstein’s field equations to the golden age of theoretical black hole research. Properties of the two size classes of black holes that are convincingly established – stellar-sized and supermassive – are outlined in §3. Also in that section we comment on the more speculative intermediate-mass black holes, and the microquasar phenomenon. A few of the core concepts associated with accretion power are treated in §4, including the α -disk model and the concept of accretion efficiency. In our treatment of general relativity, we forego a treatment of the theory proper, and instead focus on a few of the applications relevant to line spectroscopy of accreting black holes, including the implications of both the Schwarzschild (§5) and Kerr (§6) solutions. These include the gravitational redshift, the nature of circular orbits, and light motion. Vertical structure calculations of accretion disk atmospheres and the basic atomic physics processes that give rise to iron K spectra are the subjects of §7. Topics here include X-ray photoionization codes, the X-ray fluorescence mechanism, the fluorescence yield, resonant Auger destruction, and X-ray reflection. We conclude in §8.

2. History of the Black Hole Concept

Given the association of black holes with Einstein’s GR, it might be natural to conclude that the notion of objects from which light cannot escape was engendered by 20th Century physics. However, allusions to the idea were already around hundreds of years earlier. In 1676, Olaus Roemer, noting variations in the period of Jupiter’s moon Io, discovered that the speed of light is finite. In 1728, James Bradley, through observations of stellar aberration, produced further confirmation and a more accurate value of the speed of light, $295,000 \text{ km s}^{-1}$. The concept of escape velocity, which, for a spherical mass M of radius R , is $v_{\text{esc}} = (2GM/R)^{1/2}$, was present in Newton’s time. In 1783, the English geologist John Michell combined these previous pieces of information, and realized that it would be theoretically possible for gravity to be so overwhelmingly strong that nothing – not even light – could escape. Michell’s statements were made in the context of a corpuscular theory of light, the in-vogue approach at the time:

Suppose the particles of light to be attracted in the same manner as all other bodies...[then] there should exist in nature bodies from which light could not arrive at us.

Michell went further, and proposed that from the motion of companion stars³

... we might still perhaps infer the existence of the central objects with some degree of probability.

Michell's objects were dubbed *dark stars*. Pierre Simon Laplace published similar comments in his 1795 *Exposition du Systeme du Monde*, and added that

... it is therefore possible that the greatest luminous bodies in the Universe are on this account invisible.

Late 19th Century experiments fueled the rise of quantum mechanics and the wave interpretation of light, and the ideas of dark stars were soon forgotten.

The mathematical discovery that would lead to the modern concept of the black hole was introduced in 1916, as the first solution to Einstein's field equations. At the outbreak of World War I, in August 1914, Karl Schwarzschild volunteered for military service. He served in Belgium as commander of a weather station, in an artillery unit in France calculating missile trajectories, and in Russia. During this time he wrote two papers on Einstein's relativity theory (and one on Planck's quantum theory, explaining the splitting of the spectral lines of hydrogen by an electric field – the Stark effect). Einstein was later to say of Schwarzschild's work:

I had not expected that one could formulate the exact solution of the problem in such a simple way.

Regrettably, while in Russia, Schwarzschild contracted a fatal disease and went home to die at the age of 42, never believing in the physical nature of what his solution implied for dark stars. In fact, a back-of-the-envelope calculation shows that for an object to exist within a sphere of radius $2GM/c^2$, its mean density must satisfy $\bar{\rho} > 3c^6/32\pi G^3 M^2$, or $\bar{\rho} > 10^{16} \text{ g cm}^{-3}$ for a stellar-mass object, which must have seemed absurd at that time.

With the end of the First World War, further astronomical tests of general relativity led to popular and scientific interest in Einstein's ideas. Most notable was an expedition led by Arthur Eddington, the goal of which was to obtain a measurement of the bending of starlight by the Sun during a solar eclipse. Meanwhile, research on stellar structure and evolution thrived during these years. In 1930, S. Chandrasekhar computed the first white dwarf models, taking into account special relativistic effects in the degenerate electron equation of state, based on the Fermi-Dirac statistics introduced in 1926, and on the ideas of W. Fowler regarding the equilibrium between electron degeneracy pressure and gravity. Chandrasekhar discovered that no white dwarf could sustain a mass larger than $1.4M_{\odot}$. It was apparent that if the electron degeneracy cannot withstand gravity, further collapse is inevitable.

In 1934, W. Baade and F. Zwicky predicted that this further collapse would strip the atoms of their electrons, packing the nuclei together, while forming a neutron star. These stars were expected to be about 10 km in diameter, but with densities on the order of a billion tons per cubic inch. The neutron had been discovered by Chadwick only two years earlier. In this same work, Baade and Zwicky coined the term *supernova* and introduced its concept. In acknowledgement of one of the most prescient papers ever written, even the comic strip of the *Los Angeles Times* would comment on the issue. Zwicky would later say of this insert:

This, in all modesty, I claim to be one of the most concise predictions ever made in science. More than thirty years were to pass before the statement was proved to be true in every respect.

³ Michell is credited with the idea of binary stars.

In 1939, Oppenheimer and Volkoff [35], and, a few months later, Oppenheimer and Snyder [36] realized that this inevitable stellar collapse implies a stellar evolutionary scenario for the formation of black holes. In the first paper, the first detailed calculations of the structure of neutron stars were performed, establishing the foundation of the general relativistic theory of stellar structure. The second paper focused on the collapse of a homogeneous sphere of a pressure-free fluid using general relativity. Oppenheimer and Snyder's star was precisely spherical, non-spinning, non-radiating, uniform in density, and with no internal pressure. It was this set of assumptions, perhaps, that gave rise to skepticism regarding the applicability of the results to real imploding stars. The most impressive prediction in the Oppenheimer and Snyder work was the fact that an external observer – one far from the star – would see the implosion come to a halt at the event horizon, whereas one riding with the falling material would witness the whole process to the end, finding herself drawn into a point of infinite density, notwithstanding the meager hopes of surviving the trip until contact with the singularity. They concluded:

When all thermonuclear sources of energy are exhausted, a sufficiently heavy star will collapse. Unless [something can somehow] reduce the star's mass to the order of that of the sun, this contraction will continue indefinitely.

These discoveries in the field of stellar evolution directed attention to the Schwarzschild model of the spacetime exterior to a star. But yet again, a new world war would soon divert the efforts of most scientists towards military and nuclear research. Work on black hole physics recommenced in the mid-1950s, when D. Finkelstein discovered an alternative coordinate system for the Schwarzschild geometry that helped to clarify the Oppenheimer and Snyder results as being caused by time dilation in a gravitational field. J. A. Wheeler, first an opponent of the black hole concept, began to accept it, and tried to construct a quantum mechanical view of the inner singularities. Finally, Kerr discovered the spinning black hole solution to the Einstein field equations in 1963 [148].

The term “black hole” was introduced in 1967 by Wheeler. In a 2003 interview with P. Davies, he explains his choice:

The occasion was a meeting in the fall of 1967 at the Institute of Space Studies in New York to consider this marvelous work of Jocelyn Bell and Anthony Hewish on the pulsars. What could be the cause of these absolutely regular pulses from some object out in space, and one obvious possibility was vibration of a white dwarf star, another was the rotation of a neutron star. But then I thought that to keep one's mind open, to look at all the possibilities one ought really to look at the gravitationally completely collapsed object. Well, the very words sounded so foggy, so ethereal, so far from touchability that nobody resonated to that as a possibility to be investigated. So in desperation I adopted the words Black Hole. Well, here at least was a name.

The golden age of theoretical research in black hole physics started in 1964, and was to last for at least a decade. In this decade, computer codes used in hydrogen bomb research were adapted to study stellar collapse, topological methods and thermodynamical ideas were introduced into the study of black holes, the “no hair theorem” was demonstrated (a black hole has no characteristics indicative of the star from which it came, and that only three parameters – mass, angular momentum, and charge – are needed to describe it), and the cosmic censorship conjecture was stated (there are no naked singularities, but rather, they are dressed with horizons), among many other results. After 1975, whereas important theoretical progress was still being made, the field slowly started to be dominated by an astronomical search for black holes in the Universe, at all scales. By that time, there were ample astrophysical reasons to expect objects described by solutions to Einstein's field equations to become part of the ontology of the Universe.

3. Accretion Power

Accretion is defined as the capture of matter by an object's gravitational field, where it is presumed that the fate of the captured material is coalescence with the gravitating body, the results of which are an increase in the object's mass, as well as the conversion of gravitational potential energy into other forms. The introduction of accretion flows into astrophysics is often traced to the 1939 paper by Hoyle and Lyttleton [37]. Interestingly, its title is "The Effect of Interstellar Matter on Climatic Variations," which examined the possibility that variable accretion of interstellar clouds by the Sun could be linked to the Ice Epochs of Earth's deep geological past. The notion of accreting black holes lay more than two decades in the future. The astronomical discoveries of the 1960s provided impetus for the rapid development of accretion theory, currently an active area of astrophysical research. We provide here a brief sketch of the theory as it pertains to our subject matter. A collection of seminal papers on the topic can be found in [38]. For a comprehensive textbook introduction to the physics of accretion, see [39]. An up-to-date review article, with a pedagogical approach, can be found in [40].

3.1. Basic Concepts

To impart the fundamentals of accretion physics, we start with the Newtonian view of gravitation and a neutron star onto which matter falls. A test mass m that free falls from rest at "infinity" and comes to rest on the surface of a star of mass M and radius R , loses an energy GMm/R , which, for the purposes of this discussion, we assume to be converted into radiation. Therefore, given a more-or-less steady infall of matter, the energy generation rate — the accretion luminosity — is $L_{\text{acc}} = GM\dot{M}_{\text{acc}}/R$, where \dot{M}_{acc} is the mass accretion rate, the dot denoting differentiation with respect to time. It is sometimes convenient to express L_{acc} in a special relativistic context, treating the energy release per unit time as being equivalent to a conversion of rest mass energy into radiation per unit time. Thus $L_{\text{acc}} = \eta\dot{M}_{\text{acc}}c^2$, where η is the dimensionless *accretion efficiency*. For the case of a spherical star, as discussed here, $\eta = GM/Rc^2$. The appearance of relativistic correctness implied by the adornment of these last two expressions with factors of c^2 is entirely artificial, since the derivation of the accretion luminosity was obtained with purely Newtonian physics. Later, however, we will see that expressing L_{acc} in terms of η follows quite naturally in the general relativistic context, and we continue to use η to relate L_{acc} to \dot{M}_{acc} .

Matter in an accretion flow is subject not just to gravitational forces, but to radiation forces, as well. The radiation produced near the surface of the accreting object exerts a pressure on the accretion flow. For radiation emerging from a gravitating source in a frequency interval $d\nu$, the force on a particle at distance r , in terms of an interaction cross-section $\sigma(\nu)$, is

$$F_{\text{rad}} = \int_0^\infty d\nu \frac{L_\nu}{4\pi r^2 h\nu} \frac{h\nu}{c} \sigma(\nu), \quad (1)$$

where $L_\nu/4\pi r^2 h\nu$ is the areal rate at which photons in the frequency range $[\nu, \nu + d\nu]$ arrive at r , and $h\nu/c$ is the photon momentum. Thomson scattering sets the baseline for this integral, so that, ignoring relativistic corrections to the Thomson cross-section σ_T , the net force, including gravity, is

$$F = \frac{\sigma_T L}{4\pi cr^2} - \frac{GMm_p}{r^2} \quad (2)$$

assuming for simplicity a fully ionized hydrogen plasma (m_p is the proton mass). For accretion to proceed, we must have $F < 0$, which imposes an upper limit to the accretion luminosity, known as the *Eddington luminosity*, which is given by

$$L_E = \frac{4\pi Gm_p c M}{\sigma_T} = 1.3 \times 10^{38} \frac{M}{M_\odot} \text{ erg s}^{-1}. \quad (3)$$

By the same reasoning, there is an upper limit to the mass accretion rate. From the relation defining the proportionality between L and \dot{M} , $L = \eta \dot{M} c^2$, we define the *Eddington accretion rate*,

$$\dot{M}_E = \frac{4\pi G m_p M}{\eta c \sigma_T} = 1.4 \times 10^{18} \left(\frac{\eta}{0.1} \right)^{-1} \frac{M}{M_\odot} \text{ g s}^{-1}. \quad (4)$$

If a black hole accretes matter at the Eddington rate, then its growth rate $dM_{\text{BH}}/dt \propto M_{\text{BH}}$, and the mass grows exponentially with time, with an e -folding time $\tau_{\text{growth}} = \eta c \sigma_T / 4\pi G m_p \sim 5 \times 10^7 \text{ yr}$, if $\eta = 0.1$.

Perhaps the simplest model of mass transfer in an X-ray binary system, to the extent that it is straightforward to obtain order-of-magnitude estimates, is that pertaining to a *high-mass X-ray binary* (HMXB). A more detailed description can be found in [41]. In HMXBs, a high-mass (O or B) star, radiates a bright UV continuum that transfers momentum to the stellar atmosphere through absorption in resonance lines, thus driving a mass outflow, or a stellar wind. In close proximity to the OB star is a neutron star, which captures part of the wind. In order to obtain numerical values of various quantities, we assume here that the mass of the neutron star is $1.4 M_\odot$, and that its radius is 10^6 cm , so that $\eta = 0.21$. A simple estimate of the rate at which mass is captured by the neutron star can be found by finding the distance r_{acc} at which the wind kinetic energy per unit mass, determined by the wind velocity v_w , is equal to the gravitational potential associated with the neutron star. This gives the *accretion radius*, $r_{\text{acc}} = 2GM/v_w^2$. Since the neutron star accretes at the rate $\dot{M}_{\text{acc}} = \pi r_{\text{acc}}^2 \rho_w v_w$, we can determine the accretion luminosity once we know the wind mass density ρ_w at the position of the neutron star. This can be estimated by a mass continuity equation, assuming that the wind is spherically symmetric with respect to the OB star: $\dot{M}_w = 4\pi a^2 \rho_w v_w$, where \dot{M}_w is the total mass loss rate of the star, and a is the separation between the centers of mass of the components of the binary. Putting all this together, we find

$$\dot{M}_{\text{acc}} \sim \left(\frac{GM}{av_w^2} \right)^2 \dot{M}_w = 2 \times 10^{16} a_{12}^{-2} (v_w)_8^{-4} (\dot{M}_w)_{-6} \text{ g s}^{-1}. \quad (5)$$

To obtain the numerical estimate, we have written the various quantities in terms of multiples of typical values for those quantities: a_{12} is the binary separation expressed as $a/(10^{12} \text{ cm})$; $(v_w)_8$ is the wind velocity expressed as $v/(10^8 \text{ cm s}^{-1})$; $(\dot{M}_w)_{-6}$ is the mass loss rate expressed as $\dot{M}_w/(10^{-6} M_\odot \text{ yr}^{-1})$.

In obtaining an estimate of the mass accretion rate in a typical HMXB, there is no reason we could not have substituted a black hole for the neutron star. But let us now proceed to determine the resulting luminosity and radiation temperature. Using $\eta = 0.21$, derived above for the neutron star case, the rate of mass accretion found in Eq. (5) results in a luminosity $L_{\text{acc}} \sim 10^{36} \text{ erg s}^{-1}$, or approximately $10^3 L_\odot$. An order-of-magnitude estimate (actually a lower bound) of the radiation temperature associated with the accretion luminosity can be obtained by assuming that the radiant energy takes the form of a blackbody. If the energy is released uniformly over a spherical surface of radius R , which we assume to coincide with the neutron star surface, then $L_{\text{acc}} = 4\pi R^2 \sigma T_{\text{bb}}^4$, where σ is the Stefan-Boltzmann constant. Thus we find $T_{\text{bb}} = (GM\dot{M}_{\text{acc}}/4\pi\sigma R^3)^{1/4}$, or, again in terms of typical system parameters,

$$T_{\text{bb}} = 3.2 \times 10^7 (v_w)_8^{-1} a_{12}^{-1/2} (\dot{M}_w)_{-6}^{1/4} \text{ K}, \quad (6)$$

which implies that the emission peaks in the X-ray band.

The simple model described above is consistent with observations of typical HMXBs. Is this model, on the other hand, relevant to black hole systems? For example, is it valid to simply evaluate η for a black hole by inserting, say, $R = 2GM/c^2$ into $\eta = GM/Rc^2$, i.e., $\eta_{\text{BH}} = 0.5$? Clearly, the answer must be “no,” since the calculation of η for a neutron star is based upon the assumption that the matter comes to rest on a material surface. In the cold fluid approximation, as used above, we might expect all of the energy release in black hole accretion to occur below the event horizon, leaving $\eta = 0$. In a more

realistic treatment, one assumes a finite gas temperature, and includes thermal energy balance in the calculations. Some fraction of the accretion energy is radiated away before crossing the event horizon. Such a scenario applies to accretion of the interstellar medium by an isolated black hole. Detailed calculations [42] show, however, that for an ambient ISM density and temperature of 1 cm^{-3} and 10^4 K , respectively, the efficiency $\eta \sim 10^{-10}$, and the expected luminosity is expected to be only $\sim 10^{21} \text{ erg s}^{-1}$ per solar mass of the accretor, far too dim to be observed (cf., [43] [44]). The inefficiency of spherical accretion by a black hole is borne out by the realization that, in spite of the large number of black holes postulated to populate the Milky Way Galaxy, only the merest fraction (perhaps 1 in 10^7) has been identified.⁴

In acknowledging that radial accretion onto a black hole is unlikely to produce a light source sufficiently bright that it is observable at Earth, we turn instead to accretion via a disk. We will see that disk accretion can be an extraordinarily efficient means by which to extract energy from matter near a black hole.

3.2. Accretion Disks

Angular momentum favors the formation of disks around accreting masses. The surfaces of constant gravitational potential between two stars in a binary system are such that a saddle point forms on the line of centers (the imaginary line connecting the centers of mass) between the two stars. The equipotential surface that intersects this saddle point is called the *Roche lobe*. If matter from one star reaches this saddle point, known as the inner Lagrangian point, or L1, then it can accrete onto the other star. Since there is relative motion between the stars, however, the overflowing matter cannot strike the accreting star directly, but rather goes into an orbit [45] dictated by its specific angular momentum. If sufficiently large quantities of matter spill through L1, however, these orbits cannot persist. Instead, collisions result in loss of energy and circularization of the orbits. Viscosity spreads the disk, transporting angular momentum outward and matter inward. This model describes the mass transfer mechanism in X-ray binaries, a pair of stars in close orbit, one of which is a gravitationally collapsed object — a neutron star or a black hole. The mass donor star is known as the companion. The X-ray binary phase of a Roche lobe overflow system is initiated when the companion expands to fill its Roche lobe, a consequence of normal stellar evolution [46]. The accretion of matter, if the overflow rate is sufficiently large, can power a highly luminous X-ray source. In this case, however, as contrasted to the HMXB case, the disk itself radiates much of the luminosity, irrespective of the presence of a material surface at the gravitating center.

Disk accretion by Roche lobe overflow was first invoked to explain cataclysmic variable systems [47], in which a normal star transfers mass to a white dwarf ($R_{\text{wd}} \sim 10^9 \text{ cm}$) in a close binary system. The fundamental theoretical aspects of accretion disks in X-ray binaries were worked out by Pringle and Rees [48] and by Shakura and Sunyaev [49]. The latter authors derived an analytic model of disk flow, where the viscously dissipated energy is assumed to be locally radiated as blackbody emission, with temperature given by

$$T_{\text{bb}}(r) = \left[\frac{3GM\dot{M}}{8\pi\sigma r^3} (1 - \sqrt{R_*/r}) \right]^{1/4}, \quad (7)$$

where R_* is the radius of the accretor, or, in the black hole case, R_* is the innermost stable circular orbit of disk material (see §6). Equation (7) is similar to the expression derived for HMXBs, showing that, for similar parameters, X-ray-emitting temperatures are expected. The energy dissipated per unit

⁴ By “identified,” we mean “inferred.” The designation *black hole candidate* is applied when alternative explanations do not suffice.

area is

$$Q(r) = \frac{3GM\dot{M}}{8\pi r^3} (1 - \sqrt{R_*/r}), \quad (8)$$

from which Eq. (7) follows. The disk luminosity L_{disk} can be found by integrating $Q(r)$ over both disk faces, from R_* to some outer radius R_{outer} . A good approximation for L_{disk} is found by letting $R_{\text{outer}} \rightarrow \infty$, yielding the result $L_{\text{disk}} = GMM/2R_*$ [39]. If the accretor has a solid surface, the remainder of the energy is dissipated as it comes to rest on the surface. If the accretor is a black hole, then the remainder simply disappears behind the event horizon. In this latter case, if the black hole does not spin, the inner disk radius is taken to be $6GM/c^2$ (see §5), which gives $L_{\text{acc}} = \dot{M}c^2/12$. i.e., $\eta \approx 0.083$. For a black hole spinning at its theoretical maximum rate, we set $R_* = GM/c^2$, which gives $\eta = 0.5$. In §5 and §6, we derive relativistically correct values for the accretion efficiencies of non-spinning and spinning black holes, respectively.

In terms of accretion disk dynamics, the essential breakthrough introduced by Shakura and Sunyaev [49] was the α -prescription, a parameterization of the vertically-averaged stress that assumes it can be written as αP , where P is the vertically-averaged total pressure in the gas (gas pressure plus radiation pressure), and where α is a constant. The α -prescription permits the solution of the coupled set of eight equations that determine the disk structure. Although the α -prescription sidesteps a good bit of complex physics, it turns out that many results are fairly insensitive to the value of α . For example, the disk central temperature, i.e., $T(r, z = 0)$, is proportional to $\alpha^{-1/5}$, whereas, Eqs. (7) and (8) show that some results of interest have no dependence at all on α . For this reason, the α -disk has seen wide use. Indeed, the optically thick α -disk model has been accepted with only a few modifications since its inception in 1973 ([50] [51]; [52]). Among these modifications are the development of various branches of self-consistent accretion flow solutions such as advection-dominated accretion flows [53] [54] that successfully describe the spectral behavior of black hole XRBs [55] [56], advection-dominated inflow/outflow systems [57], and convection-dominated accretion flows [58]. Comparisons of the α -disk model with observations of X-ray binaries and AGN are presented in [39] and [59] [60], respectively. Modern accretion flow models are discussed in [61].

In spite of the successes and ease of use of the α -disk model, a physical understanding of α (or something like it) has been an important goal for accretion disk modelers, since it determines the essential mechanism that drives the transport of angular momentum. The viscous mechanism in accretion disks allows accretion to occur by transporting angular momentum outward, matter inwards, and by dissipating gravitational energy into heat inside the disk. The viscosity mechanism has been identified in theory as a magneto-rotational instability arising from the entanglement of magnetic fields caused by differential rotation of gas in Keplerian orbits [62]. In MHD models, this mechanism provides the energy dissipation and angular momentum transfer needed to naturally produce mass accretion with self-sustained magnetic fields B that are much smaller than the equipartition level ($B^2/8\pi \ll \rho v^2$), where ρ is the gas mass density and v is the thermal velocity. Numerical magnetohydrodynamic (MHD) models [63] show that α is not constant, but that it ranges from $\sim 10^{-3}$ – 10^{-1} .

While the X-ray continuum in accreting neutron star systems is interpreted, in part, as thermal emission from the disk, the presence of (apparently) non-thermal continuum radiation in these sources, and AGN, as well, is not naturally explained with the α -disk formalism. In fact, the high-energy emission is especially problematic in AGN, if we consider Eq. (7). Anticipating a result that is derived in §6, set $R_* = 6GM/c^2$, which corresponds to the inner disk edge in a non-spinning black hole, and express the mass accretion rate as a fraction f_E of the Eddington accretion rate, $\dot{M} = f_E \dot{M}_E$. Finally, if we express r as a multiple of the gravitational radius GM/c^2 , so that $x = c^2 r / GM$, then Eq. (7) can be written as

$$T_{\text{bb}}(x) = \left[\frac{3m_p c^5 f_E}{2\eta \sigma_T GM} \frac{(1 - \sqrt{6/x})}{x^3} \right]^{1/4}, \quad (9)$$

The key result to take away from this expression is the scaling $T_{\text{bb}}(x) \propto M^{-1/4}$. Thus if we accept the α -disk model for stellar-sized accreting black holes ($M_{\text{BH}} \sim 10M_{\odot}$), we are faced with a glaring inconsistency if we wish also to apply it to AGN ($M_{\text{BH}} \sim 10^7M_{\odot}$); all other things being equal, $T_{\text{bb}}^{\text{agn}}/T_{\text{bb}}^{\text{xrb}} = (M_{\text{BH}}^{\text{xrb}}/M_{\text{BH}}^{\text{agn}})^{1/4}$, which means that a 10^7 K blackbody for an X-ray binary is scaled down to about 3×10^5 K for an AGN disk. The AGN emission is thus expected to peak in the UV band, with very little luminosity appearing in the hard X-ray region. While the UV peak, the “big blue bump,” is a well known component of AGN spectra [64] [65], the α -disk model says nothing about the X-ray flux that characterizes AGN [66], and refinement is required in order to match disk models to observations. For example, a more realistic accounting of radiation transport effects in the disk atmosphere partially ameliorates this problem [67] [68] [69].

The favored explanation of the X-ray luminosity of accreting black holes posits that the blackbody component originates in a cold, optically thick accretion disk, whereas the hard X-ray power-law component is produced in an optically thin hot corona by thermal *Comptonization* of disk photons [70] [71]. Comptonization refers to the deformation of a radiation field as it interacts through Compton scattering with an electron distribution, where a self-consistent solution determines both the spectral shape and the electron temperature [72] [73] [74]. Constructing theoretical models of continuum production is complicated by the need to include $e^+ - e^-$ pair production in a manner that is self-consistent with the radiation field [75] [76] [77] [78].

In disk accreting systems where a hard X-ray source is present, the disk is exposed to this radiation and will be heated by it. In fact, radiative heating can exceed internal viscous heating in some regions of the disk. The temperature structure of the disk can thus be controlled by the X-ray field, photoionizing the gas, suppressing convection, and increasing the scale height of the disk [79]. Photoionization in the disk is balanced by radiative and dielectronic recombination [80], and possibly three-body recombination [81] and charge transfer recombination [82]. These recombination processes produce discrete line emission, which constitute spectral components distinct from the fluorescence component of the spectrum, potentially providing corollary information relating to the disk structure. A quantity that is commonly used to describe emission lines that are superimposed on a continuum is the equivalent width. Since we make several references to the equivalent width in later sections, we define it here for convenience. The experimentally measured line equivalent width is defined by

$$W_{\epsilon} = \int_0^{\infty} d\epsilon \frac{(F_{\epsilon})_{\text{line}}}{(F_{\epsilon})_{\text{cont}}}. \quad (10)$$

The equivalent width is usually quoted in units of eV or keV. Theoretical predictions of W_{ϵ} follow from calculations of accretion disk models, which can then be compared to observations. For example, early model calculations of the expected iron $K\alpha$ equivalent width, based on the response of an X-ray irradiated slab, showed that 90-150 eV was attainable [83].

The production of line emission, regardless of the formation mechanism, and the transfer of these lines through the overlying atmosphere requires, in principle, a detailed calculation of the opacity distribution along their lines of flight. The spatial distribution of the line emissivity, as well as a proper accounting of the probability of escape must, therefore, account for the vertical structure of the disk. This includes, in the limit that the vertical structure is in steady-state, the density, temperature, and charge state distribution. Thus each annulus of the disk can be thought of as a stellar atmosphere, where the equations of energy flow must be solved self-consistently with the ionization equations, possibly constrained by hydrostatic equilibrium. The explicit vertical structure of the disk, however, does not follow directly from the α -disk model. For example, the surface density – the line integral of the density in the vertical direction – appears as one of the variables in the disk equations. We return to the subject of the vertical structure of accretion disks as it bears on X-ray fluorescence in §7.

4. Astrophysical Black Holes

In this section, we present a brief survey of black holes from an astronomical point of view, touching on the gross characteristics of black holes in X-ray binaries and AGN.

4.1. Black Hole X-ray Binaries

Currently about 250 X-ray binaries are known in our galaxy [84] [85], possibly representing an underlying population of more than 1000 objects. X-ray binaries can be separated into two populations: the *low-mass X-ray binaries* (LMXBs), where “low-mass” refers to the companion star to the compact object, an older population, concentrated near the Galactic bulge; and the HMXBs (see §3.1), younger systems, concentrated in the spiral arms. Mass transfer from the companion to the compact object is found to typically differ for these two classes as well. In general, LMXBs transfer mass to their companions through Roche lobe overflow (Fig. 2). Mass transfer in HMXBs is generally mediated by stellar winds.

A subset of X-ray binaries, twenty or so, are identified as black holes paired with a star that serves as a mass donor for accretion [55] [86]. The most famous example of this class is Cygnus X-1, identified in 1972 as a black hole candidate [87]. A more common subclass of X-ray binaries are those for which the compact object is a neutron star, rather than a black hole. When the compact object in an X-ray binary system is shown to be more massive than about $3M_{\odot}$, the compact object is a good black hole candidate. For a small group of X-ray binaries, the mass measurement has been performed with high precision. This group of X-ray sources is usually referred to as *dynamically confirmed black holes*.⁵ A continually updated list of such objects can be found, thanks to J. Orosz⁶ (see [32] for a more detailed discussion). Among the dynamically confirmed black hole X-ray binaries, there are several recurrent X-ray novae, all of them LMXBs, and only three persistent sources – Cyg X-1, LMC X-1, and LMC X-3 – the latter of which are HMXBs. These special binaries span a large range in the parameter space of basic properties; for example, XTE J1118+480 has $P_{\text{orb}} = 0.17$ days and a binary separation of $\approx 2.8R_{\odot}$, whereas GRS 1915+105 has $P_{\text{orb}} = 33.5$ days and a binary separation $\approx 95R_{\odot}$.

Clearly, if a less strict standard of evidence is accepted, many more black hole candidates can be identified (see, e.g., [32] for a recent discussion). Still, given the small number of black hole candidates, it may be surprising that, from stellar evolutionary considerations, together with the incidence of the X-ray binaries that are believed to contain black holes, it is thought that the Milky Way Galaxy contains about ~ 300 million stellar-mass black holes [88] [89] [90] [91]. This number implies, assuming $\sim 10M_{\odot}$ per black hole [32], that about 4% of the total baryonic mass (i.e., stars plus gas) of the Galaxy is in the form of black holes.

The X-ray spectra of X-ray binaries are dominated by continuum radiation. The X-ray luminosities of persistent XRBs are intrinsically variable, and range anywhere from (typically) $L_x \sim 10^{36}$ erg s⁻¹ to as high as the Eddington luminosity of $\text{few} \times 10^{38}$ erg s⁻¹. In black hole X-ray novae, the range in X-ray luminosities is more dynamic, with quiescent luminosities as low as $L_x \sim 10^{30}$ erg s⁻¹ [92]. Based upon spectral observations in the soft X-ray band (say, 1–10 keV), two main categories of emission states have been distinguished, depending mostly on the slope of the power-law ($F_E \propto E^{-\alpha}$) describing the continuum emission of the system. Here, the differential photon count rate is given in units of photons cm⁻² s⁻¹ keV⁻¹. The so-called low state (relatively low photon count rate) features non-thermal X-ray flux, typically with slopes near 1.6 – 1.7. Because of the hardness (i.e.,

⁵ The relevant experimentally inferred quantity is the mass function, defined by $f(M) \equiv P_{\text{orb}} K_2^3 / 2\pi G = M_1 \sin^3 i / (1+q)^2$ where P_{orb} is the orbital period and K_2 is the semi-amplitude of the velocity curve of the secondary, M_1 is the black hole mass, i is the orbital inclination angle, and $q \equiv M_2/M_1$, where M_2 is the mass of the secondary, is the mass ratio. The equation for $f(M)$ implies that the value of the mass function is the absolute minimum mass of the compact primary. A secure value of $f(M)$ may be sufficient to show that the mass of the compact X-ray source is at least $3M_{\odot}$.

⁶ <http://mintaka.sdsu.edu/faculty/orosz/web/>

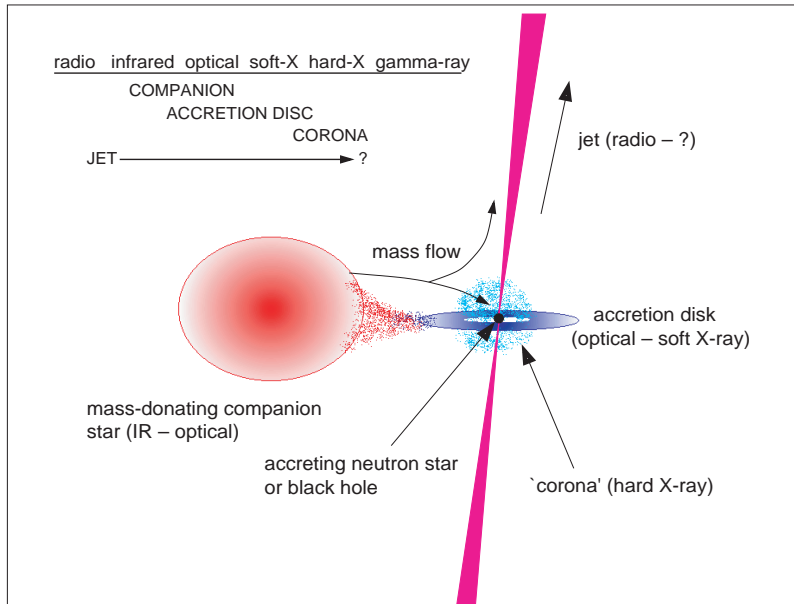


Fig. 2. Current basic understanding of the physical components and sites of emission in an X-ray binary system. In this example, the companion loses mass to the compact object through Roche lobe overflow. The accreting matter forms a disk, which can be thought of as a series of annular rings in quasi-Keplerian orbits, whose radii decrease under the action of stresses between neighboring annuli. Radiant energy is released, giving rise to X-ray emission at small radii. Hard X-ray emission impinges on the optically thick disk, which “reflects” a fraction of the incident flux, with spectral imprinting in the form of lines, absorption, and deformed continuum. A fraction of the accretion energy is redirected into kinetic energy, giving rise to the jets. A hot corona sandwiches the disk at small radii, which can affect the reflection spectrum through Compton scattering. From Fender and Maccarone [130].

relatively high ratio of hard X-ray flux to soft X-ray flux) of such indices, this state is also referred to as the low/hard state. The high state, by contrast, is characterized by intense quasi-thermal flux. In this state, most of the radiated energy is concentrated in a blackbody component, while the power-law contribution becomes softer, with power-law indices typically larger than 2. The usual interpretation is that the blackbody component originates in a cold, optically thick accretion disk, whereas the power-law component is produced in an optically thin hot corona by thermal Comptonization of disk photons [71] [98] [99] [100].

The first broad Fe $K\alpha$ line observed was reported in the spectrum of Cyg X-1, based upon *EXOSAT* data [23]. Recently, the *Chandra* X-ray observatory was used to observe Cyg X-1 with the High Energy Transmission Grating Spectrometer in an intermediate X-ray state [102]. A narrow Fe line was detected at $E = 6.415 \pm 0.007$ keV with an equivalent width (see Eq. 10) of $W_\epsilon = 16_{-2}^{+3}$ eV, along with a broad line at $E = 5.82 \pm 0.07$ keV with $W_\epsilon = 140_{-40}^{+70}$ eV. A smeared photoelectric edge was also detected at 7.3 ± 0.2 keV. These results are interpreted in terms of an accretion disk with irradiation of the inner disk producing the broad Fe $K\alpha$ emission line and edge, and irradiation of the outer disk producing the narrow line. The broad line is thought to be shaped by Doppler and gravitational effects and, to a lesser extent, by Compton reflection (see §7).

Early studies of relativistically smeared Fe $K\alpha$ lines from X-ray binaries relied on proportional

counter detectors with relatively poor spectral resolution (e.g., the *Ginga*'s LAC and the *RXTE*'s PCA, have an energy resolution of ≈ 1.2 keV at Fe $K\alpha$). The response matrices of the detectors are uncertain at the 1–2 % level, while the Fe line profile is typically only 1–5 % above the X-ray continuum [32]. Therefore, interpretations of results from these instruments must be approached with caution. *BeppoSAX*, with a resolution of ≈ 0.6 keV at 6.4 keV, has also been used to observe several black hole candidates. The observed iron emission generally appear to be rather symmetric, and may be more a product of Compton scattering than relativistic broadening. However, in the cases of GRS 1915+105 [103] and V4641 Sgr [104], the iron lines are skewed, possibly implying relativistic smearing. In addition, an observation using the *XMM* EPIC–MOS1 detector led to the report of a broad, skewed Fe $K\alpha$ emission in XTE J1650–500, perhaps suggesting the presence of a rapidly spinning black hole [105].

4.2. Active Galactic Nuclei

Approximately one in a hundred galaxies shows evidence for energy output that appears to be unrelated to normal stellar processes – rapid bulk motions, a bright, non-stellar radiation continuum, rapid aperiodic variability, and high-luminosity emission lines originating near the galactic nucleus. Members of this subset of galaxies are known as *active galaxies*, and the nuclei are referred to as AGN [106]. The classification scheme for active galaxies is somewhat daunting. We list here the various classes as they have been designated in the literature [107]: (1) radio galaxies; (2) radio quasars; (3) BL Lac objects; (4) optically violent variables; (5) radio quiet quasars; (6) Seyfert 1 galaxies; (7) Seyfert 2 galaxies; (8) low-ionization nuclear emission-line regions (LINERs); (9) nuclear H II regions; (10) starburst galaxies; and (11) strong IRAS galaxies. Not all among this group are active by virtue of black hole accretion. For example, starburst galaxies are sites of anomalously large star formation rates, probably the result of a gravitational encounter with another galaxy, leading to an enhanced IR luminosity. We do not delve here into the phenomenology that gives rise to this complex taxonomy. In what follows, we reserve the term AGN for active galaxies believed to harbor a supermassive black hole.

Within the unification scheme [108], the underlying model for all classes of AGN is intrinsically similar. At the very center of the galaxy sits a *supermassive black hole* ($\sim 10^6 - 10^{10} M_{\odot}$), which accretes galactic matter through an accretion disk. Broad emission lines are produced in clouds orbiting above the disc at high velocity (the Broad Line Region [109]), and this central region is surrounded by an extended, dusty, molecular torus. A hot electron corona sandwiches the inner regions of the disk, probably playing a dominant role in generating continuum X-ray emission. Two-sided jets of relativistic particles emanate perpendicular to the plane of the accretion disc, the generation of which is still not fully understood.

As pointed out in [110], X-ray surveys are an excellent means by which to locate AGN. Surveys using the *Chandra* and *XMM-Newton* observatories find a remarkable $\sim 10^3$ X-ray sources per square degree, the vast majority of which are undoubtedly AGN [111] [112]. To date, however, the most secure detections of supermassive black holes (accompanied by a “rule out” of alternative models, such as the existence of dense clusters of stars or exotic particles) come from stellar proper motion in the Galactic center and the H₂O megamaser of the nearby Seyfert 2 galaxy NGC 4258 [113] (see [114] and references therein for further discussion). Optical stellar and gas dynamical studies, generally using the Hubble Space Telescope, have revealed a large concentration of nuclear mass in several tens of candidates, believed to be black holes. It is true, however, that these methods currently lack sufficient angular resolution to probe the spacetime at distances on the scale of the black hole horizon (e.g., see [115]).

It is worth noting that nuclear activity is not a prerequisite for the presence of a black hole. In fact, most of the galaxies probed for supermassive black holes are not really active, but dormant quasars, relatively close to Earth, and for which the Keplerian signatures could be more easily discovered because of the higher spatial resolution [116]. The most famous example is provided by our own Galaxy

[117]. After charting the kinematics of stars swirling around the central regions of the Milky Way [118] [119] [120], it has been found that the total mass of the region enclosed within a radius of 2×10^{15} cm is approximately $3.7 \times 10^6 M_{\odot}$, far more compact than what is possible for a stable distribution of individual objects; total gravitational collapse is required, according to GR. Indeed, the only remaining alternative candidate, other than a black hole, to describe the behavior of the innermost stellar orbits in the center of the Milky Way Galaxy comes from particle physics, and is known as a boson star [121]. Mass estimates for central supermassive black holes in about twenty nearby galaxies are also available (see review in [122]). Therefore, if we assume that the Milky Way Galaxy is not unique in this respect, it is possible that a large fraction of galaxies, active or not, harbor supermassive black holes near their dynamical centers.

Currently, the Seyfert 1 galaxies MCG–6-30-15 [123] [124], Mrk 766 [125], and NGC 3516 [126] provide the most robust detections of the relativistically broadened iron $K\alpha$ line. In addition to the preceding papers, a concise set of case studies of these three objects is provided in [127].

4.3. Microquasars and Jets

Some X-ray binaries are sources of jets, high-velocity streams of oppositely directed particles originating near the compact object. These sources are called *microquasars* [128] [129], exploiting an analogy discussed in more detail below. Figure 2, from [130], is a sketch of an X-ray binary, presenting the major physical components and sites of emission in such systems. The basic underlying idea behind the analogy between quasars and microquasars is that the physics in all black hole systems is essentially governed by scaling laws, whose order parameter is the black hole mass. For instance, the scales of length and time of black hole related phenomena are proportional to the mass of the black hole. For a given critical accretion rate, the bolometric luminosity and length of relativistic jets are also proportional to the mass of the black hole. For a black hole of mass M the density and mean temperature in the accretion flow scale with M^{-1} and $M^{-1/4}$, respectively. The maximum magnetic field at a given radius in a radiation dominated accretion disk scales with $M^{-1/2}$, which implies that in the vicinity of stellar-mass black holes the magnetic fields may be 10^4 times stronger than that found near supermassive black holes [131].

One of the most impressive phenomena occurring in both quasars and microquasars is the ejection of blobs of plasma at apparently superluminal speed [132]. Very Long Baseline Interferometry at radio wavelengths allows position measurements down to milli-arcseconds, thereby permitting detections of small changes in position on the sky. The apparent velocity is obtained by multiplying the observed proper motion by the distance to the source. Such superluminal sources were discovered as radio-galaxies and quasars, where the central black hole is supposed to have millions of solar masses. It was found that this very same phenomenon could also occur in Galactic sources, after the report on GRS 1915+105 by Mirabel and Rodriguez [128].

4.4. Intermediate Mass Black Holes

Although consensus has not yet been reached, there are two types of data suggesting the existence of intermediate mass black holes, with masses between $\sim 20M_{\odot}$ and several thousand M_{\odot} [136]. First, there are numerous X-ray point sources, dubbed *ultraluminous X-ray sources*, that are not associated with AGN, and that have fluxes far beyond the Eddington limit of a stellar size black hole system. Second, several globular clusters show clear evidence for an excess of dark mass in their cores, which appears to be a single object. The number of such intermediate objects, as well as their actual existence, is yet under debate, and strongly depends on the mechanism that forms them. For both intermediate and supermassive black holes, the formation processes are not as well understood as they are for their stellar counterparts.

5. Black Hole Accretion in the Schwarzschild Metric

In this section we present in some detail a few of the results of general relativity that pertain to black hole accretion. As mentioned earlier, there are only three vacuum solutions for black holes. The simplest – the Schwarzschild metric – describes the geometry of spacetime outside the event horizon of a black hole with zero charge and angular momentum; mass alone describes the geometry. A clear and concise derivation of the Schwarzschild solution can be found in, for example, [137]. Before proceeding to the Schwarzschild solution, we introduce the unit conventions that have been adopted for dealing economically with calculations involving relativity.

5.1. Geometrized Units

In the domain of special relativity, space and time are linked by the invariant spacetime interval. By convention, we can rewrite the familiar expression for the proper time interval in flat spacetime $d\tau^2 = c^2 dt^2 - dx^2$ as $d\tau^2 = dt^2 - dx^2$ by expressing time in cm; 1 cm of time is, in conventional units, the time required for light to travel 1 cm, or $t_{\text{conv}} = t_{\text{cm}}/(3 \times 10^{10} \text{ cm s}^{-1})$.

In general relativity, the dimension of length is given to other quantities as well. For example, as mentioned in §1, the characteristic length scale in black hole physics is the gravitational radius⁷ $R_g = GM/c^2$. Thus one often encounters dimensionless terms of the form $r/(GM/c^2)$. In adopting geometrized units, we make the transformation

$$\frac{r}{GM/c^2} \rightarrow \frac{r}{M}, \quad (11)$$

where M carries the unit cm, so that r/M is dimensionless. Therefore, to convert mass expressed in cm to mass expressed in grams, use

$$M_{(\text{g})} = \frac{c^2}{G} M_{(\text{cm})} \quad \text{or} \quad M_{(\text{g})} = 1.347 \times 10^{28} M_{(\text{cm})}. \quad (12)$$

For example, the mass of the black hole near the center of the Milky Way Galaxy ($M \approx 3.7 \times 10^6 M_\odot$ or 7.4×10^{39} g in conventional units) is 5.5×10^{11} cm.

Angular momentum, symbolized here as J or L , has dimensions of length squared in geometrized units. The conversion is

$$\frac{c^3}{G} J_{(\text{cm}^2)} = J_{(\text{g cm}^2 \text{ s}^{-1})}. \quad (13)$$

For convenience with mathematical manipulations, the spin of a black hole is characterized by the quantity $a = J/M$, where J is the angular momentum of the hole. The conversion between geometric units and c.g.s. units is

$$a = \frac{J_{(\text{cm}^2)}}{M_{(\text{cm})}} = \frac{J_{(\text{g cm}^2 \text{ s}^{-1})}}{M_{(\text{g})}c}, \quad (14)$$

so that spin has dimensions of length. Since mass also has dimensions of length, it is often useful to define a dimensionless *spin parameter*, $a_* = a/M$. If the mass and angular momentum of a spinning object are known in conventional units, a dimensionless a/M follows from

$$a_* = \frac{a}{M} = \frac{c}{G} \frac{J}{M^2} \Big|_{\text{c.g.s.}} \quad (15)$$

⁷ As an easy-to-remember conversion, the gravitational radius of an object is 1.477 km per solar mass.

5.2. The Schwarzschild Metric

A spacetime *metric* provides a “rule” by which to relate measurements of events in different frames. The *Minkowski metric*,

$$d\tau^2 = dt^2 - (dx^1)^2 - (dx^2)^2 - (dx^3)^2, \quad (16)$$

can be expressed in a more concise form if we define a set of metric coefficients $\eta_{\alpha\beta}$. Thus one can write $d\tau^2 = -\eta_{\alpha\beta} dx^\alpha dx^\beta$, where $dx^0 = dt$, $\eta_{00} = -1$, $\eta_{jj} = 1$ for $j = 1, 2, 3$, and where summation is performed over all repeated indices.

More generally, a spacetime metric has the form

$$d\tau^2 = -g_{\mu\nu} dx^\mu dx^\nu, \quad (17)$$

where the metric coefficients can be functions of the spacetime coordinates. The Schwarzschild solution to the Einstein field equations yields the metric

$$d\tau^2 = \left(1 - \frac{2M}{r}\right) dt^2 - \left(1 - \frac{2M}{r}\right)^{-1} dr^2 - r^2 (d\theta^2 + \sin^2 \theta d\phi^2), \quad (18)$$

which is the vacuum solution to the spacetime outside of a spherical mass M (for a derivation, see, e.g., [137] [138]). The metric coefficients $g_{\mu\nu}$ can be read off directly. The t -coordinate is the time as measured by a distant observer. The r -coordinate, called the *reduced circumference*, is defined such that the circumference of a circle centered on the gravitating mass is precisely $2\pi r$. The θ - and ϕ -coordinates are defined such that $r d\theta$ and $r d\phi$, respectively, measure differential distances along tangents to a circle at r , again, centered on the gravitating mass. For $r \gg 2M$, the Schwarzschild metric reduces to the Minkowski metric (Eq. 16), after a transformation between spherical polar coordinates and Cartesian coordinates. There is, however, no transformation of coordinates that can globally reduce the Schwarzschild metric to the Minkowski metric. Thus the spacetime described by the former is said to be curved, whereas the Minkowski spacetime is said to be flat — “flat” in the sense that it is quasi-Euclidean.

Since the metric is spherically symmetric, the motion of test particles and photons is restricted to a plane. This plane, with no loss of generality, can be chosen to be the equatorial plane ($\theta = \pi/2$). For events occurring within the equatorial plane, we can also set $d\theta = 0$ in Eq. (18), which gives the simplified proper time interval,

$$d\tau^2 = \left(1 - \frac{2M}{r}\right) dt^2 - \left(1 - \frac{2M}{r}\right)^{-1} dr^2 - r^2 d\phi^2. \quad (19)$$

The proper length interval ds ($ds^2 = -d\tau^2$) is given by

$$ds = \left(1 - \frac{2M}{r}\right)^{-1/2} dr. \quad (20)$$

5.3. Gravitational Time Dilation and Gravitational Red Shift

Even before Einstein arrived at his final formulation of the field equations, he argued the case for gravitational time dilation. The standard version of his derivation appeared in 1911, although he was aware of the effect as early as 1907 [1]. We provide here a derivation that follows the one presented in [137], except that we will take advantage of the explicit form of the Schwarzschild solution, thereby deriving a result that will be useful later.

Imagine that two identical clocks are manufactured in a region of flat spacetime and calibrated so that every hour the clocks chime together, each clock thus marking proper time intervals $\Delta\tau$

corresponding to one hour. Two experimenters, A and B , are enlisted. A moves one clock to a position at distance r_A from a gravitating object. B moves the other clock to a position at distance $r_B > r_A$ from the mass (Fig. 3). At each chiming, A records the time, and will maintain that the passage of time from chime to chime Δt_A is precisely one hour. According to Eq. (19), A measures $\Delta t_A = \Delta\tau/\sqrt{1-2M/r_A}$. Light pulses are sent from r_A to r_B at each chiming of A 's clock, and B records the arrival times. Light pulses require time – according to observers in *any* frame – to travel from A to B . Nevertheless, B records a pulse-to-pulse time separation of precisely Δt_A , provided that the light paths are identical for each pulse. When he compares the chime-to-chime record of his own clock, however, he finds that $\Delta t_B < \Delta t_A$, where B will insist that Δt_B is one hour. B measures $\Delta t_B = \Delta\tau/\sqrt{1-2M/r_B}$. B is forced to conclude that time runs slower at r_A than at r_B . If the experiment were altered such that B sent pulses to A , then A would be forced to conclude that time runs faster at r_B than at r_A . This effect is known as gravitational time dilation.

For our purposes, it is more appropriate to express time dilation in terms of light frequencies. Referring to the experiment above, and replacing the clocks by radiating atoms, label by ν_{obs} the frequency of light originating at A as observed at B , and label by ν_{em} the frequency of an identical source at B as observed by B . The ratio of the frequencies is, therefore,

$$\frac{\nu_{\text{rec}}}{\nu_{\text{em}}} = \frac{\Delta t_B}{\Delta t_A} = \left(\frac{1-2M/r_A}{1-2M/r_B} \right)^{1/2}. \quad (21)$$

The case of primary interest – observing radiation from a distant source – corresponds to $r_B \rightarrow \infty$. This gives us the expression for the *gravitational redshift* for a Schwarzschild black hole, according to the observer at infinity,

$$\nu_{\infty} = \nu_{\text{em}} \left(1 - \frac{2M}{r} \right)^{1/2}. \quad (22)$$

As $r \rightarrow 2M$, the observer at infinity finds that $\nu_{\text{obs}} \rightarrow 0$. For this reason, the radius $r = 2M$ is sometimes referred to as the *surface of infinite redshift*. It is important to remember that this expression is valid only for the case of a stationary source and a stationary receiver. Below, we will accommodate the case of a source in orbit around a black hole.

5.4. Conserved Quantities

Before discussing the motion of particles and photons in the Schwarzschild metric, we will need two conservation laws, which follow from the equations of motion. The equations of motion of free particles in curved spacetime can be derived from the Euler-Lagrange equations, for an appropriate Lagrangian Λ , according to

$$\frac{d}{dp} \frac{\partial \Lambda}{\partial \dot{x}^\alpha} - \frac{\partial \Lambda}{\partial x^\alpha} = 0 \quad (23)$$

where the dot denotes differentiation with respect to a timelike parameter p . A useful form for the Lagrangian is

$$\Lambda = \frac{1}{2} g_{\alpha\beta} \frac{dx^\alpha}{dp} \frac{dx^\beta}{dp}. \quad (24)$$

with $p = \tau/m$, as shown in [10]. For the Schwarzschild metric, again reducing the problem to motion in the $\theta = \pi/2$ plane, this is

$$2\Lambda = - \left(1 - \frac{2M}{r} \right) \left(\frac{dt}{dp} \right)^2 + \left(1 - \frac{2M}{r} \right)^{-1} \left(\frac{dr}{dp} \right)^2 + r^2 \left(\frac{d\phi}{dp} \right)^2 \quad (25)$$

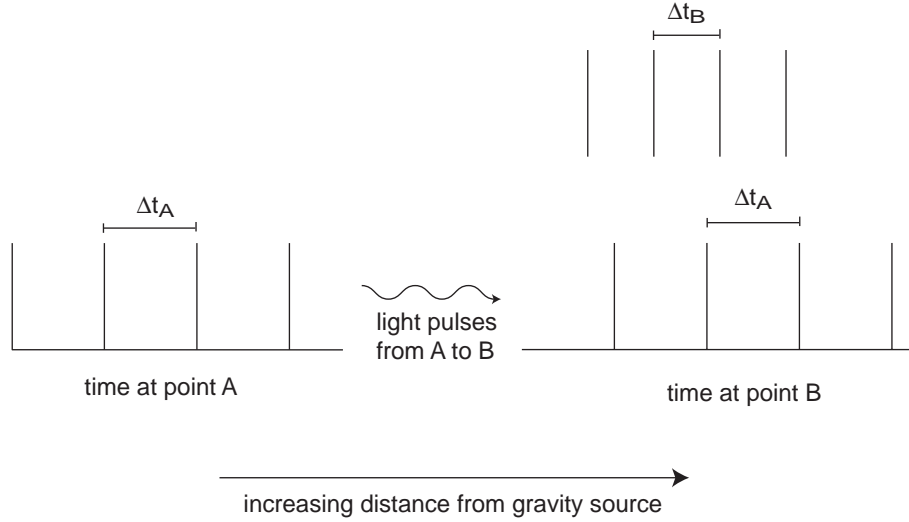


Fig. 3. Gravitational time dilation. Two identically manufactured clocks are positioned at points A and B , with $r_B > r_A$ with respect to a gravitating mass. An observer at A sends pulses to observer at B at each chiming of the clock at A . Observer at B notes that chime frequency is higher at B than at A and concludes that time runs slow at A . See text for further discussion.

Evaluating Eq. (23) for the t -coordinate, we find

$$\frac{E}{m} = \left(1 - \frac{2M}{r}\right) \frac{dt}{d\tau} \quad (26)$$

where the constant of the motion, labeled E/m , is identified with the energy per unit mass of the particle, since Eq. (26) reduces to the special relativistic expression $E = m dt/d\tau$ for large r , i.e., the time-component of the momentum four-vector. Similarly, evaluating Eq. (23) for the ϕ -coordinate, we find a second constant of the motion

$$\frac{L}{m} = r^2 \frac{d\phi}{d\tau}. \quad (27)$$

where L/m can be identified as the angular momentum per unit mass.

5.5. The Effective Potential

The usual Newtonian approach to the problem of calculating the orbit of a test particle under the influence of a spherically symmetric gravitational field involves finding two constants of the motion – energy and angular momentum – and recasting the radial equation in terms of an effective potential. The effective potential is the sum of the gravitational potential and a centrifugal term. From an analysis of the radial excursions in this effective potential, one finds the two basic orbit classes – elliptical and hyperbolic – corresponding to bound and unbound motion, respectively, with circular orbits corresponding to a special case of elliptical orbits. A similar, and quite fruitful, approach is adopted to analyze the orbit classes for motion in the Schwarzschild metric.

To derive the effective potential for the Schwarzschild metric, notice that Equations (19), (26), and (27) can be treated as a set of three equations in the four unknowns $d\tau$, dt , dr , and $d\phi$. Therefore, we can eliminate dt and $d\phi$ in Eq. (19) to obtain

$$\left(\frac{dr}{d\tau}\right)^2 = \left(\frac{E}{m}\right)^2 - \left(1 - \frac{2M}{r}\right) \left[1 + \frac{(L/m)^2}{r^2}\right], \quad (28)$$

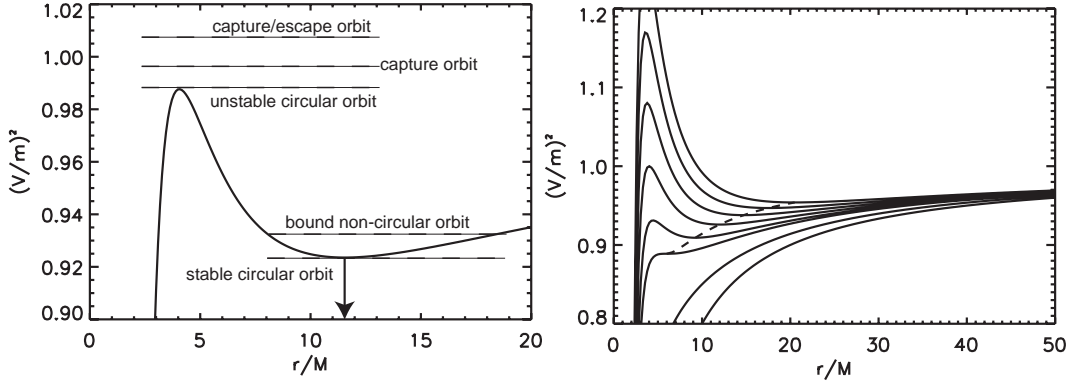


Fig. 4. (Left panel) Effective potential for a test particle trajectory in the Schwarzschild metric (Eq. 29) with $L/mM = 3.95$. Dashed lines correspond to five different energies, increasing from bottom to top. See text for a discussion. (Right panel) Effective potential for various values of the angular momentum: from bottom to top, $L/mM = [0., 2.5, 2\sqrt{3}, 3.7, 4.0, 4.3, 4.6, 4.9]$. Intersections of the dashed line with potential curves marks positions of stable circular orbits. The innermost stable circular orbit occurs at $r/M = 6$, corresponding to $L/mM = 2\sqrt{3}$.

and one defines the effective potential according to

$$\left(\frac{V}{m}\right)^2 = \left(1 - \frac{2M}{r}\right) \left[1 + \frac{(L/m)^2}{r^2}\right] \quad (29)$$

Note that the effective potential cannot be associated with an actual potential energy, as in Newtonian mechanics; in general relativity, it is impossible to separate energy into a kinetic term and a potential term. Rather, the effective potential merely allows us to characterize certain aspects of particle trajectories without integrating the equations of motion.

One example of the effective potential is plotted in the left panel of Fig. 4; as $r \rightarrow \infty$, $V(r) \rightarrow 1$ as can be seen from Eq. (29). The curve is, in fact, qualitatively similar to analogous curves derived from the Newtonian prescription, except for small radii, where the two differ dramatically, i.e., the repulsive centrifugal barrier that extends to arbitrarily small radii in the Newtonian potential is absent at small radii in the Schwarzschild effective potential. Any inward bound particle that finds itself within the region of this downturn of V , which has been referred to as “the pit in the potential” [170], is destined to fall through the event horizon. Energies corresponding to such capture orbits are indicated by the top two dashed lines in Fig. 4. The top line, with $E/m > 1$, is labeled “capture/escape orbit” because inward bound particles are captured, whereas outward bound particles can escape to infinity. The energy level labeled “capture orbit” corresponds to a particle that, if inward bound, passes through the event horizon, and, if outward bound, arrives at apastron, returns, since $E/m < 1$, then passes through the event horizon. Below that is the level for a particle with energy corresponding to an unstable circular orbit at $r = r_{\text{us}}$. Test particles with this energy, whether directed inward from $r > r_{\text{us}}$ or directed outward from $r < r_{\text{us}}$, will end up on this orbit, and remain there until perturbed. The next orbit is bound, since particles with this energy transit between two turning points. The Newtonian analogy for this orbit is an ellipse. In the Schwarzschild metric, the azimuthal oscillation frequency exceeds the radial oscillation frequency, leading to an orbit with a precessing apastron, with prograde precession. The final trajectory class, corresponding to the local minimum of V , is a stable circular orbit, discussed in the next section.

5.6. Circular Orbits in the Schwarzschild Metric

The most important general relativistic effect for X-ray line shapes is the gravitational redshift. The redshift formula is given in Eq. (22), and we intend to use that in our discussions of line profiles. However, as remarked there, the formula is valid only in the case of stationary emitter and receiver, and the emitters in an accretion disk are not stationary. In fact, we expect relativistic velocities. In order to preserve the use of the simple equation for the redshift, we need first to know the photon energies as they would be measured by *local stationary observers* ($dr/d\tau=d\phi/d\tau=d\theta/d\tau=0$), distributed in radius. We denote with the subscript *lso* measurements made by such observers. Once we know the local photon energy distribution, it is then a simple matter to calculate the distribution at infinity by application of Eq. (22). Since disk material is, in the approximation that disk annuli describe circular orbits, passing the stationary observer with azimuthal velocity $r d\phi/dt_{lso}$, we can simply apply a Lorentz transformation that relates the spectrum in the disk frame to the spectrum measured by the stationary observer. The effective potential dictates a relationship between the angular momentum and the radius of circular orbits. Once we find this relationship, we proceed to the radial dependence of the velocity of circular orbits.

5.6.1. Angular Momentum/Radius Relationship for Circular Orbits

The condition for a circular orbit, $\partial V/\partial r = 0$, yields a relationship between r and L . Using Eq. (29), this is

$$r^2 - \left(\frac{L}{m}\right)^2 \frac{r}{M} + 3\left(\frac{L}{m}\right)^2 = 0, \quad (30)$$

which has the two solutions

$$r_{\pm} = \frac{(L/m)^2}{2M} \left[1 \pm \left(1 - \frac{12M^2}{(L/m)^2} \right)^{1/2} \right]. \quad (31)$$

The stability condition $\partial^2 V/\partial r^2 > 0$ shows that a circular orbit at r_+ is stable, while the one at r_- is unstable. Equation (31) thus provides the radii of both the unstable circular orbit and the stable circular orbit for a given value of L/m . We further see, that, owing to presence of the square root, the domain of allowed L/m yielding a circular orbit is restricted to $L/m > 2\sqrt{3}M$. Setting L/m to this minimum value in Eq. (31), we find that the radius of the *innermost stable circular orbit* r_{isco} is equal to $6M$.

The existence of the innermost stable circular orbit, a uniquely general relativistic feature, can be appreciated by inspection of the right panel of Fig. 4, which shows the effective potential for several values of the angular momentum. The intersection of the dashed line with each effective potential curve marks the radial position of each stable circular orbit. The trend in the behavior of V with L/m is clear: as L/m decreases, the extent of the potential barrier decreases, as well. As $L/m \rightarrow 2\sqrt{3}M$, the barrier flattens, and disappears for $L/m < 2\sqrt{3}M$, thereby eliminating the local minimum. All inward bound trajectories with $L/m < 2\sqrt{3}M$ cross the event horizon.

5.6.2. Energies of Circular Orbits

From Eq. (28), setting $dr/d\tau = 0$ for a circular orbit,

$$\left(\frac{E}{m}\right)^2 = \left(1 - \frac{2M}{r}\right) \left[1 + \frac{(L/m)^2}{r^2}\right]. \quad (32)$$

From Eq. 30, we have

$$\left(\frac{L}{m}\right)^2 = \frac{r^2}{r/M - 3}, \quad (33)$$

which, when substituted into Eq. (32), gives

$$\frac{E}{m} = \frac{1 - 2M/r}{(1 - 3M/r)^{1/2}} \quad (34)$$

This expression for energy is valid only for $r \geq 6M$ because of the stability restriction.

At the ISCO, where $r/M = 6$, we have $(E/m)_{\text{isco}} = (8/9)^{1/2}$. Therefore, the energy change per unit mass of a test particle as its circular orbit degrades from a large distance to the ISCO is

$$\Delta\left(\frac{E}{m}\right) = 1 - \left(\frac{8}{9}\right)^{1/2} \approx 0.057 \quad (35)$$

i.e., the test particle loses an energy equivalent to about 6% of its rest mass energy as it works its way down to the ISCO in a succession of circular orbits. This is often taken as the maximum accretion efficiency η of a Schwarzschild black hole, in the sense that $L_{\text{acc}} = \eta \dot{M}_{\text{acc}} c^2$.

5.6.3. Velocities of Circular Orbits

We need to find the radial dependence of the velocities of circular orbits $v_\phi = r d\phi/dt_{\text{iso}}$ as they would be measured by locally stationary observers distributed in r . Proper time is measured in the disk frame, so that we can write

$$v_\phi = r \frac{d\phi}{d\tau} \frac{d\tau}{dt_{\text{iso}}}, \quad (36)$$

and then relate dt_{iso} and $d\tau$ by a Lorentz transformation:

$$dt_{\text{iso}} = (1 - v_\phi^2)^{-1/2} d\tau. \quad (37)$$

Using angular momentum conservation (Eq. 27), Eq. (36) becomes

$$v_\phi^2 = \frac{1}{r^2} (L/m)^2 (1 - v_\phi^2). \quad (38)$$

Substituting for L/m from Eq. (30), and recalling that that equation is valid only for stable circular orbits, some rearrangement gives

$$v_\phi^2 = \frac{M/r}{1 - 2M/r}, \quad (39)$$

which decreases monotonically with radius. The domain of validity is the same as the domain for which stable circular orbits can exist, i.e., $r \geq 6M$. The velocity of a particle in a circular orbit at the ISCO can be found from Eq. (39) by substituting $r = 6M$, from which we find that $v_{\text{isco}} = 1/2$.

For the sake of interest, let us find the linear velocity v_∞ and angular velocity Ω_∞ of matter in a circular orbit as observed at infinity. To find the angular velocity, we start with the angular momentum conservation law (Eq. 27) and write

$$\Omega_\infty = \frac{L/m}{r^2} \frac{d\tau}{dt}, \quad (40)$$

so that we need to relate dt and $d\tau$ for a circular orbit. This is accomplished by manipulating a simplified form of the metric (Eq. 19), setting $dr = 0$,

$$d\tau^2 = \left(1 - \frac{2M}{r}\right) dt^2 - r^2 d\phi^2, \quad (41)$$

which, after eliminating $d\phi/d\tau$, again using Eq. (27), becomes

$$\left(1 - \frac{2M}{r}\right) \left(\frac{dt}{d\tau}\right)^2 = 1 + \frac{(L/m)^2}{r^2}. \quad (42)$$

Substituting for L/m from Eq. (33) and simplifying gives

$$\frac{d\tau}{dt} = \left(1 - \frac{3M}{r}\right)^{1/2} \quad (r \geq 6M). \quad (43)$$

Substituting this back into Eq. (40), again using Eq. (27) gives

$$\Omega_\infty = \left(\frac{M}{r^3}\right)^{1/2} \quad (r \geq 6M), \quad (44)$$

which is identical to the Newtonian result. The linear velocity is simply $r\Omega_\infty$, i.e.,

$$v_\infty = \left(\frac{M}{r}\right)^{1/2} \quad (r \geq 6M), \quad (45)$$

which is also identical to the Newtonian result.

5.7. The Motion of Light in the Schwarzschild Metric

For light motion (technically, for the motion of massless particles), we derive the governing equations by starting with the equations of motion for massive particles, then take the limit $m \rightarrow 0$. Starting with Eq. (28), we have

$$\left(\frac{dr}{dt}\right)^2 \left(\frac{dt}{d\tau}\right)^2 = \left(\frac{E}{m}\right)^2 - \left(1 - \frac{2M}{r}\right) \left[1 + \frac{(L/m)^2}{r^2}\right]. \quad (46)$$

Using the equation for the conserved energy (Eq. 26), the previous expression gives

$$\left(\frac{dr}{dt}\right)^2 = \left(1 - \frac{2M}{r}\right)^2 - \left(1 - \frac{2M}{r}\right)^3 \left[\frac{m^2}{E^2} + \frac{L^2}{r^2 E^2}\right]. \quad (47)$$

Taking the limit $m \rightarrow 0$, and defining the *impact parameter* $b = L/E$, we find

$$\left(\frac{dr}{dt}\right)^2 = \left(1 - \frac{2M}{r}\right)^2 \left[1 - \frac{b^2}{r^2} \left(1 - \frac{2M}{r}\right)\right]. \quad (48)$$

For the azimuthal motion, we combine Eqs. (26) and (27) to give

$$\frac{d\phi}{dt} \frac{E}{m} \left(1 - \frac{2M}{r}\right)^{-1} = \frac{L/m}{r^2}, \quad (49)$$

which becomes

$$\frac{d\phi}{dt} = \frac{b}{r^2} \left(1 - \frac{2M}{r}\right). \quad (50)$$

Therefore, once we know the impact parameter (see below), the light path can be calculated as parameterized by our measure of time t . By eliminating dt between Eqs. (48) and (50), we can plot the trajectory $r(\phi)$ according to

$$\frac{dr}{d\phi} = \frac{r^2}{b} \left[1 - \frac{b^2}{r^2} \left(1 - \frac{2M}{r}\right)\right]^{1/2}. \quad (51)$$

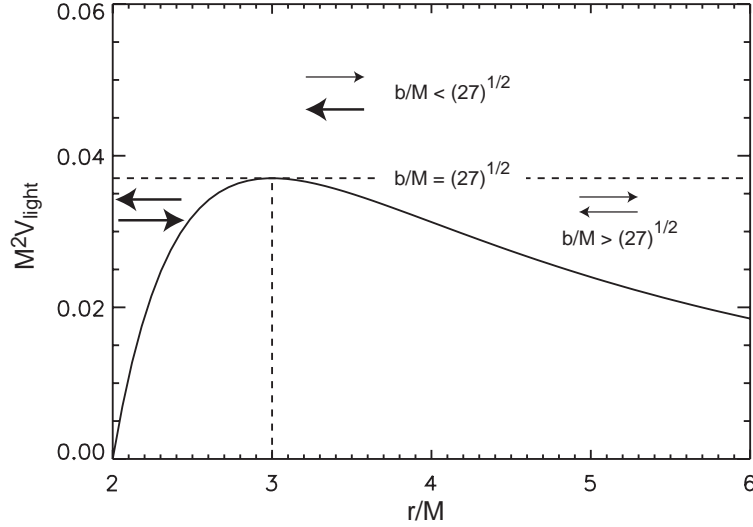


Fig. 5. Effective potential for light motion near a Schwarzschild black hole (see Eq. 54). Three sets of (r, b) constitute the range of possibilities for light motion in the Schwarzschild potential, where b is the impact parameter. Light arrows indicate escape orbits, heavy arrows are capture orbits. The vertical dashed line shows the position of the unstable circular orbit.

5.7.1. Effective Potential for Light Motion

We wish to obtain an effective potential for light, analogous to that found for particle motion, in order to gain a quick qualitative understanding of light motion, without having to perform numerical integrations of the equations of motion. Following [152], we need the relations between time and radial displacements as measured by a local stationary observer and those measured by a distant observer, which results in

$$\frac{dr_{\text{iso}}}{dt_{\text{iso}}} = (1 - 2M/r)^{-1} \frac{dr}{dt}. \quad (52)$$

Then, Eq. (48) can be written

$$\frac{1}{b^2} \left(\frac{dr_{\text{iso}}}{dt_{\text{iso}}} \right)^2 = \frac{1}{b^2} - \frac{1}{r^2} \left(1 - \frac{2M}{r} \right), \quad (53)$$

and we identify as the effective potential for light

$$V(r) = \frac{1}{r^2} \left(1 - \frac{2M}{r} \right). \quad (54)$$

Note the simplicity of the description of light trajectories compared to particle trajectories, where, in the latter case, the geodesics depend both on energy and angular momentum.

The effective potential for light is plotted in Fig. 5. The peak of V occurs at $r = 3M$, for which $V_{\text{peak}} = 1/27M^2$. For the critical impact parameter, $b_{\text{crit}} = 3\sqrt{3}M$, $dr_{\text{iso}}/dt_{\text{iso}} = 0$ at $r = 3M$. This is the only radius for which a massless particle can move on a circular orbit. However, the orbit is clearly unstable; any perturbation to the orbit will lead to either to capture or escape.

For the purposes of determining the range of impact parameters that lead to capture by the black hole, the presence of the potential peak at $r = 3M$ and the critical impact parameter divides space into two. First, consider light rays emanating from radii $r_o > 3M$. From Fig. (5), we see that all outward

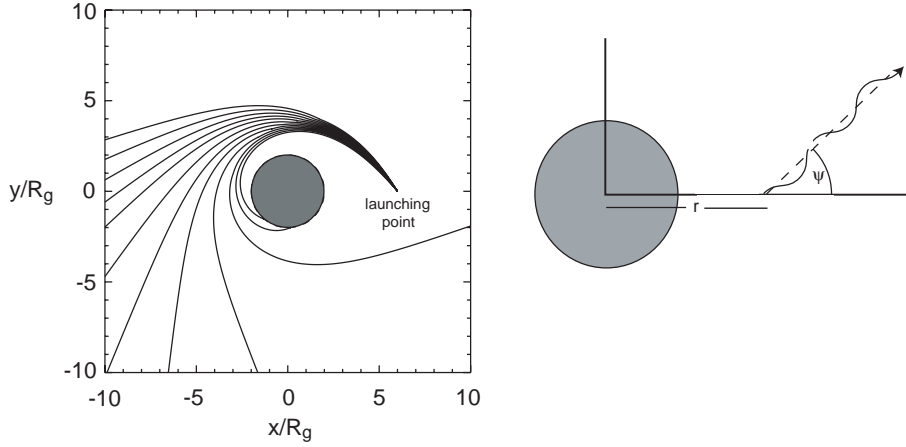


Fig. 6. (Left panel) Light trajectories in the Schwarzschild metric (see Eq. 51) for point of origin $r = 6M$ for twelve impact parameters confined to the range $5.0M$ – $5.9M$. (Right panel) The angle ψ between a light ray and a radius vector, as measured by a local stationary observer, used to define the impact parameter (see Eq. 56).

directed photons escape to infinity. For inward directed rays, those for which $b < 3\sqrt{3}M$ are captured. For photons originating inside $r = 3M$, all inward directed photons are captured. Outward directed photons are captured if $b > 3\sqrt{3}M$, and escape otherwise.

Using the effective potential, we can calculate the fraction of photons that will be captured by the black hole if emitted isotropically by a stationary source at r . First, we need to know how to calculate b for various cases of interest. Suppose photons are being launched at various angles from a point r near the black hole. We can find b by referring to the azimuthal equation of motion. From Eq. (50), reckoning time according to a local stationary observer, we have

$$r \frac{d\phi}{dt_{\text{ISO}}} = v_{\phi} = \frac{b}{r} \left(1 - \frac{2M}{r}\right)^{1/2} \quad (55)$$

Using the coordinate system illustrated in the right panel of Fig. (6), this becomes

$$b = r \left(1 - \frac{2M}{r}\right)^{-1/2} \sin \psi_{\text{ISO}} \quad (56)$$

As an aside, a distinction needs to be made between angles measured by a locally stationary observer and those calculated by a distant observer. The relation between ψ_{ISO} and the same angle according to a distant observer ψ_{∞} can be found as follows. Let the radial displacement measured by the LSO be denoted by ds . Then

$$\tan \psi_{\infty} = \frac{r d\phi}{dr} = \frac{r d\phi}{ds} \frac{ds}{dr} = \left(1 - \frac{2M}{r}\right)^{-1/2} \tan \psi_{\text{ISO}}, \quad (57)$$

where we have used Eq. (20) to relate ds and dr .

Now, for $r > 3M$, we already know that all outward directed photons escape. Inward directed photons are captured if $\sin \psi_{\text{ISO}} < 3\sqrt{3}(M/r)\sqrt{1 - 2M/r}$. This results in

$$f_{\text{capt}} = \frac{1}{2} \left[1 - \sqrt{1 - 27 \left(\frac{M}{r}\right)^2 \left(1 - \frac{2M}{r}\right)} \right] \quad (r \geq 3M). \quad (58)$$

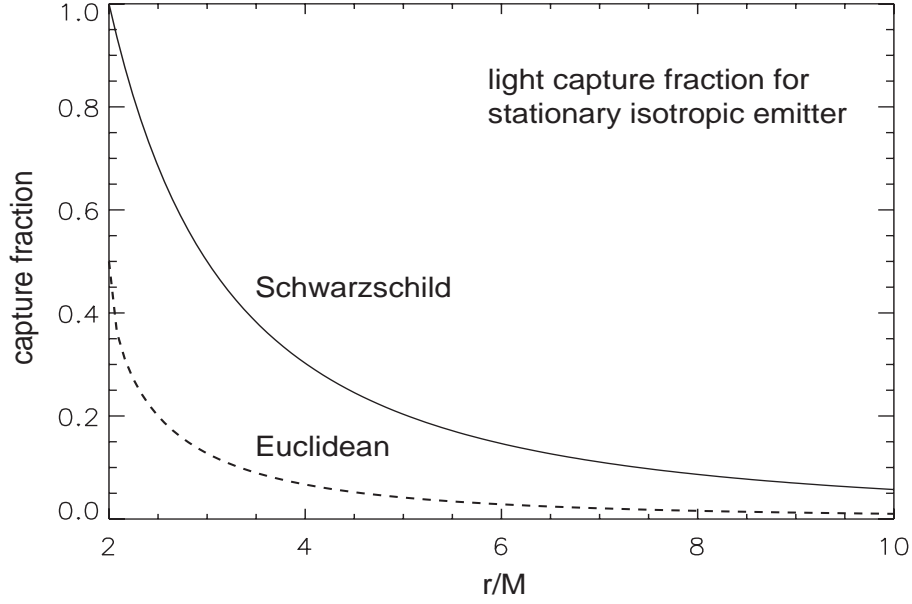


Fig. 7. Capture fraction for stationary isotropic photon emitters plotted against radius for the Schwarzschild metric and for Euclidean space. In the latter case, the capture fraction is simply the fractional solid angle subtended at r by a sphere of radius $2M$. For the Schwarzschild case, light bending is included.

For $r < 3M$, we already know that inward directed photons are captured. Outward directed photons are captured if $\sin \psi > 3\sqrt{3}(M/r)\sqrt{1 - 2M/r}$, which results in

$$f_{\text{capt}} = \frac{1}{2} \left[1 + \sqrt{1 - 27 \left(\frac{M}{r} \right)^2 \left(1 - \frac{2M}{r} \right)} \right] \quad (r \leq 3M). \quad (59)$$

The capture fraction is $1/2$ for $r = 3M$, and approaches unity as $r \rightarrow 2M$. A plot of f_{capt} vs. r is plotted in Fig. (7). Calculating the captured fraction for material moving in a disk must also account for relativistic beaming. In other words, a moving isotropic photon source will, to varying degrees, appear anisotropic to the stationary observer, with its emission concentrated into the direction of motion.

5.7.2. The Speed of Light

One of the more peculiar aspects of light propagation near a black hole is that those performing calculations in flat spacetime must account for the apparent reduction of the speed of light. According to a distant observer, the speed of light for pure radial motion, from Eq. (48), with $b = 0$, is

$$\frac{dr}{dt} = \pm \left(1 - \frac{2M}{r} \right), \quad (60)$$

which approaches unity for large r , and approaches zero as $r \rightarrow 2M$. For example, according to an observer at r , the time Δt for a light pulse to propagate radially from a position $r_o < r$ to r is

$$\frac{\Delta t}{M} = \frac{r - r_o}{M} + 2 \ln \frac{r/2M - 1}{r_o/2M - 1}, \quad (61)$$

which shows the effect of the reduced speed of light (2nd term) compared to the Euclidean value (1st term). Here we are measuring time in multiples of M . The conversion between seconds and centimeters is $\Delta t_{(s)} = (GM/c^3)\Delta t_{(cm)}$.

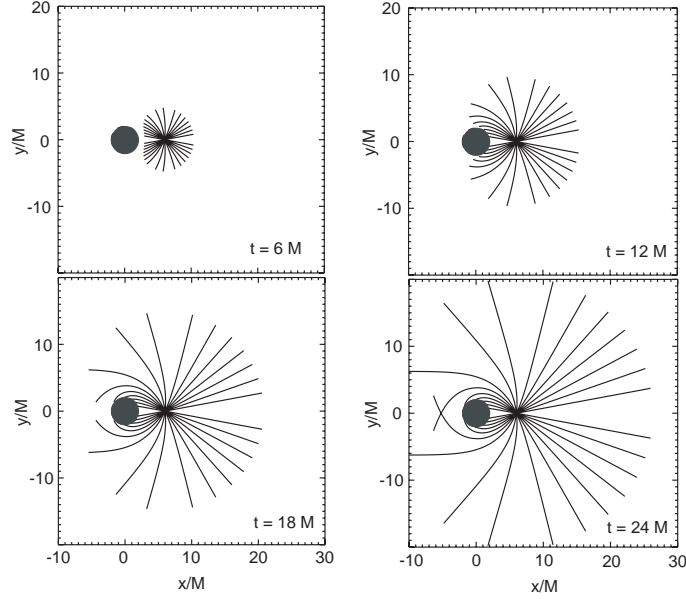


Fig. 8. Time dependence of an initially radial planar light pulse near a Schwarzschild black hole. Time intervals are measured from initiation of pulse at $t = 0$. Deviation from perfectly circular wave fronts illustrates the combined effect of a variable speed of light and light bending, as calculated by a distant observer. Plots based on integrations of Eq. 51.

The apparent speed of light for pure azimuthal motion is, from Eq. (50),

$$r \frac{d\phi}{dt} = \pm \frac{b}{r} \left(1 - \frac{2M}{r}\right) = \pm \left(1 - \frac{2M}{r}\right)^{1/2}, \quad (62)$$

where we have substituted for b from Eq. (56). Note that this is not the same as the speed of light for pure radial motion (Eq. 60).

Combining Eqs. (60) and (62), we can evaluate the speed of light for arbitrary trajectories according to a distant observer

$$c_\infty = \left[\left(\frac{dr}{dt}\right)^2 + \left(r \frac{d\phi}{dt}\right)^2 \right]^{1/2} = \left(1 - \frac{2M}{r}\right) \left(1 + \frac{2b^2 M}{r^3}\right)^{1/2} \quad (63)$$

While this apparent non-constancy of the speed of light might seem somewhat disorienting, it is important to realize that we do not actually *measure* this speed. Measurements must be made locally. We can calculate what a locally stationary observer will measure by transforming Eqs. (60) and (62) to the frame of such an observer.

$$\frac{dr_{\text{iso}}}{dt_{\text{iso}}} = \left(1 - \frac{2M}{r}\right)^{-1} \frac{dr}{dt} = \left[1 - \frac{b^2}{r^2} \left(1 - \frac{2M}{r}\right)\right]^{1/2} \quad (64)$$

$$r \frac{d\phi}{dt_{\text{iso}}} = \left(1 - \frac{2M}{r}\right)^{-1/2} r \frac{d\phi}{dt} = \frac{b}{r} \left(1 - \frac{2M}{r}\right)^{1/2} \quad (65)$$

These two equations give

$$c_{\text{iso}} = \left[\left(\frac{dr_{\text{iso}}}{dt_{\text{iso}}}\right)^2 + \left(r \frac{d\phi}{dt_{\text{iso}}}\right)^2 \right]^{1/2} = 1. \quad (66)$$

Therefore, locally stationary observers always measure $c = 1$. We, as distant observers, must contend with the fact that light appears to propagate at varying speeds, its speed depending on both the radial coordinate and the impact parameter.

An example that illustrates the effect of a variable speed of light is shown in Fig. (8). A planar radial burst of light is emitted from $r = 6M$ near a Schwarzschild black hole. Shown in the figure are the trajectories of a set of rays with a distribution of impact parameters, the endpoint of each trajectory indicating the progression of the leading edge of the pulse at four times: $t = 6M, 12M, 18M,$ and $24M$, where the time is measured as a multiple of GM/c^3 . The reduced speed of light at small radii compared to larger radii is evident in the plot for $t = 6M$ by the distortion from a perfect circle of the endpoints of the light ray pattern. With a knowledge of the disk structure (or, more likely, a model), one can imagine exploiting the unique light propagation physics in a black hole metric to locate the position of such a pulse as it irradiates different portions of the disk. Conversely, with a model of the origin for a pulse, or X-ray flare, the disk structure can be mapped, since the disk will respond to changes in the illumination pattern. Since such an effect occurs on a timescale that is measured in multiples of GM/c^3 , it is practical to observe “light echoes” in AGN (hundreds to thousands of seconds), but not in black hole X-ray binaries (~ 1 millisecond).

This leads to the concept of *reverberation mapping*, which is among the programs planned for future X-ray observatories, such as *Constellation-X*. We do not discuss the details of this ambitious goal here. However, a few comments are in order. Given that the model of X-ray fluorescence from AGN and black hole X-ray binaries involves the spectral response of an accretion disk to illumination by hard X rays, and that the hard X-ray continuum flux is observed to vary, it makes sense to ask whether changes in the shapes and intensities of fluorescence lines in response to continuum variability can elucidate both the nature of continuum production and disk structure. The basics of such a program, for the case of a Schwarzschild black hole, have been laid out in [139]. It was shown that a variable source of localized hard X-ray illumination placed at the center of a disk would cause a characteristic response in the profile of a fluorescence line. In this case, with a centrally-located illumination source, the inner disk would respond first, affecting the red and blue extremes of the profile. Owing to light travel times, the rest of the profile would respond at later times. It is shown that, in principle, the mass of the black hole can be determined. Measurements of black hole spin (see §6) are also plausibly within reach [140]. In a more general case, reverberation could involve a non-axial illumination source in the Kerr geometry, time-dependent modifications to the disk structure, and multiple, overlapping X-ray flares, with a distribution in both intensity and position. In such models, the varying speed of light propagation figures prominently. For example, as discussed in [141], non-axial variable illumination causes the redward portion of the line profile to lag the rest of the profile, indicative of an inward moving pulse that sweeps across the disk, slowing to zero velocity at the horizon.

Interestingly, current studies of AGN in which the X-ray continuum is observed to vary fail to show the expected variability in the iron $K\alpha$ line complex [142] [143] [144], although efforts attempting to reconcile this problem are underway [145].

5.8. Minimum and Maximum Frequency Shifts

Assume that a locally stationary observer measures the frequency distribution of a radiating particle that moves on a circular orbit at velocity v_ϕ and emits photons of frequency ν_o in its rest frame. The minimum and maximum frequencies measured by the LSO are determined by a Lorentz transformation:

$$\nu_{\text{iso}} = \gamma \nu_o (1 \pm v_\phi) \quad (67)$$

where v_ϕ is given by Eq. (39), and $\gamma = (1 - v_\phi^2)^{-1/2}$. Then from Eq. (22) we can find the frequency observed at infinity according to

$$\nu_\infty = \left(1 - \frac{2M}{r}\right)^{1/2} \nu_{\text{iso}}. \quad (68)$$

This is straightforward, and works out to

$$(\nu_\infty)^\pm = \nu_o \left(\frac{1 - 2M/r}{1 - 3M/r}\right)^{1/2} \left[(1 - 2M/r)^{1/2} \pm (M/r)^{1/2}\right]. \quad (69)$$

At the ISCO, we find $\nu_\infty^- = (\sqrt{2}/3)\nu_o$ and $\nu_\infty^+ = \sqrt{2}\nu_o$ [10]. This analysis also assumes that the observer at infinity sees the full red and blue shifts of the emitted photons. In more realistic cases, the line profile is narrower, since the disk is likely to be inclined.

Note that, although an observer at infinity marks the velocity of a circular orbit as being $v_\infty = \sqrt{M/r}$, we cannot properly calculate the photon energies (as above) unless we analyze the problem in the local frame of the orbiting matter. The lesson is that there is no Lorentz transformation that globally reduces curved spacetime to the Minkowski metric.

We revisit the minimum and maximum frequency shifts in a later section, after we derive the analogous quantities for Kerr black holes.

6. Spinning Black Holes – The Kerr Metric

We have already remarked on the ubiquity of angular momentum in the cosmos. Angular momentum is also likely to play a role in the behavior of spacetime near black holes. Stellar precursors to Galactic black holes rotate, thus imbuing these stars with angular momentum. Near the center of a galaxy, gas that supplies fuel to supermassive black holes in AGN is in motion, and thus carries angular momentum with respect to the black hole. In both cases, then, we expect the black hole to possess angular momentum. Therefore, improved treatments of the physics in the black hole environment should include modifications to the spacetime geometry induced by spin [147].

In 1963, Roy Kerr [148] presented his solution for the metric outside a spinning object at the First Texas Symposium on Relativistic Astrophysics (see [149] for a description of these proceedings). The physical implications of this solution were pursued over the course of the next few years. More recently, observable properties of the emission and timing properties of accretion disks have led to attempts to measure black hole spin.

The Kerr metric is given in Boyer-Lindquist coordinates [150] as

$$d\tau^2 = \left(1 - \frac{2Mr}{\Sigma}\right) dt^2 + \frac{4Mar \sin^2 \theta}{\Sigma} dt d\phi - \frac{\Sigma}{\Delta} dr^2 - \Sigma d\theta^2 - R_{a,\theta}^2 \sin^2 \theta d\phi^2, \quad (70)$$

where

$$\Sigma = r^2 + a^2 \cos^2 \theta$$

$$\Delta = r^2 - 2Mr + a^2 \quad (71)$$

$$R_{a,\theta}^2 = r^2 + a^2 + 2Mra^2 \Sigma^{-1} \sin^2 \theta.$$

For motion in the equatorial plane ($\theta = \pi/2$), the Kerr metric is

$$d\tau^2 = \left(1 - \frac{2M}{r}\right) dt^2 + \frac{4Ma}{r} dt d\phi - \frac{r^2}{\Delta} dr^2 - R_a^2 d\phi^2, \quad (72)$$

where

$$R_a^2 = r^2 + a^2 + \frac{2Ma^2}{r}. \quad (73)$$

We show below that R_a is the reduced circumference in the equatorial plane of a Kerr black hole.

6.1. The Kerr Event Horizon

The radial coordinate of the horizon r_H is defined as that radius at which the coefficient of the dr^2 term of the metric blows up. For the Kerr metric this occurs when $\Delta = 0$, which gives

$$r_H = M + \sqrt{M^2 - a^2}. \quad (74)$$

This shows us that the maximum spin consistent with a real-valued radial coordinate for the horizon is simply M . The radial coordinate of the horizon thus ranges from $2M$ ($a = 0$) down to M ($a = M$). Detailed considerations concerning the spin-up of a black hole by accreting matter shows that the maximum spin is not M , but rather $0.998M$ [151]. The case $a = M$ (or $a = 0.998M$) is referred to as an *extreme Kerr black hole*, and the black hole is said to be *maximally spinning*.

6.2. The Static Limit and the Dragging of Inertial Frames

The following derivation follows that in [10]. The relation $g_{\mu\nu}p^\mu p^\nu = -m^2$ is equivalent to the condition $g_{\mu\nu}u^\mu u^\nu = -1$, where u^μ is a component of the velocity four-vector. Consider an observer at fixed r and θ , so that $dr = 0$ and $d\theta = 0$. Then

$$g_{tt}(u^t)^2 + 2g_{t\phi}u^t u^\phi + g_{\phi\phi}(u^\phi)^2 = -1, \quad (75)$$

where the metric coefficients can be read off from Eq. 70. Rearrangement of the previous equation gives

$$(u^t)^2 \left[g_{tt} + 2g_{t\phi} \frac{u^\phi}{u^t} + g_{\phi\phi} \frac{(u^\phi)^2}{(u^t)^2} \right] = -1. \quad (76)$$

If we let $u^\phi/u^t = d\phi/dt \equiv \omega$, then we require

$$\omega^2 + 2 \frac{g_{t\phi}}{g_{\phi\phi}} \omega + \frac{g_{tt}}{g_{\phi\phi}} < 0. \quad (77)$$

This restricts ω to the range

$$\frac{|g_{t\phi}|}{g_{\phi\phi}} \left[1 - \sqrt{1 - \frac{g_{tt}g_{\phi\phi}}{g_{t\phi}^2}} \right] \leq \omega \leq \frac{|g_{t\phi}|}{g_{\phi\phi}} \left[1 + \sqrt{1 - \frac{g_{tt}g_{\phi\phi}}{g_{t\phi}^2}} \right], \quad (78)$$

or $\omega_{\min} < \omega < \omega_{\max}$. Note that $g_{t\phi}$ is always negative, and that $g_{\phi\phi}$ is always positive. The metric coefficient g_{tt} can be positive or negative:

$$g_{tt} < 0 \text{ if } r > M + \sqrt{M^2 - a^2 \cos^2 \theta} \quad (79)$$

$$g_{tt} > 0 \text{ if } M < r < M + \sqrt{M^2 - a^2 \cos^2 \theta}.$$

Thus whenever $g_{tt} > 0$ (small radii), we see that $\omega_{\min} > 0$; the observer is swept around the black hole, and no action on the part of the observer can change that. Where $g_{tt} < 0$ (large radii), $\omega_{\min} < 0$, and retrograde motion is allowed. The critical boundary, the mathematical surface inside which matter is dragged irresistibly in the prograde direction is called the *static limit*, which, from Eq. 79 is

$$r_{\text{stat}} = M + \sqrt{M^2 - a^2 \cos^2 \theta}, \quad (80)$$

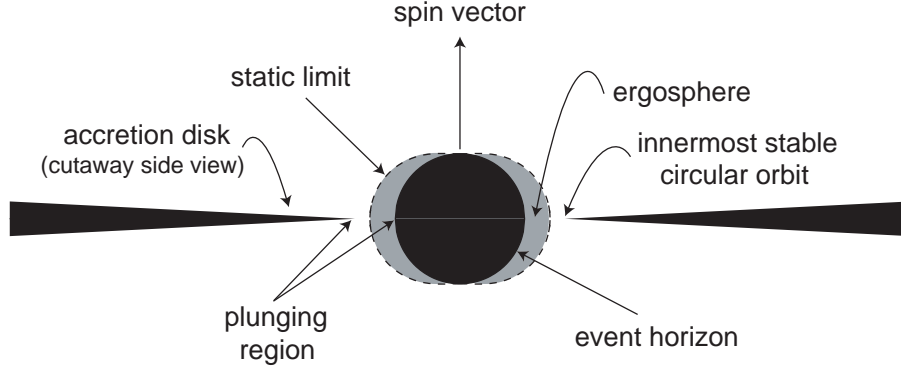


Fig. 9. Schematic of a disk-accreting Kerr black hole ($a = 0.9M$) in cross-section, using t, r, θ, ϕ coordinates, illustrating various geometric relations. The dark circle is the black hole, bounded by its event horizon. The gray region, delineated by the horizon and the static limit (dashed lines) is the ergosphere, cylindrically symmetric with respect to the spin vector. The accretion disk is assumed to lie in the equatorial plane of the hole. The disk is truncated near the hole according to the radius of the innermost stable circular orbit appropriate to the spin. Inside the ISCO, matter free falls through the plunging region and crosses the horizon. Tapering of the disk is schematic only, suggesting a general trend of geometrical thickening with radius. Also, see Fig. (12).

which corresponds to $g_{tt} = 0$.

The peculiar behavior of spacetime near the static limit can be illustrated [152] if we imagine launching light pulses in the azimuthal direction, first in the prograde direction, then in the retrograde direction, at some radius r near a spinning black hole. We wish to find $d\phi/dt$, the angular velocity of the light pulse according to distant observers, for these two cases. For simplicity, we work in the equatorial plane. Then, with $\theta = \pi/2$, $dr = 0$, $d\theta = 0$, and the condition $g_{\mu\nu}u^\mu u^\nu = 0$, we find the following quadratic for $d\phi/dt$,

$$R_a^2 \left(\frac{d\phi}{dt} \right)^2 - \frac{4Ma}{r} \frac{d\phi}{dt} - \left(1 - \frac{2M}{r} \right) = 0, \quad (81)$$

which has the solution

$$\frac{d\phi}{dt} = \frac{2Ma}{rR_a^2} \left[1 \pm \sqrt{1 - \frac{r^2 R_a^2}{4M^2 a^2} \left(1 - \frac{2M}{r} \right)} \right]. \quad (82)$$

From Eq. 80, the static limit in the equatorial plane is $r_{\text{stat}} = 2M$, which, when substituted into Eq. 82, gives the two solutions $d\phi/dt = 4Ma/rR_a^2 = a/(a^2 + 2M^2)$ and $d\phi/dt = 0$. The pulse emitted in the retrograde direction appears to stand still. Inside the static limit, retrograde pulses appear, in fact, to move initially in the prograde direction. Although we do not pursue it here, it is worth noting that the region between the static limit and the horizon is called the *ergosphere*, after the Greek word *ergon*, for work, since energy can, in principle, be extracted from it [153]. An illustration of the size and shape of the ergosphere is shown in Fig. (9), along with other components of an accreting black hole.

An expression for the rate at which spacetime is dragged around a spinning black hole can be derived from the momentum conservation law, which, as in §6 for the Schwarzschild metric, we derive from the Euler-Lagrange equation for ϕ . A suitable Lagrangian for motion in the equatorial plane is given by

$$\Lambda = -\frac{1}{2} \left(1 - \frac{2M}{r} \right) \dot{t}^2 - \frac{2Ma}{r} \dot{t} \dot{\phi} + \frac{r^2}{2\Delta} \dot{r}^2 + \frac{R_a^2}{2} \dot{\phi}^2, \quad (83)$$

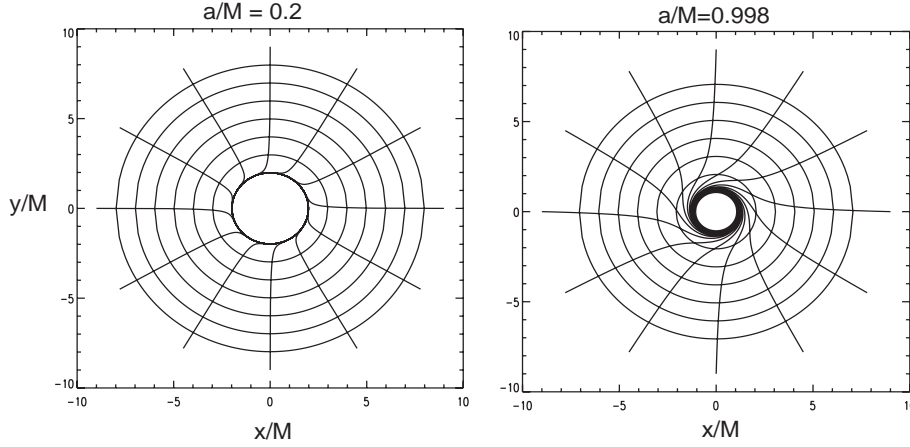


Fig. 10. Plots of photon trajectories with zero angular momentum near a Kerr black hole, for $a = 0.2M$ (left panel) and $a = 0.998M$ (right panel) illustrating the frame dragging effect. Circles are lines of constant r . Plots are based on integrations of Eq. 116.

where the dot denotes differentiation with respect to any parameter p along the particle's world line [10]. The Euler-Lagrange equation for the ϕ -coordinate results in

$$R_a^2 \frac{d\phi}{dp} - \frac{2aM}{r} \frac{dt}{dp} = L. \quad (84)$$

If $dp = d\tau/m$, then we find an expression that can be compared to the case for the Schwarzschild metric (Eq. 26),

$$R_a^2 \frac{d\phi}{d\tau} = \frac{L}{m} + \frac{2aM}{r} \frac{dt}{d\tau}. \quad (85)$$

to which it reduces for $a \rightarrow 0$. The second term on the right, which is proportional to the black hole spin, shows that a particle with $d\phi/d\tau = 0$ must have negative angular momentum. In fact, for massive particles and massless particles alike, if $L = 0$, then

$$\frac{d\phi}{dt} = \frac{2aM}{rR_a^2} \equiv \omega_{\text{drag}}. \quad (86)$$

According to a distant observer, a particle with zero angular momentum appears to rotate in the direction of the black hole spin (i.e., following the right-hand rule). This effect is known as the *dragging of inertial frames*. The drag frequency increases with decreasing radius. Frame dragging can also be described as follows: Imagine yourself in a rocket near a spinning black hole. Looking at the fixed stars for reference, you find that you require a thrust in the positive azimuthal direction (i.e., pointed toward the spin direction) to hold the rocket in a position such that the stars overhead appear not to move. It is said that spacetime itself is moving.

The dragging of inertial frames occurs outside of any spinning body. As an example, we use Eq. (86) to estimate ω_{drag} caused by the Earth's rotation. In conventional units, the drag frequency at the Earth's surface is $\omega_{\text{drag}} \approx 2GI\omega_E/(c^2R_E^3)$, where I is Earth's moment of inertia, R_E is its radius, and ω_E is its rotation frequency. The moment of inertia of the Earth is $0.33M_ER_E^2$ [8], where the deviation from 2/5 in the multiplier is due to the non-uniform density distribution of Earth's mass. Taking $M_E = 6.0 \times 10^{27}$ g, $R_E = 6.4 \times 10^8$ cm, and $\omega_E = 7.3 \times 10^{-5}$ s $^{-1}$, we find $\omega_{\text{drag}} = 219$ mas yr $^{-1}$, large enough to be measured with current technology. Recently, the LAGEOS mission, a pair of

laser-ranged satellites on orbits with aphelia of approximately 12,000 km, measured ω_{drag} , finding a value that is 99 ± 5 percent of the value predicted by GR [154]. Gravity Probe-B is expected to reduce the uncertainty in the measurement to 1%.

Interestingly, we find for the Earth that $a = 7.3 \times 10^2 M_E$. The restriction $a \leq M$ is clearly not a general constraint on material bodies; instead, it can be viewed as a necessary condition for matter lying inside its event horizon.

6.3. Gravitational Redshift in the Kerr Metric

In the Schwarzschild metric, we found the relation between proper time and coordinate time by considering two stationary observers at different radii, and found that the tt -component of the metric contained the necessary information. An analogous approach in the Kerr metric involves an observer, called a *zero angular momentum observer* (ZAMO), moving along the ϕ -direction with an angular velocity ω_{drag} given by Eq. 86. By a simple transformation, the metric can be diagonalized, i.e., we can decouple the t and ϕ coordinates, then relate dt to $d\tau$. Let $d\phi = \omega_{\text{drag}} dt + d\phi_r$, where $d\phi_r$ is an azimuthal displacement measured in the ZAMO frame. The case of greatest interest is that of an emitter in the equatorial plane. Therefore, for pure azimuthal motion, Eq. (72), with $dr = 0$, becomes

$$d\tau^2 = \left(1 - \frac{2M}{r}\right) dt^2 + \frac{4Ma}{r} dt d\phi - R_a^2 d\phi^2. \quad (87)$$

Substituting the $d\phi$ transformation into this form of the metric yields a new metric that uncouples the t - and ϕ -coordinates:

$$d\tau^2 = \left(1 - \frac{2M}{r} + \frac{4M^2 a^2}{r^2 R_a^2}\right) dt^2 - R_a^2 d\phi_r^2. \quad (88)$$

This shows that the reduced circumference in the equatorial plane of a Kerr hole, the analog of r used to describe the Schwarzschild geometry, is R_a . Equation (88) gives us the relation between time for a ZAMO (set $d\phi_r = 0$) and a distant observer, which we write as a redshift formula for frequency:

$$\nu_\infty = \nu_o \left(1 - \frac{2M}{r} + \frac{4M^2 a^2}{r^2 R_a^2}\right)^{1/2}, \quad (89)$$

or, after expanding R_a , and rearranging,

$$\nu_\infty = \nu_o \left(\frac{r^2 + a^2 - 2Mr}{r^2 + a^2 + 2Ma^2/r}\right)^{1/2}, \quad (90)$$

which reduces to Eq. (22) in the limit $a \rightarrow 0$, the Schwarzschild case. As a consistency check, note that the surface of infinite redshift, the outer solution of $r^2 + a^2 - 2Mr = 0$, is identical to our earlier result, Eq. (74).

The multiplier of ν_o in Eq. (90) is sometimes called the *lapse function*. Since we use this function later in the calculation of orbital velocities, it is defined here and given the label α :

$$\alpha = \frac{\sqrt{r^2 + a^2 - 2Mr}}{R_a}. \quad (91)$$

6.4. Circular Orbits in the Kerr Potential

Evaluation of the Euler-Lagrange equation for t provides an energy constant of the motion,

$$\left(1 - \frac{2M}{r}\right) \dot{t} + \frac{2Ma}{r} \dot{\phi} = E, \quad (92)$$

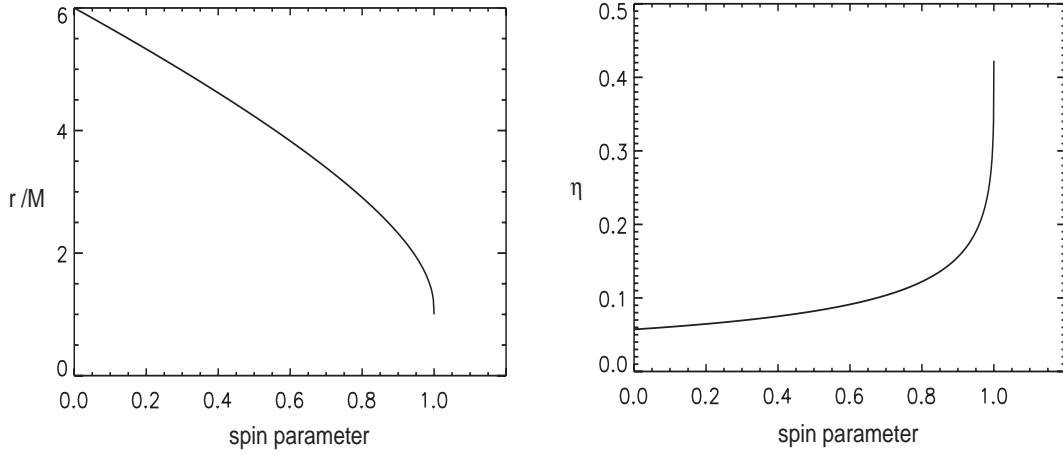


Fig. 11. (Left panel) Radius of innermost stable circular orbit plotted against the spin parameter a_* . Radii of the ISCOs range from $6M$ ($a_* = 0$) to M ($a_* = 1$). For physically realizable Kerr black holes, the maximum spin is $a_* = 0.998$, corresponding to an ISCO radius of $1.24M$. (Right panel) Dimensionless accretion efficiency η plotted against a_* . Efficiency ranges from 0.057 ($a_* = 0$) to 0.42 ($a_* = 1$). For $a_* = 0.998$, $\eta = 0.34$.

using the Lagrangian in Eq. (72). We have already evaluated the $\dot{\phi}$ component (Eq. 84), which we reproduce here,

$$-\frac{2Ma}{r}\dot{t} + R_a^2\dot{\phi} = L. \quad (93)$$

These two equations can be solved for \dot{t} and $\dot{\phi}$ in terms of the energy and angular momentum, yielding

$$\dot{t} = \frac{ErR_a^2 - 2LMa}{r\Delta} \quad (94)$$

$$\dot{\phi} = \frac{L(r - 2M) + 2EMa}{r\Delta}. \quad (95)$$

Substitution of Eqs. (94) and (95) into the Lagrangian (Eq. 83), noting that $\Lambda = -m^2/2$, yields an equation for \dot{r} , which we write in terms of $dr/d\tau$, substituting $p = \tau/m$,

$$r^3\left(\frac{dr}{d\tau}\right)^2 = S \equiv \left(\frac{E}{m}\right)^2 rR_a^2 - 4Ma\left(\frac{L}{m}\right)\left(\frac{E}{m}\right) - (r - 2M)\left(\frac{L}{m}\right)^2 - r\Delta. \quad (96)$$

Stable circular orbits can be found by imposing three conditions on S : (1) $S = 0$ (turning point); (2) $\partial S/\partial r = 0$ (circle); (3) $\partial^2 S/\partial r^2 \leq 0$ (stability). The first two conditions yield a system of two equations that can be solved for E/m and L/m , restricting those quantities for a given r and a :

$$\frac{E}{m} = \frac{r - 2M + a\sqrt{M/r}}{(r^2 - 3Mr + 2a\sqrt{Mr})^{1/2}}, \quad (97)$$

$$\frac{L}{m} = \left(\frac{M}{r}\right)^{1/2} \frac{r^2 - 2a\sqrt{Mr} + a^2}{(r^2 - 3Mr + 2a\sqrt{Mr})^{1/2}}. \quad (98)$$

The third condition requires that

$$\left(\frac{E}{m}\right)^2 - 1 + \frac{2M}{3r} \leq 0. \quad (99)$$

Substituting from Eq. 97, and defining the dimensionless *spin parameter* $a_* = a/M$, the previous restriction becomes

$$\left(\frac{r}{M}\right)^2 - 6\frac{r}{M} + 8a_*\left(\frac{r}{M}\right)^{1/2} - 3a_*^2 \geq 0, \quad (100)$$

where the equality can be treated as a quartic equation in $(r/M)^{1/2}$. The quartic has been solved [146] for the radius of the innermost stable circular orbit for a specified spin parameter:

$$r_{\text{isco}} = M \left[3 + Z_2 - \sqrt{(3 - Z_1)(3 + Z_1 + 2Z_2)} \right], \quad (101)$$

where Z_1 and Z_2 are defined by

$$\begin{aligned} Z_1 &= 1 + (1 - a_*^2)^{1/3} [(1 + a_*)^{1/3} + (1 - a_*)^{1/3}] \\ Z_2 &= (Z_1^2 + 3a_*^2)^{1/2}. \end{aligned} \quad (102)$$

Equation (101) generalizes the result based on Eq. (31) for the Schwarzschild metric. As shown in the left panel of Fig. (11), r_{isco} is a monotonically decreasing function of spin, ranging from a maximum of $6M$ for a Schwarzschild hole to a minimum of M for a maximally-spinning Kerr hole. In Fig. (12) we show schematically the variation of the position of the ISCO of an accretion disk compared to the size of the event horizon and the shape of the ergosphere, where, for example, it is seen that for large values of a_* the ISCO lies inside the ergosphere, and approaches the event horizon.

If we assume that the accretion efficiency η is determined by the energy of the innermost stable circular orbit, then the maximum efficiency occurs for the case of maximal spin. With $r = M$ and $a = M$, Eq. (97) gives $E/m = 1/\sqrt{3}$. Therefore, for a disk extending down to r_{isco} for a maximally spinning black hole, the accretion efficiency is

$$\eta(a_* = 1) = \Delta\left(\frac{E}{m}\right) = 1 - \left(\frac{1}{3}\right)^{1/2} \approx 0.423, \quad (103)$$

which can be compared to Eq. (35) for the Schwarzschild metric. The energy conversion efficiency η is plotted as a function of the spin parameter a_* in the right panel of Fig. (11).

The velocity of matter in a circular orbit around a Kerr black hole, as measured by a ZAMO, can be expressed in terms of the orbit's angular frequency as reckoned by a distant observer (Ω) as

$$v_\phi = \frac{R_a}{\alpha} (\Omega - \omega_{\text{drag}}), \quad (104)$$

where R_a (Eq. 73) is the reduced circumference of a spinning hole, ω_{drag} (Eq. 86) corrects for the dragging of inertial frames, and the lapse function α (Eq. 91) accounts for the transformation between measures of time. An expression for Ω [155] [156] is most easily found by starting with the equation of motion

$$\frac{d^2 x^\lambda}{d\tau^2} + \Gamma_{\mu\nu}^\lambda \frac{dx^\mu}{d\tau} \frac{dx^\nu}{d\tau} = 0, \quad (105)$$

where the *Christoffel symbols* are given in terms of the metric $g_{\mu\nu}$ and the inverse metric $g^{\mu\nu}$ by

$$\Gamma_{\mu\nu}^\lambda = \frac{1}{2} g^{\eta\lambda} \left[\frac{\partial g_{\nu\eta}}{\partial x^\mu} + \frac{\partial g_{\mu\eta}}{\partial x^\nu} - \frac{\partial g_{\nu\mu}}{\partial x^\eta} \right], \quad (106)$$

whose derivation can be found in [137]. For a circular orbit, using Eqs. (94) and (95), the first term on the left of Eq. (105) vanishes for all λ . If we choose $\lambda = r$, then

$$\Gamma_{\mu\nu}^r dx^\mu dx^\nu = \Gamma_{tt}^r dt^2 + 2\Gamma_{\phi t}^r dt d\phi + \Gamma_{\phi\phi}^r d\phi^2 = 0, \quad (107)$$

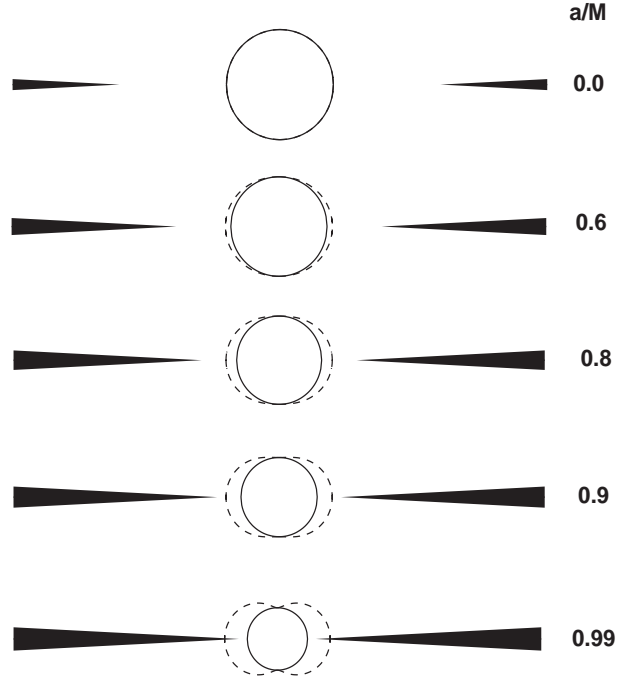


Fig. 12. Comparison of the radius of the event horizon (*solid circles*), the static limit (*dashed lines*) and ergosphere, and position of the innermost stable circular orbit for black holes of various spin parameters.

or, letting $\Omega = d\phi/dt$,

$$\Gamma_{\phi\phi}^r \Omega^2 + 2\Gamma_{\phi t}^r \Omega + \Gamma_{tt}^r = 0. \quad (108)$$

An evaluation of the Christoffel symbols gives

$$\begin{aligned} \Gamma_{tt}^r &= \frac{1}{2}g^{rr}(2M/r^2) \\ \Gamma_{\phi t}^r &= \frac{1}{2}g^{rr}(-2Ma/r^2) \\ \Gamma_{\phi\phi}^r &= \frac{1}{2}g^{rr}(2Ma^2/r^2 - 2r), \end{aligned} \quad (109)$$

which, when substituted into Eq. (108), leaves us with the simple quadratic equation

$$\left(\frac{Ma^2}{r^2} - r\right)\Omega^2 - \frac{2Ma}{r^2}\Omega + \frac{M}{r^2} = 0. \quad (110)$$

The solution corresponding to prograde motion is

$$\Omega = \frac{\sqrt{M/r}}{r + a\sqrt{M/r}} = \frac{1}{M} \frac{1}{(r/M)^{3/2} + a_*}. \quad (111)$$

This expression for Ω can also be derived by taking the ratio of $\dot{\phi}$ and \dot{t} from Eqs. (95) and (94), respectively, then substituting for E and L from Eqs. (97) and (98), respectively, but the algebra is tedious.

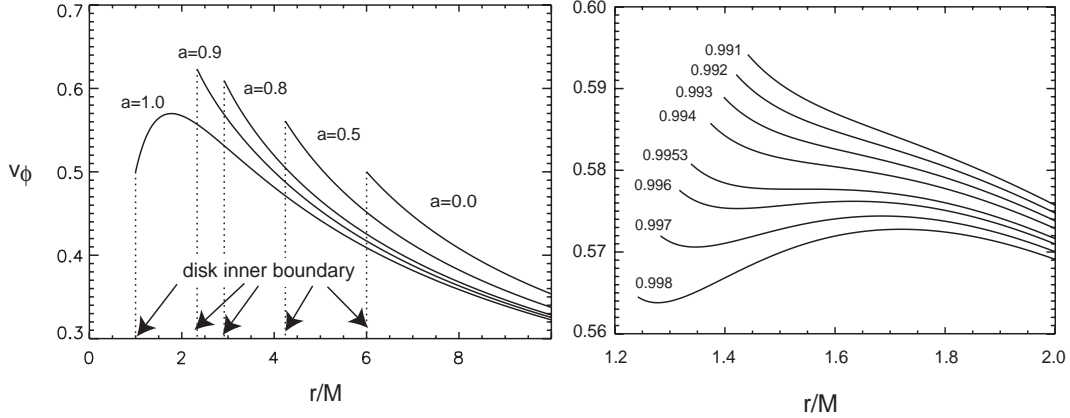


Fig. 13. (Left panel) Azimuthal velocities for equatorial circular orbits as a function of radius for five values of black hole spin, as measured by locally stationary observers. Curves are labeled by the spin as fractions of M . Vertical lines indicate radii corresponding to the innermost stable circular orbit. (Right panel) Azimuthal velocities for a selected group of spin parameters (as labeled), illustrating the development of a local minimum for $a_* > 0.9953$.

Substituting Eqs. (73), (86), (91), and (111) into Eq. (104) yields an expression for the velocity of circular orbits [146],

$$v_\phi = \left(\frac{M}{r}\right)^{1/2} \frac{r^2 - 2a\sqrt{Mr} + a^2}{(r + a\sqrt{M/r})\sqrt{r^2 - 2Mr + a^2}}, \quad (112)$$

which reduces to the Schwarzschild case, Eq. (39), for $a = 0$. For the other limit, $a \rightarrow M$, the numerator can be factored to give

$$v_\phi = \left(\frac{M}{r}\right)^{1/2} \frac{r^{3/2} + M^{1/2}r + Mr^{1/2} - M^{3/2}}{(r + M^{3/2}r^{-1/2})(r^{1/2} + M^{1/2})}, \quad (113)$$

which shows that as $r \rightarrow M$, the velocity approaches $v_\phi = 1/2$, which is, perhaps surprisingly, identical to the velocity at the ISCO of a Schwarzschild black hole. The left panel of Fig. (13) shows the radial profile of $v_\phi(r)$ for several different spin parameters. The maximum orbital velocity attained is $v_\phi^{\max} = 0.624$ for $a_* = 0.9268$, which occurs at the ISCO with $r_{\text{ISCO}} = 2.14M$.

Another feature worth noting is that for the extreme $a = M$ case, the maximum velocity is approached from above, i.e., $v_\phi(r)$ is not monotonic. For more realistic cases, where the maximum value of a_* is 0.998, the velocity at the ISCO is always approached from below. But this velocity is not always the maximum velocity. For $a_* = 0.9964$ and above, the radius of maximum velocity $r(v_{\max})$ is distinct from the ISCO, as can be seen in the right panel of Fig. (13) (lowest two curves), with the largest separation $r(v_{\max}) - r_{\text{ISCO}}$ occurring for the maximally spinning case, where $r(v_{\max}) = 1.72M$ and where $v_{\max} = 0.573$. The non-monotonic behavior of $v_\phi(r)$ sets in for $a_* > 0.9953$. For a_* in this range, $v_\phi(r)$ has a local minimum that moves inward as the spin parameter increases. Recently, it was proposed [157] that this feature of v_ϕ may be related to the fixed ratio of high frequency quasi-periodic oscillations (QPOs) observed in Galactic black hole X-ray binaries.

Having obtained formulae for the gravitational redshift (Eq. 90) and the velocities of circular orbits (Eq. 112), we now follow the same procedure used for Schwarzschild black holes (§5.8) to find the

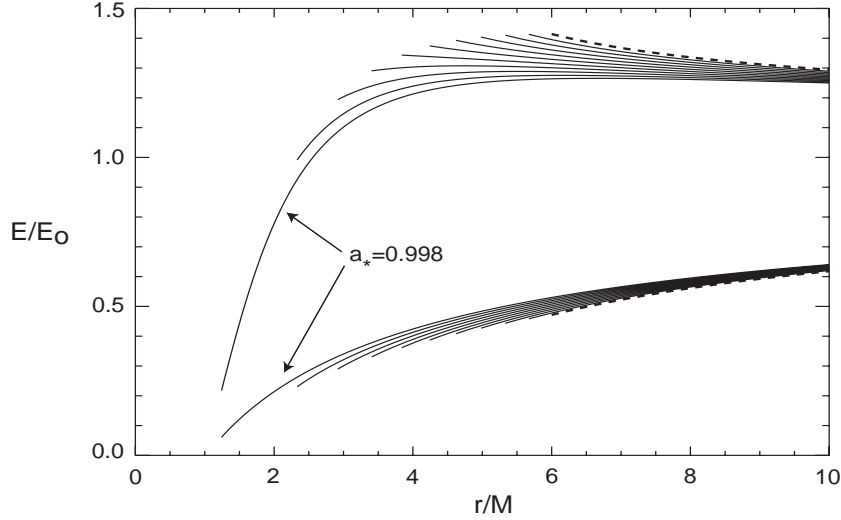


Fig. 14. Minimum and maximum normalized line energies observed at infinity vs. disk radius for several black hole spin parameters, assuming circular orbits and 90 degree inclination. The upper set of curves shows the maximum blueshifts for the eleven spin parameters $a_* = [0., 0.1, 0.2, 0.3, 0.4, 0.5, 0.6, 0.7, 0.8, 0.9, 0.998]$, working downward from the dashed line (Schwarzschild case). The lower set of curves shows the corresponding maximum redshifts, working upward from the $a_* = 0$ case. Pairs of curves delineate the maximum width of the line profile for a given radius, neglecting thermal Doppler widths, and any possible radiative transfer effects. Curves are truncated at the ISCO corresponding to each spin parameter.

minimum and maximum line energies as observed at infinity as a function of radius for several spin parameters. The result is shown in Fig. (14), where the extrema are plotted against radius for eleven values of the spin parameter. From that figure one sees that the differences between spinning black holes and a Schwarzschild black hole are fairly minor for $r > 6M$, viz., the maximum extent of the blue wing is the same to within about 10%, for $r > 6M$, and the maximum redshift is even less distinct when comparing different spins. If, for example, the disk of a maximally spinning hole did not, for some reason, produce line emission inside of about $6M$, one would be hard-pressed to discern spin by measuring the line width alone. Figure (14) also shows that the line width is bounded by the Schwarzschild “envelope” for $r > 6M$ (dashed line). The maximum blueshift is a monotonically decreasing function of spin; the maximum blueshift never exceeds the spin-zero case $E/E_o = 1.41$ at $r = 6M$, which may be surprising. For a given spin, and moving to smaller radii, the modest change in the maximum blueshift illustrates the trade-off between increasing orbital velocity and increasing gravitational redshift. For large spin values, the maximum blueshift is actually redshifted from line center, showing the dominant effect of gravitational redshift. Thus the radius of maximum blueshift is not always the innermost stable circular orbit. This is most obvious for maximally spinning holes, where the energy of the blue side of the line approaches $\approx 0.2E_o$, since the ISCO approaches the event horizon. The maximum redshift always occurs at the ISCO, with the minimum value of E/E_o being 0.060 for $a_* = 0.998$. The maximum redshift increases monotonically with spin, since the effects of increasing velocity and increasing gravitational redshift reinforce each other, rather than offset each other, as they do when evaluating the maximum blueshift. One also sees from the figure that the total line width changes with radius. For example, an emission profile from an annulus near $r = 2M$ in a maximally spinning hole would appear relatively narrow, with a highly redshifted centroid energy. The narrowing of the line follows from the overwhelming effect of gravitational redshift as the ISCO

approaches the event horizon.

In any realistic situation, one expects fluorescence from a large range of radii. A model line profile is built up annulus by annulus, where account is taken of the intrinsic surface brightness variation, the fraction of emitted photons that escape the system and find their way to the observer (given light bending), and the dynamical aspects discussed above. These model profiles can then be compared to spectroscopic data, which, in principle, allows one to extract several parameters of interest (disk inclination, radial emissivity profile, disk inner edge, etc.). Considered as a diagnostic of black hole spin, the distinguishing characteristic of line emission is, from Fig. (14), the extent of the red wing. By contrast, the blue wing is more sensitive to the inclination than to the spin. Given an observed line profile, the inclination, to a first approximation, can be determined by the position of the blue edge. The spin can then be estimated from the redward extent of the line profile. It's not quite that easy, unfortunately, but computer programs allowing fits to relativistic line profiles exist and are in wide use (e.g., [21] [158]), made available, for example, as part of the XSPEC [159] or ISIS [160] data analysis packages.

The detection of highly redshifted iron $K\alpha$ emission has led to inferences of non-zero spin, and has given rise to the idea that X-ray lines can be used to measure black hole spin. A dramatic example of a red-shifted iron $K\alpha$ line profile has been documented for the Seyfert 1 galaxy MCG-6-30-15 [161] [162], in which the line profile was observed to vary dramatically, from a profile for which the emission appeared to be dominated by large radii, and then to a profile in which the bulk of the emission was observed to lie below the rest energy. This latter result implies that the emission originated from $r < 6M$, which, given the assumption that radiation from within the ISCO is unobservable, implies black hole spin. In fact, a fit to the data requires $a_* > 0.94$ [163].

6.5. The Plunging Region

As orbiting matter in accretion disk reaches the ISCO, it is typically assumed to lose all rotational support and free fall from there through the event horizon. In terms of test particle trajectories, the gradually shrinking circular orbits are replaced by a rapid spiraling infall. We can calculate such a trajectory by eliminating $d\tau$ between Eqs. (27) and (28), from which we find the following expression for the trajectory of a test particle in the Schwarzschild metric:

$$\frac{dr}{d\phi} = \pm \frac{r^2}{L/m} \left[\left(\frac{E}{m} \right)^2 - \left(1 - \frac{2M}{r} \right) \left(1 + \frac{(L/m)^2}{r^2} \right) \right]^{1/2}. \quad (114)$$

If we set $E/m = \sqrt{8/9}$ and $L/m = 2\sqrt{3}M$, the values for a circular orbit at the ISCO, then add a slight radial displacement inward, an orbit such as that shown in Fig. (15) results.

The sudden increase in radial velocity results in a reduced disk optical depth, which may reduce the X-ray albedo. The free falling matter is also conventionally assumed to be stress-free, so that a hot corona cannot be supported within the ISCO. Therefore, irradiation inside the ISCO by hard X rays is reduced relative to matter at larger radii. Finally, the drop in density may imply an increase in ξ , which reduces the overall efficiency of fluorescence line production. Taken together, these aspects of disks imply that any fluorescence must occur outside the ISCO. In other words, the radii over which observable fluorescence emission originates has a hard inner limit of $r = 6M$ for a Schwarzschild black hole. Given such a constraint, the assumption of a zero-spin black hole therefore limits the maximum redshift of the line profile (see Fig. 14). Profiles violating this limit have thus been taken to imply spin (see §6.4).

The whole concept of a clearly demarcated inner disk edge has recently been called into question, based both upon test particle trajectories [164] and upon three-dimensional MHD simulations of accretion disks [165]. In the former paper, with a source of hard X-ray illumination located on the axis above the disk plane, it was found that substantial fluorescence line flux from inside the ISCO may

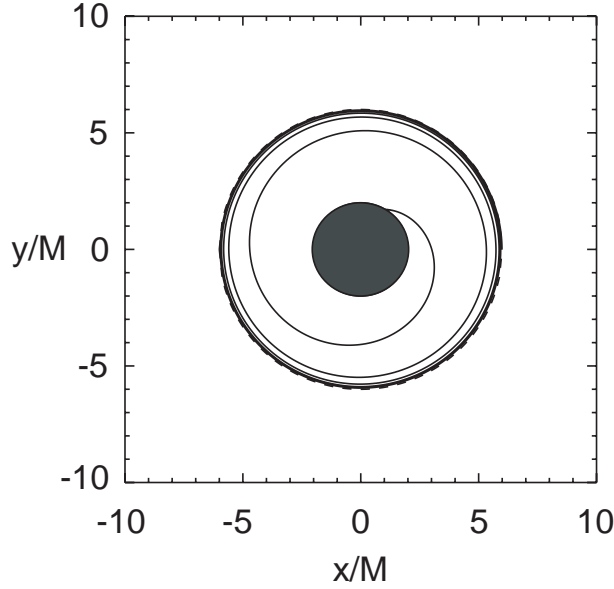


Fig. 15. Trajectory of free falling test particle inside the innermost stable circular orbit — the plunging region — of a Schwarzschild black hole (see Eq. 114) according to an observer at infinity. The energy and angular momentum are set to the corresponding values at $r = 6M$. In order to perturb the particle off the stable orbit at $r = 6M$, the initial radius was set to $5.99M$.

emerge from the system, and that this component of the flux appears at redshifts exceeding the usual limit imposed by a hard cutoff at $r = 6M$, thus mimicking emission from a spinning black hole. The importance of emission from inside the ISCO of a non-spinning hole has been contested [140], however, based upon the absence of an iron K absorption edge in the well-studied source MCG–6-30-15 that is predicted by modeling calculations. In [165] stress is found to be continuous across the ISCO, invalidating the usual assumption that the stress vanishes there. Moreover, it was found that the matter density distribution need not conform to the simpler model wherein the density decreases monotonically with decreasing radius, but that clumpiness may permit the survival of matter with lower values of ξ . Thus there is some doubt cast upon our ability to make clean measurements of black hole spin using the iron $K\alpha$ profile alone.

6.6. The Motion of Light in the Kerr Metric

A general treatment of light motion in the Kerr metric is considerably more complex than the Schwarzschild case (see, e.g. [166]). For example, except for the case of motion in the equatorial plane, trajectories are non-planar (see Fig. 16). Discussions of the techniques used to calculate photon geodesics near Kerr black holes may be found in [166] [167] [168] [169].

We can, however, work out the relatively simple example of a massless particle with $L = 0$ moving in the equatorial plane of a spinning black hole. We find an expression for $dr/d\phi$ from the following two equations:

$$R_a^2 d\phi - (2Ma/r) dt = 0 \tag{115}$$

$$(1 - 2M/r) dt^2 + (4Ma/r) dt d\phi - (r^2/\Delta) dr^2 - R_a^2 d\phi^2 = 0.$$

The first of this set comes from Eq. (84) with $L = 0$, and the second is simply the metric (Eq. 72) with

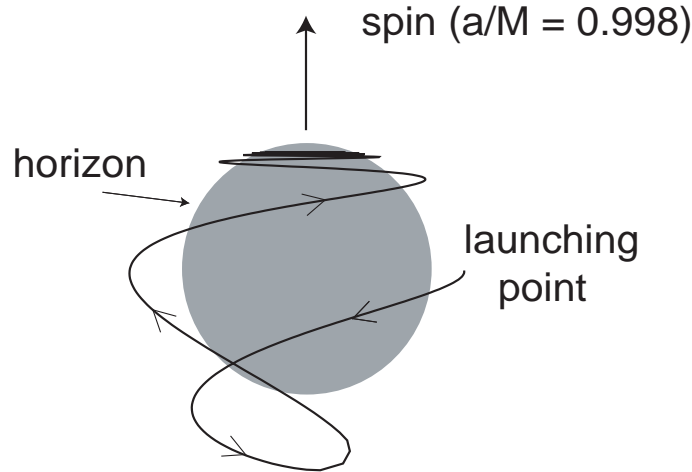


Fig. 16. Trajectory for a massless test particle near a maximally spinning black hole, showing the generally non-planar character of photon trajectories in the Kerr spacetime. The path is projected onto the x - z plane, in which the angular momentum vector of the black hole lies. Photon is launched from $r = 1.27R_g$, with an initial momentum vector predominantly in the positive y -direction, with a small positive x component and a small negative z component. The photon executes several “circuits” before impacting the horizon near the pole. The calculation was performed following the methods described in [166].

$d\tau = 0$. Equation (115) is a system of two equations in the variables dt , dr , and $d\phi$. By eliminating dt , we arrive at an expression involving only dr and $d\phi$ that describes the photon trajectory:

$$\frac{dr}{d\phi} = \pm \frac{R_a \Delta}{2Ma}, \quad (116)$$

for which a straightforward numerical integration produces the plots shown in Fig. (10), where trajectories for $L = 0$ photons follow the spacetime drag for two values of the spin parameter.

7. X-ray Fluorescence Spectroscopy of Accreting Black Holes

Having introduced the basic aspects of GR and accretion disk theory, we look now at the production of X-ray fluorescence line emission in black hole accretion disks. We start with a brief discussion of photoionization codes, and introduce the ionization parameter concept. Then we treat the phenomenon of “reflection,” the spectral response of an optically thick medium to irradiation by a hard X-ray source. We close the section by presenting a few aspects of fluorescence at the atomic scale. The treatment of the latter topic is primarily from the point of view of atomic modeling, rather than from a quantum mechanical standpoint.

7.1. X-Ray Photoionization Codes

Photoionization codes, such as those described in references [172] and [173], are used to determine the effect of a radiation field on a gas of specified chemical composition, and the self-consistent effect that passage through the gas has on the radiation field. In other words, the opacity determines the effect of the gas on the radiation field, but the radiation field partly determines the opacity, primarily through its influence on the charge state distribution (ionization balance) [174]. In addition to acting as the dominant agent of ionization, photoionization also heats the plasma, since suprathreshold photoelectrons are thermalized after interacting with the local population of Maxwellian-distributed electrons. Compton

scattering and the Auger effect (see below) also contribute to plasma heating. One may add a source of non-ionizing heating to mimic the sum of various other processes [175]. Plasma cooling is primarily through recombination, collisionally-excited line emission, bremsstrahlung, and inverse Compton scattering. Also, imposing the constraint of charge neutrality controls the overall free electron to ion ratio. The explicit calculation of heating and cooling thus couples the energy equation (*radiative heating = radiative cooling*) to the ionization equations and the neutrality equation, constituting a complex system of equations, whose solution requires an iteration scheme.

Three approaches to calculating level populations can be used: (1) the nebular approximation, in which only the ground state has a significant population, (2) the Saha-Boltzmann approach, in which the populations of excited levels k are given by $n_k = (g_k/g_1) \exp(-E_k/kT_e)$, where g denotes the statistical weight factor, E_k is the level energy with respect to ground, and kT_e is the local electron temperature, and (3) detailed level accounting, where level populations are calculated explicitly by diagonalizing the rate matrix, the elements of which include all rates into and out of each level, thus requiring many thousands of atomic rate coefficients. Once the level populations are specified, the local contribution to the overall spectrum is determined. Finally, by more or less approximate methods, radiation transport of lines and continua from their sites of creation to the observer is accounted for [176] [177] [178] [179]. Thorough discussions of photoionization codes and their applications can be found in [172] [180] [181] [182] [183].

7.1.1. The Ionization Parameter

The physical conditions in X-ray photoionized plasmas are, for a given ionizing spectrum, often described in terms the *ionization parameter* [184]. This quantity arises naturally from the steady-state equations of ionization equilibrium. Let β_i , C_i , and α_{i+1} denote the photoionization rate (s^{-1}) of charge state i , the collisional ionization rate coefficient ($\text{cm}^3 \text{s}^{-1}$) of i , and the recombination rate coefficient ($\text{cm}^3 \text{s}^{-1}$) of charge state $i + 1$, respectively. The term α_{i+1} accounts for all two-body recombination processes. Ignoring three-body recombination, as well as coupling to charge states more than one charge away, the steady state equations of ionization equilibrium can be written

$$[\beta_i + n_e C_i(T_e)] n_i = n_e \alpha_{i+1}(T_e) n_{i+1}, \quad (117)$$

where the rate coefficients for recombination and collisional ionization depend explicitly on the electron temperature T_e . In terms of the photoionization cross-section σ_i and ionization threshold energy χ_i of charge state i , the photoionization rate for a point source of ionizing continuum can be written as an integral over photon energy:

$$\beta_i = \frac{L_x}{r^2} \int_{\chi_i}^{\infty} dE \frac{S_E(E)}{4\pi E} \sigma_i(E), \quad (118)$$

where S_E is the spectral shape function, normalized on a suitable energy interval. Denoting the integral in Eq. (118) by Φ_i , Eq. (117) becomes

$$\frac{L_x}{n_e r^2} \Phi_i n_i + C_i(T_e) n_i = \alpha_{i+1}(T_e) n_{i+1}. \quad (119)$$

Let $\xi = L_x/n_e r^2$, which is called the *ionization parameter*. Then

$$\frac{n_{i+1}}{n_i} = \frac{C_i(T_e) + \xi \Phi_i}{\alpha_{i+1}(T_e)} \approx \frac{\xi \Phi_i}{\alpha_{i+1}(T_e)}, \quad (120)$$

where the second approximate equality applies for many cases of interest. Such a plasma, where the ionization and energetics are dominated by the influence of an X-ray field, is referred to as an *X-ray photoionized plasma*. More generally, when the source of X-ray illumination is not a point source,

$$\xi = \frac{4\pi F}{n} \quad (121)$$

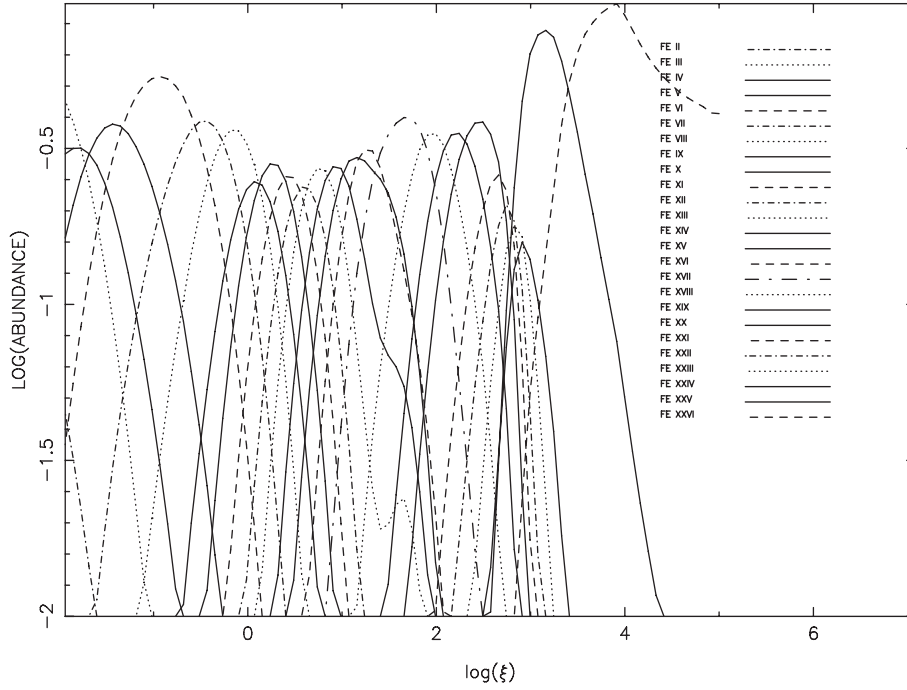


Fig. 17. Iron charge state distribution vs. ionization parameter. Figure from Kallman et al. [185].

where F is the energy-integrated, angle-averaged, ionizing flux, and n is the particle number density. There are other, related forms of the ionization parameter in use (e.g., [175]), but we will use ξ throughout. In terms of ξ , the photoionization rate corresponding to a single ionic cross-section is

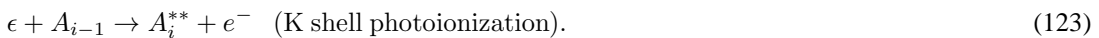
$$\beta_i = n\xi \int_{\chi_i}^{\infty} dE \frac{S_E(E)}{4\pi E} \sigma_i(E). \quad (122)$$

For the X-ray sources of interest, typical values of ξ range from approximately $1-10^4 \text{ erg cm s}^{-1}$. Since the energy equation and the equations of ionization balance are coupled, the output from the calculation of the physical state of a gas using a photoionization code gives both the temperature and the charge state distribution as a function of ξ . A pertinent example is given in Fig. (17), which shows the distribution in ξ of all 27 charge states of iron [185].

7.2. X-ray Fluorescence Lines

As discussed above, in accretion-powered X-ray sources, such as AGN and X-ray binaries, reprocessing of a hard X-ray continuum in relatively cool matter ($10^5 - 10^6 \text{ K}$) can generate intense iron K radiation from more neutral iron species of relatively low charge [83]. Iron fluorescence can be quite prominent, and, in fact, has long been known to constitute an essential component of disk spectra [186] [187].

The reprocessing mechanism, for any species with more than two bound electrons, begins with photoionization of a $1s$ electron by a photon with energy ϵ above the K edge, sending an element A in charge state $i - 1$ to charge state i , where i is in a quasi-bound state that is coupled to the continuum, denoted by the double asterisk below:



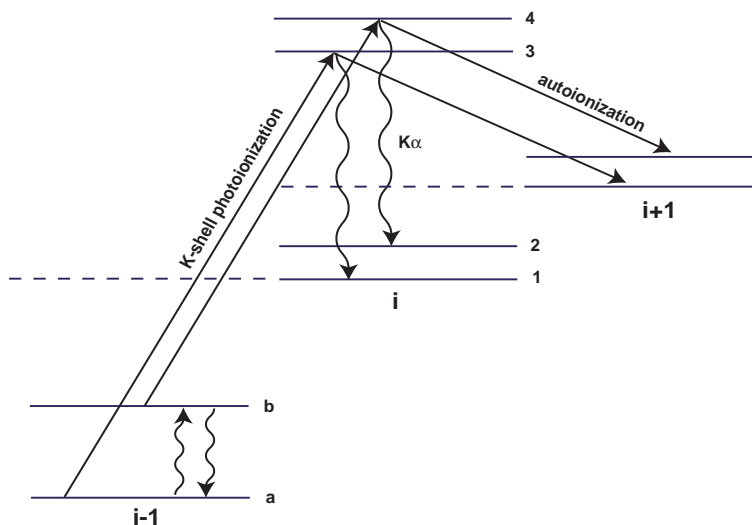


Fig. 18. Schematic of atomic processes involved in production of photoionization-driven K spectra. Three charge states, $i - 1$, i , and $i + 1$ are represented. Level 1 is the ground state of i , level 2 is an excited level, levels 3 and 4 are autoionizing, lying above the first ionization limit of i (dashed line). The low-lying level b in $i - 1$ is populated by photoexcitation from the ground level a , and decays radiatively back to a (wavy lines). (In the more general case, collisional excitation and de-excitation also affect the population distribution.) K-shell photoionization from levels a and b populates levels 3 and 4, respectively, which can decay radiatively by $K\alpha$ emission to levels 1 and 2, respectively. Alternatively, levels 3 and 4 can autoionize, leaving as products an Auger electron and ion $i + 1$. The relative intensities of $3 \rightarrow 1$ and $4 \rightarrow 2$ thus depend on the level population distribution in $1 - i$. The escape probabilities of these two lines depend on the level population distribution in i .

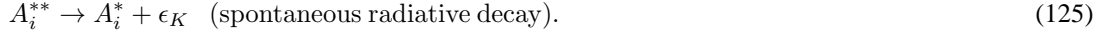
The intermediate state A_i^{**} , since it lies above the ionization threshold, has a non-vanishing $e^- - e^-$ Coulomb repulsion matrix element with a final product state, part of which consists of a continuum electron. Therefore, there is a non-vanishing probability assigned to the reaction



The ejection of an electron by this mechanism is called *autoionization*. The configuration or energy level associated with A_i^{**} is called an autoionizing configuration or autoionizing level, respectively. Referred to as the *Auger effect* for $1s$ vacancy states, autoionization is often the dominant decay route for the $1s$ -hole state. The reaction products are an *Auger electron*, i.e., an electron with a kinetic energy that is characteristic of the atomic energy level structure, and an ion in charge state $i + 1$, where, in this example, we assume for simplicity that $i + 1$ is left in its ground state. Still, it is worth mentioning that autoionization does not always leave a product ion in the ground state. It may be excited, and it can even be autoionizing. In the latter case, several charge states are coupled by autoionization; a single K-shell photoionization thus leads to a *vacancy cascade*, and must be accounted for when calculating the charge state distribution [188]. An extreme case relevant to astrophysics occurs for K-shell photoionization of neutral iron (Fe I), which initiates a vacancy cascade that can leave Fe X [189]. However, even in the simplest case described above ($A_{i-1} \rightarrow A_i \rightarrow A_{i+1}$), three charge states are coupled, and we see that the simple equations of ionization balance given in Eq. (117) need modification for actual calculations of the charge state distribution. This does not affect the definition of ξ given there, however.

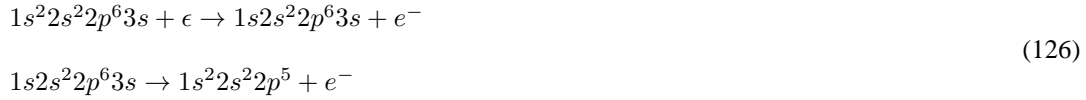
For iron, autoionization rates $\sim 10^{12} - 10^{14} \text{ s}^{-1}$ are typical. Competing with autoionization of the state A_i^{**} is spontaneous radiative decay. Radiative transition rates are of the same order of magnitude

as autoionization rates in iron, but are typically smaller by factors of a few. The case of highest probability involves a radiative transition that fills the K-shell hole. The line energy ϵ_K is characteristic of the atomic structure of the ion. We write the reaction as



The product ion A_i^* is indicated as being an excited level, although there are cases when it is a ground level. If the radiative transition leaves an ion in a state such that its energy lies below the first ionization potential, then that transition has led to *radiative stabilization* of the ion, i.e., the ion is no longer subject to autoionization. Parity-changing transitions of the type $np-1s$ are preferred over $nl-1s$, where $l \neq p$. Transitions filling the K-shell hole, if $n = 2$, are referred to as $K\alpha$ transitions, and if $n = 3$, $K\beta$ transitions. To make these concepts more concrete, we provide the following examples.

Example 1: 11-electron ion – autoionization



The first reaction generates a photoelectron, which heats the ambient plasma. The energy distribution of photoelectrons is continuous, and depends on the shape of the ionizing spectrum. The second reaction – autoionization – leaves the F-like ion in the ground level, and ejects an Auger electron.

Example 2: 11-electron ion – radiative stabilization by $K\alpha$ emission



The second step is a radiative stabilization of the autoionizing level, which produces a $K\alpha$ photon and leaves an excited Ne-like ion. The latter then decays by emission of a $3s \rightarrow 2p$ soft X-ray line. The end products are a Ne-like ground level, an Auger electron, one $K\alpha$ line, and one Ne-like $3s \rightarrow 2p$ line.

Natural line widths are $\approx 0.4 A_{14}$ eV, where A denotes the sum of radiative and autoionization transition rates from the autoionizing level of interest, and is given as a multiple of 10^{14} s^{-1} . For a line with energy ϵ , the thermal Doppler width is $\approx 0.4 (\epsilon/6.5 \text{ keV})(kT/100 \text{ eV})^{1/2}$ eV. Note that the low temperature is characteristic of X-ray photoionized plasmas. The commensurability of the natural line width and the thermal Doppler width for iron K fluorescent lines implies large Voigt parameters (see, for example, [73]). Estimates of line-center optical depths based on a pure Doppler profile will tend to provide an overestimate by factors of a few, as well as underestimate the contribution of the line opacity in the damping wings. The curve of growth is affected rather dramatically; the large Voigt parameter results in the virtual elimination of the saturation part of the curve, leaving a transition from the linear part to the damping part.

7.2.1. $K\beta$ Emission

While not as diagnostically useful as $K\alpha$ emission, the $K\beta$ complex has the potential to provide corollary information.

Example 3: 13-electron ion – $K\beta$ emission



Competing with $K\beta$ emission in the second step are autoionization and $K\alpha$ emission. There is a relatively small, but non-negligible, probability that a $K\beta$ photon is produced. Detailed calculations show that, for the near-neutral iron charge states, the $K\beta/K\alpha$ intensity ratio varies from about 0.12 (Fe II) to 0.15 (Fe IX) [190].

For most cases of interest, photoionization-driven $K\beta$ is important only when the pre-ionization charge state has an occupied $3p$ subshell in its ground configuration. To see this, we take as a counterexample, a N-like ion, with ground configuration $1s^2 2s^2 2p^3$. While, in principle, it is possible to create, say, C-like $1s 2s^2 2p^2 3p$ through K-shell photoionization from the N-like ground configuration, this mechanism is of interest only if there is a substantial population of the excited $1s^2 2s^2 2p^2 3p$ configuration, which is extremely unlikely, since the radiative lifetime of such an excited level is usually less than a nanosecond. Note also that it is not sufficient to have a populated $3s$ subshell in the ground configuration of the pre-ionization charge state. Decay by $K\beta$ $3s \rightarrow 1s$, because of the parity selection rule, is extremely improbable, since it competes with a much faster $2p \rightarrow 1s$ transition, as indicated in Example 2 above. Therefore, as a rule of thumb, $K\beta$ is emitted only by the iron ions Fe II – Fe XIV (singly-ionized through Al-like) if photoionization dominates the excitation.

One possible mechanism leading to $K\beta$ emission in charge states more ionized than Fe XIV involves direct photoexcitation by the same radiation field responsible for creating the charge state distribution [191]. Thus for a continuum photon of energy ϵ reactions such as $1s^2 2s^2 2p^2 + \epsilon \rightarrow 1s 2s^2 2p^2 3p$, a resonance absorption, followed by re-emission, can be efficient drivers of $K\beta$. Similarly, again using a C-like ion as an example, the entire Rydberg series of lines $1s 2s^2 2p^2 np \rightarrow 1s^2 2s^2 2p^2$ can be energized by resonance absorption of the continuum, so that $K\gamma$, $K\delta$, etc., may appear in a spectrum. Gauging the overall importance of such a mechanism involves radiation transport, thereby introducing macroscopic properties of the gas into the calculation, which is case specific. Generally, it is found that the efficacy with which photoexcitation competes with photoionization in driving line emission decreases with plasma column density [192]. However, velocity gradients can complicate the analysis [193].

7.2.2. Fluorescence Yield

The two-step process described above — inner-shell photoionization followed by radiative stabilization accompanied by emission of a K photon — is called *fluorescence*, possibly a misnomer, since the term applies also to other radiation processes. The *K fluorescence yield*, which we denote by Y_K , is the quotient of the rate at which K lines are generated from an irradiated sample and the rate at which K-shell holes are produced in the sample [194]. To motivate the concept of fluorescence yield, imagine a somewhat idealized laboratory experiment in which a beam of ions of element A interacts with a high-energy electron beam, say, in a crossed-beam setup. The electrons ionize the ions, increasing their charge by one step, and the beams are magnetically separated downstream of the interaction region. An experimenter counts the ionizations per unit time. Suppose also that an X-ray detector records the X-ray line production, and the ratio of X-ray count rate to ionization rate is recorded. A second run with the beam current increased by a factor of two shows that both the ionizations per second and the X-ray counts per second double. Next, an ion beam of a different element B is tested with the same setup. It is again found that the X-ray flux doubles when the ionization rate doubles. However, the ratio of X rays to ionizations is different for B . One draws the conclusion that the X-ray production is linearly proportional to the ionization rate, but that the constant of proportionality differs from element to element, and, possibly, from charge state to charge state for a given element. One infers that the proportionality constant Y is a characteristic of a given species and, specializing to K line emission, defines

$$Y_K = \text{probability of K line emission per K shell ionization.} \quad (129)$$

The usual convention is to associate a fluorescence yield with the pre-ionization charge state. For example, Fe II K lines are associated with an Fe I yield. This makes good sense, since there are cases where K lines from a given charge state arise from a photoionization of an ion several charge states removed. For example, Fe III line production may add to the Fe I fluorescence yield. We also distinguish emission from H-like and He-like ions from that of the lower charge states. In X-ray photoionized plasmas, emission from H- and He-like ions results predominantly from radiative recombination into excited levels. One *could* assign a fluorescence yield to a H-like ion by taking the ratio of H-like K lines produced per photoionization of the H-like ion, but that is actually somewhat at odds with the convention used for the lower charge states. In this paper, we assume that the fluorescence yield is defined for neutral atoms through Li-like ions.

In what follows, we show that the implication of Eq. (129) — that Y is an intrinsic atomic property — is false. For a set of energy levels u that lie above the ionization threshold, and a set of stabilized levels ℓ , all of which belong to charge state i (see Fig. 18), one starting point for deriving an explicit expression for the fluorescence yield is the emissivity, summed over all K lines of charge state i ,

$$j_K = \sum_u \sum_\ell n_{i,u} A_{u\ell}^r, \quad (130)$$

where we assume that transitions $u \rightarrow \ell$ are members of the $K\alpha$ complex in i . Level population densities of level u in charge state i are denoted $n_{i,u}$. Radiative transition rates are denoted by A^r . The summed K line emissivity has c.g.s. units $\text{cm}^{-3} \text{s}^{-1}$.

The level population density $n_{i,u}$ is found by dividing the population flux into level u by the total decay rate of the level,

$$n_{i,u} = \frac{\sum_k n_{i-1,k} \beta_{ku}}{\sum_j A_{uj}^r + \sum_m A_{um}^a}, \quad (131)$$

where A_{um}^a is an autoionization rate connecting level u in i to level m in $i+1$. Energy levels k in the pre-ionization charge state $i-1$ are represented as $n_{i-1,k}$. Photoionization connecting level k in $i-1$ to autoionizing levels u in i are denoted by β_{ku} , and are calculated according to Eq. (118).

Substituting Eq. (131) into Eq. (130) gives

$$j_K = \sum_k \sum_u \sum_\ell n_{i-1,k} \beta_{ku} \Gamma_{u\ell}, \quad (132)$$

where we define the *line fluorescence yield* $\Gamma_{u\ell}$ for each transition $u \rightarrow \ell$ by

$$\Gamma_{u\ell} = \frac{A_{u\ell}^r}{\sum_j A_{uj}^r + \sum_m A_{um}^a}. \quad (133)$$

The line fluorescence yield depends on purely atomic quantities, and can be thought of as a radiative branching ratio where additional sinks are included, viz., autoionization.

Now we “normalize” the emissivity by dividing it by the total photoionization rate, which gives an expression for the fluorescence yield,

$$Y_K = \frac{\sum_k \sum_u \sum_\ell n_{i-1,k} \beta_{ku} \Gamma_{u\ell}}{\sum_k \sum_u n_{i-1,k} \beta_{ku}}. \quad (134)$$

The yield $Y_{K\alpha}$ is thus a weighted average of the line fluorescence yields, where the weightings are determined by the level population distribution of charge state $i-1$ and the level-to-level photoionization rates, and should, in principle, be evaluated on a case-by-case basis, taking into account processes that affect the local excitation conditions. While complicated enough, note that Y_K does *not* depend on the

level population distributions of charge states i and $i + 1$, nor does it depend on the charge state distribution. We have added one further simplification, which is to ignore possible collisional redistribution of levels u , which is likely to be a valid assumption for most astrophysical densities.

The above derivation shows that a fluorescence yield cannot be considered as an intrinsic attribute of an atomic species, a fact that has been known for some time [195]. Equation (134) shows that Y_K depends on the level population distribution of $i - 1$, which depends in turn on the electron density, the electron temperature, and the local radiation field. Nevertheless, tables of yields exist, and are widely used in astrophysics [189] [196]. Part of the reason for this is that atomic calculations covering the wide range of conditions expected in astrophysical plasmas are scarce. Although this situation will change, in the meantime data based upon laboratory experiments, where fluorescence lines are used for the purposes of calibration, and “theoretical” data based upon approximation schemes, such as Z -scaling, continue to be used. Notwithstanding one’s possible expectations that yields vary dramatically, depending on the plasma conditions, detailed calculations of iron fluorescence [185] [197] show that numerical values of Y_K do not show substantial sensitivity to electron density between the low-density limit and the Maxwell-Boltzmann limit for the ions Fe II – Fe XVII. It is found that Y_K hovers around the “canonical” value of 0.34 for these ions. A variation is observed for higher charge states, however.

Since electric dipole radiative rates scale as Z^4 for $\Delta n > 0$ transitions, and since Auger rates are roughly constant with Z , Y_K increases rapidly with Z [198]. The trend of Y_K with Z , based upon both experimental data and calculations is shown in [199]. Among the elements currently relevant to cosmic X-ray spectroscopy, only nickel has a higher atomic number than iron, and the nickel abundance is at least an order of magnitude smaller than that of iron [200]. The relatively large iron fluorescence yields, coupled with its high abundance, conspire to make iron K fluorescence lines the most commonly observed in astrophysics. Calculations of disk reflection models have shown that fluorescence lines from the remaining cosmically abundant elements are relatively weak [201], and this is validated by the lack of detection in black hole accretion disk systems, although some (e.g., silicon K α) are observed in other source classes (e.g., [202]).

7.2.3. Energy Distribution of Iron K Lines

To date, spectrometers used to observe extrasolar X-ray sources have, at best, resolved the iron K α complex into three features: the Fe XXVI Ly α doublet at 6.97 keV, the Fe XXV blend, near 6.7 keV, and a blend of emission from a composite of lines from Fe II-Fe XVIII near 6.4 keV. For convenience, we refer to the 6.4 keV blend as arising in “near-neutral” material. The energy distribution of the iron K lines is shown in Fig. (19), from [185], where the potential for blending of the near-neutral lines is evident. Comparing adjacent charge states, the small energy spacings of lines from near-neutral iron arises from the fact that changes in the screening of the atomic potential experienced by $2p$ electrons are small compared to the K α line energies, i.e., the potential in the $n = 2$ shell is dominated by the nuclear charge to such an extent that screening by $n = 3$ electrons is of small consequence. The blending persists into the L shell. For example, in assessing the 5 eV energy separation of the K α line centroids⁸ of Ne-like Fe XVII and F-like Fe XVIII, note that the upper configurations are $1s2s^22p^63s$ and $1s2s^22p^6$, respectively. The small difference in centroid energies results from the small screening of the nuclear potential by the $3s$ electron in the Fe XVII $1s$ -hole state. Starting with O-like Fe XIX, the ion-to-ion K α centroid separations begin to increase. The removal of a $2p$ electron has a relatively large effect on the differential screening. For example, the K α energy centroids for Fe XVIII and Fe XIX are separated by 34 eV.

The most commonly observed fluorescence lines are those from near-neutral ions. Because of the blending and the small variation of line centroid energies, the entire complex is often referred to as

⁸ The centroid is defined as $\sum_i \epsilon_i j_i / \sum_i j_i$, where ϵ is a line energy, and j is an emissivity.

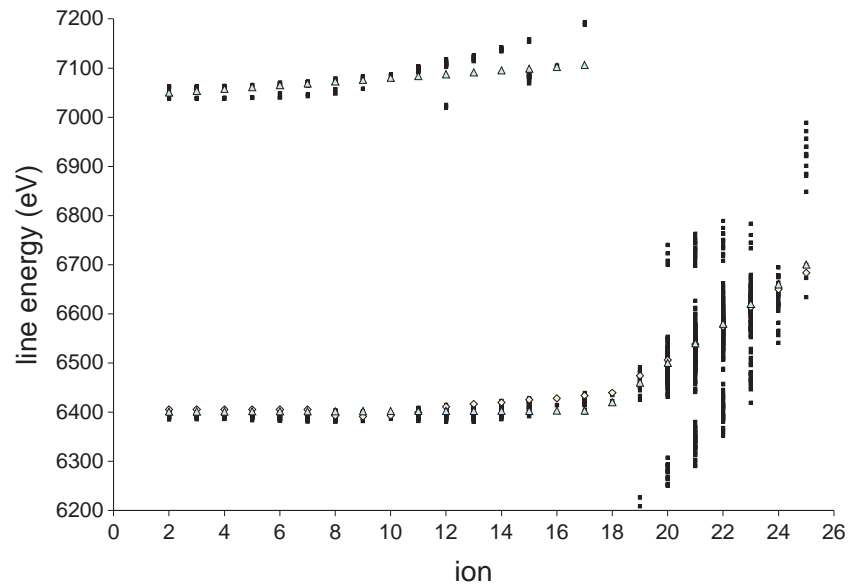


Fig. 19. Energy centroids for iron $K\alpha$ (lower) and $K\beta$ (upper.) Ordinate denotes the number of bound electrons in the emitting ion: ‘2’ for Fe II, etc. Figure from Kallman et al. [185].

“the iron line,” with the understanding the “line” is likely to be a composite structure. Reference to table values of line energies often contain separate entries for $K\alpha_1$ and $K\alpha_2$, which partially accounts for the intrinsic spectral structure. The distinction between these two features results from the relative probabilities of a $1s$ vacancy being filled by a radiative transition from an electron in the $2p_{3/2}$ subshell ($K\alpha_1$) or the $2p_{1/2}$ subshell ($K\alpha_2$). Thus $E(K\alpha_1) > E(K\alpha_2)$. Since there are four $2p_{3/2}$ electrons in a filled L shell, and two $2p_{1/2}$ electrons, the $K\alpha_1$ yield is generally given as twice the $K\alpha_2$ yield. However, even this greatly oversimplifies the K spectra from iron ions. In fact, the $K\alpha_1$ – $K\alpha_2$ labels are primarily an observational convenience (when they are spectrally resolved). When one accounts for the myriad possibilities introduced by angular momentum coupling, and the variety of possible excitation conditions encountered in astrophysical plasmas, the true spectrum may consist of hundreds of individual lines. In some cases the $K\alpha_1$ and $K\alpha_2$ line complexes overlap in energy.

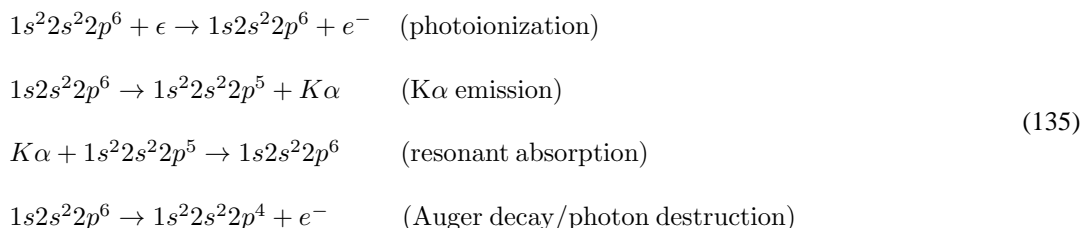
7.2.4. Resonant Auger Destruction

The blending of $K\alpha$ lines from near-neutral iron ions could be considered as both a blessing and a curse. On the one hand, the blending allows a simple approach to spectral fitting: simply add a line at or near 6.4 keV to the trial spectral model; no need to worry about a complex distribution of lines; no need to worry about the charge state distribution. On the other hand, blending means that while conditions in the disk plasma may vary considerably through the emitting region, for a large range of physical parameter space, these variations are not conveyed by the spectrum. In this latter context, then, one might look to the L-shell ions for potential diagnostics. The $K\alpha$ spectra of L-shell ions provide unique diagnostic information on plasmas that exist over intermediate ranges of ionization, as can be seen in Fig. 17. Interestingly, it appears that $K\alpha$ lines from iron L-shell ions are not required in spectral fits to black hole accretion disk spectra, even though there is ample evidence for emission from the charge states that bracket them. The absence of L-shell emission has been attributed to a process known as *resonant Auger destruction* [203] [204], a radiation transfer effect that leads to severe attenuation of K

emission lines from L-shell ions.

To see how resonant Auger destruction (RAD) selectively attenuates K emission from L-shell ions, as opposed to M-shell ions, consider the following example.

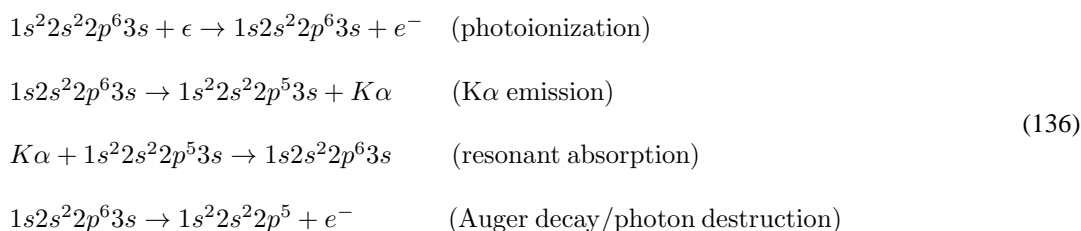
Example 4: 10-electron ion – resonant Auger destruction of $K\alpha$



The third step is the inverse of the second, where it is understood that the $K\alpha$ photon, somewhere along its line of flight, encounters an ion in the same state as the product ion that resulted from the original $K\alpha$ transition. The fourth step, autoionization, is, on average, more probable than radiative decay. Therefore, there is a high probability per scattering event that the photon will be destroyed. If the autoionizing ion in the fourth step decays radiatively instead, then, depending on the line optical depth of the medium, another absorption can occur, with an equally large destruction probability. The probability of the $K\alpha$ photon surviving more than just a few scatters is very small, and very few photons can escape the medium.

To make a distinction between L-shell ions and M-shell ions and their response to the RAD process, consider one more example.

Example 4: 11-electron ion – an improbable resonant Auger destruction of $K\alpha$



While this set of reactions is possible, it is generally unimportant, since the third step is extremely unlikely. For this step to operate effectively, the medium would require a high optical depth in the relevant excited level of the $1s^2 2s^2 2p^5 3s$ configuration. For the densities of interest, this will never be the case. By far, the dominant configuration of 10-electron ion is $1s^2 2s^2 2p^6$, and excitation channels to the $2p$ subshell are closed. This is also the case for the RAD sequence that begins with any ion that has $n = 3$ electrons in its ground configuration. Therefore, RAD has a negligible effect on M-shell ions, but a potentially major effect on L-shell ions.

Consider a semi-infinite slab that is irradiated from above by a hard X-ray continuum source. Only an upper layer of the slab corresponding roughly to unity line optical depth will contribute to $K\alpha$ fluorescence from L-shell ions. Below that depth, escape is prohibited by resonant Auger destruction. Compare this to the case of fluorescence from M-shell ions, where the fluorescing region for near-neutrals extends for roughly one continuum optical depth. This would suggest that the emergent $K\alpha$ line flux from L-shell ions is dwarfed by that from the near-neutrals. This provides a plausible explanation for the absence of an L-shell component in iron $K\alpha$ spectra. Moreover, in the context of spectral modeling of accretion disks, it appears to provide justification for simply zeroing out the $K\alpha$ emission for L-shell ions.

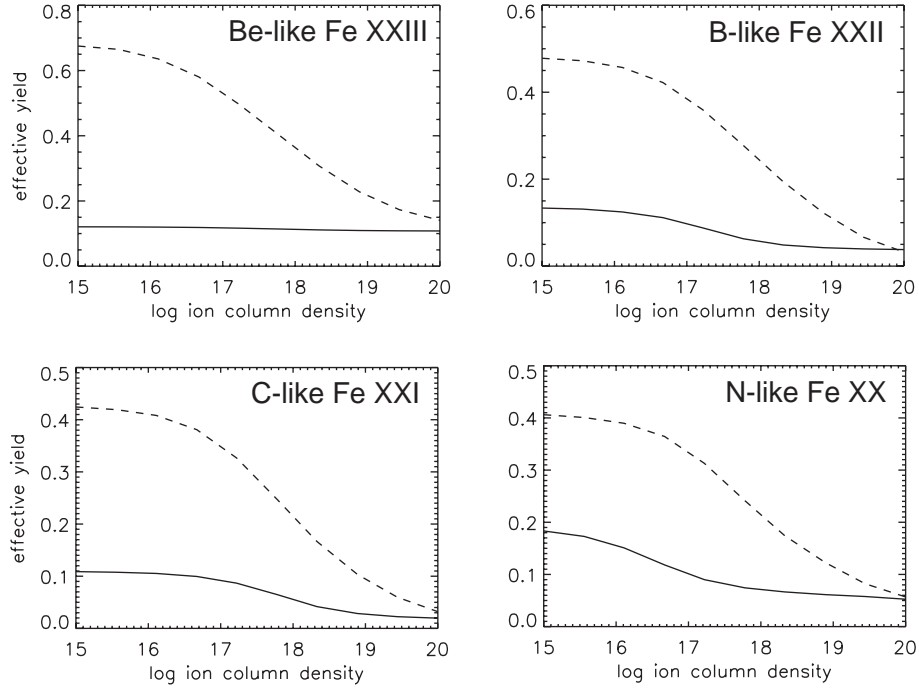


Fig. 20. Effective fluorescence yields as modified by resonant Auger destruction plotted against ionic column density for Fe XX – Fe XXIII. Each plot shows two cases: (*dotted line*) level populations of low-lying states driven by an 80 eV half-diluted blackbody and (*dashed line*) no perturbing radiation field. The fluorescence yield of N-like Fe XX is determined by the production and escape probability of C-like Fe XXI lines, etc.

This argument needs some modification, however. When we couch the argument only in terms of absorption cross-sections and ion column densities, we ignore the fact that the line optical depth depends on the level population of the lower level of the relevant transition, which need not be the ground state. For a given transition between an upper level u and a lower level ℓ , the line optical depth, in terms of the hydrogen column density N_{H} , the elemental abundance A_Z , and the ionic fraction F_{ion} , can be written

$$\tau_{\ell u} = N_{\text{H}} A_Z F_{\text{ion}} p_{\ell} \frac{\pi e^2}{mc} f_{\ell u} \phi(\nu) \quad (137)$$

where p_{ℓ} is the fractional population density of level ℓ , $f_{\ell u}$ is the absorption oscillator strength, and $\phi(\nu)$ is the line profile function in the rest frame of the absorber. Therefore, we must solve for the level populations p_{ℓ} for the lower levels of each $K\alpha$ transition. In fact, many $K\alpha$ transitions terminate on excited states, and such lines may be optically thin under certain conditions relevant to accretion disk atmospheres [205].

Given that the level population distribution in a charge state i partly determines the optical depth of $K\alpha$ lines from i , self-consistency demands that the set p_{ℓ} in charge state $i - 1$ also be calculated. The level populations of $i - 1$ determine the relative rates at which the upper levels of the $K\alpha$ transitions in i are populated by K-shell photoionization [185]. Referring back to the discussion in §7.2.2 concerning the effects of local excitation conditions on Y_K , this constitutes a second reason why assessments of RAD cannot be decoupled from microscopic considerations. It is shown in [205] that the level population distribution in $i - 1$, responding to an underlying UV/soft X-ray continuum, can significantly increase Y_K for N-like, C-like, B-like, and Be-like iron ions. If the definition of Y_K is modified so as

to account for the escape probability of $K\alpha$ lines from a medium of specified column density in charge state i , then a plot of Y_K^{eff} vs. N_i allows us to evaluate the overall effect of RAD, accounting for both microscopic and macroscopic influences. This is illustrated in Fig. (20), which shows that RAD is not decisively effective in quenching $K\alpha$ emission from L-shell ions until ionic column densities $\sim 10^{19}$ cm^{-2} are reached. Calculations of vertical structure in irradiated accretion disks suggest that, for these ions, this value is most likely on the high side of what is expected in typical disk atmospheres [206].

7.3. X-ray Reflection

The simplest assumption concerning vertical structure is to invoke a constant density, i.e., to forego a detailed consideration of the effect of the gravitational field entirely. Calculations of this type, while seemingly neglecting important physics, have nevertheless proven to be quite powerful in elucidating the physics of spectral formation in accretion disks [207] [208] [209]. With a choice for the incident flux, the local density dictates the ionization parameter. Transport of the incident radiation down through the atmosphere leads to its attenuation, which results in a stratification of ξ ($\partial\xi/\partial z$ is positive). Photoionization codes are then used to generate local spectra, which, accounting for opacity in the overlying layers, are propagated through the atmosphere to the computational boundary, the result being the spectral distribution of the radiation field at the “surface.” If desired, the effects of disk rotation, disk inclination, and relativistic effects are applied, thus generating a model spectrum as observed at infinity.

The first applications of constant-density models were focused on an examination of the “reflection” of the incident continuum from cold matter, “cold” in this context meaning that H and He were assumed to be fully stripped, while the remaining elements retained all of their electrons. A fraction of the radiation impinging on any gas will be re-radiated, or reflected, back into the general direction of the radiation source. This fraction is known as the *albedo*. More generally, one is interested in the energy dependence of the albedo. High-energy photons interacting with the cold material described above will either be absorbed via photoionization or Compton scattered.

A photoelectric cross-section falls roughly as E^{-3} above the photoionization threshold, or edge. Neutral iron has as its ground configuration $[\text{Ar}] 3d^6 4s^2$, where the notation $[\text{Ar}]$ symbolizes the configuration set of ground state Ar. With electrons occupying four shells, Fe I has associated with it an N ($n = 4$) edge, an M edge ($n = 3$), an L edge ($n = 2$), and a K edge ($n = 1$). The rapid falloff in the cross-sections results in the K edge dominating the total cross-section for energies above the 7.1 keV K edge. Competing with iron opacity is Compton scattering, with a small contribution from photoabsorption by the remaining elements. Although the iron K edge cross-section at threshold is orders of magnitude larger than the Compton cross-section, the fact that iron is a trace element (the solar abundance relative to hydrogen is 4.7×10^{-5} [200]) leads to a near equality in the opacities, so that Compton scattering is approximately as important as the iron photoelectric opacity at the iron K edge. A few keV above the iron K edge, Compton scattering becomes the dominant opacity source.

Since the typical energy lost by a photon in Compton scattering off of cold electrons is $\Delta E \approx E^2/mc^2$, not only do high-energy photons lose more energy than low-energy photons, but they lose a larger fractional energy $\Delta E/E$, as well. Compton scattering from a cold slab thus leads to a degradation in energy of the incident spectrum, high energy electrons migrating to lower energies, with a trend toward a steepening relative to the incident spectral shape. At the same time, however, a fraction of the photons near and below ~ 10 keV are absorbed, depleting the incident flux of soft X rays. The combined effect of these two processes produces the *Compton bump*, an apparent excess above an incident power-law spectrum in the approximate range 20–50 keV [18] [19] (see Fig. 21). Accompanying this signature of reflection are fluorescence lines [83] [210] (see below). The overall spectrum is a sum of the incident power-law and the reflection spectrum. The relative contribution of the reflection spectrum depends on the solid angle $\Delta\Omega$ that the reflector subtends at the hard X-ray source [211] [212]. For example, a disk geometry with illumination from above gives a *covering fraction* $\Delta\Omega/4\pi$ of about 1/2.

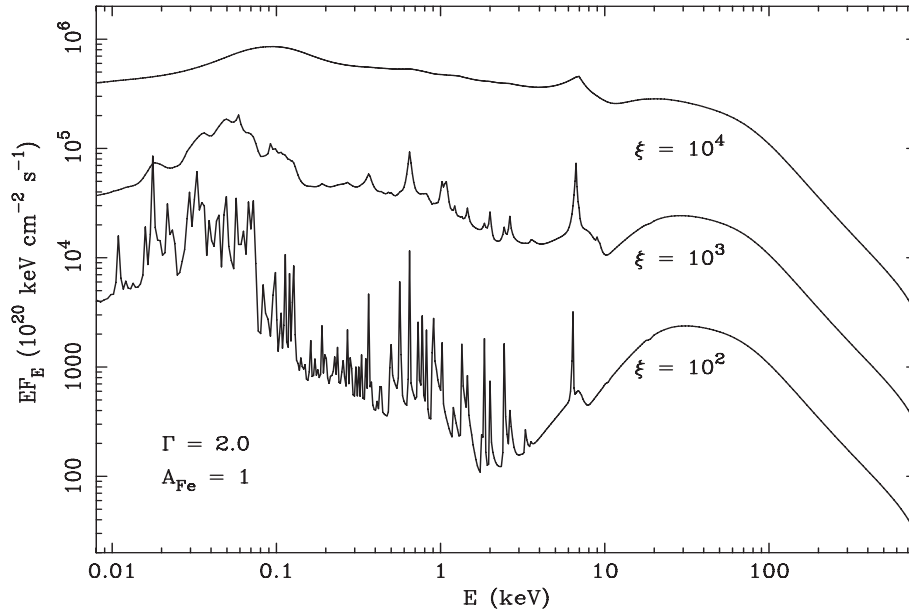


Fig. 21. Reflection spectra for constant-density slabs for three values of ξ (as labeled), assuming normal illumination by a power law spectrum with photon index 2. Electron density is set to 10^{15} cm^{-3} . The iron abundance is set to the solar value. From Ross and Fabian [179].

Some of the first serious attempts to model the vertical structure of hydrostatic accretion discs, including energy transport, opacity, and the equation of state, were applied to discs in cataclysmic variables [213] [214] [215]. These calculations made no provision for the influence of a hard X-ray source, however, and were not directly applicable to accreting neutron stars and black holes. Later developments saw the introduction of hydrostatic disk models for which the outer disk was assumed to be X-ray photoionized by a central source of illumination, appropriate to accreting neutron star X-ray binaries [216] [217] [218] [219].

A typical approach involves dividing the disk into a set of annuli, say, a few tens, then using a disk photoionization code to calculate the atmospheric structure of each annulus by integrating the equations of hydrostatic balance and 1-D radiation transfer for a slab geometry. A common alternative is to treat a single annulus. A hard X-ray radiation field, incident from above at some specified angle, is assumed for each radius. The spectral shape is usually taken directly from observations, rather than calculated self-consistently. A typical choice for the relative normalizations of the X-ray field at each annulus is to scale it by a r^{-3} power law. This is motivated by the picture described earlier wherein the hard X rays are supposed to originate from Compton scattering of the UV/soft X-ray disk field, which scales as the local dissipation rate in the optically thick disk (see Eq. 8). The overall normalization of the X-ray flux to the UV flux is an input parameter, and is typically of order unity. In particular, if a single annulus is modeled, this ratio is left to the discretion of the modeler, with the assumption that the disk is irradiated by a localized disk flare [206] [220]. The atmosphere is divided into a set of zones of (possibly) variable geometrical thickness. The absorption of the incident radiation field leads to heating through photoelectron thermalization and Compton heating. Photoelectron mean free paths are sufficiently small that the energy is deposited “on the spot.” A further constraint is that local thermal equilibrium must be satisfied, i.e., $\Lambda(P, \rho, F_\nu) = 0$, where the energy function depends on the gas pressure P , the density ρ and the local radiation field F_ν . The difference between heating and cooling Λ includes Compton scattering, bremsstrahlung cooling, photoionization heating, Auger heating,

collisional line cooling, and recombination cooling from H, He, C, N, O, Ne, Mg, Si, S, Ar, Ca, Fe, and Ni ions. Photoionization produces spectral by-products, as well, such as fluorescence lines, radiative recombination continua, and lines produced in recombination cascades. This reprocessed radiation contributes to the “diffuse” flux, which is added to the modified incident field, and is propagated upwards and downwards to the adjacent computational cells. Boundary conditions at the top and bottom of the annulus are also prescribed. One choice [79] is to set the density at the bottom to the value given by the α -disk model, and to set the gas temperature at the top to the Compton temperature [73], given by the following integral over the radiation spectrum:

$$kT_c = (4U)^{-1} \int_0^\infty d\epsilon \epsilon U_\epsilon, \quad (138)$$

where U_ϵ is the specific radiation energy density and U is the total radiation energy density. The Compton temperature for most cases of interest is $\sim 10^7$ - 10^8 K.

For modeling X-ray line emission from the disk atmosphere, the commonly used assumptions of LTE and the diffusion approximation may not be valid. The assumption of constant density may be invalid, as well, since the hydrostatic equilibration time scale is small or comparable to other relevant timescales (cf., [69]). For calculating the discrete emission line content of a disk spectral model, particularly recombination emission, the vertical ionization structure and the density stratification are crucial. By contrast, the output iron fluorescence energy centroid varies little until the ionization reaches the L shell (see Fig. 18). Still, even fluorescence emission can be affected by a Compton thick, fully ionized gas overlying the emission sites deeper in the atmosphere [222]. Also, over certain ranges of ξ , the gas is subject to a thermal instability that can lead to a steep transition between cold near-neutral gas and hot highly-ionized gas [222] [223].

Examples of output from a set of reflection slab models are shown in Fig. (21) [179]. In these examples, the gas density is fixed at a constant value, and the slab is irradiated from above by a continuum flux with spectral shape $AE^{-1} \exp(-E/300 \text{ keV})$. The value of ξ is varied by varying the normalization A . As described in [179], the reflection spectrum for the largest value of ξ (10^4) is nearly line-free, since the gas is very highly ionized. Compton broadened emission from Fe XXXV and Fe XXVI make the only conspicuous discrete contribution to the spectrum. At the two lower values of ξ the increasingly complex line spectra, with contributions from $n = 2 \rightarrow n = 1$ transitions of H-like and He-like ions of C, N, O, Ne, Mg, Si, S, and a few $n = 3 \rightarrow n = 2$ Fe L-shell lines, are attributed to the progressively lower level of ionization.

7.3.1. Thermal Instability

X-ray irradiated gas is subject to a thermal instability in the 10^5 - 10^6 K temperature range [224] [225], suppressing X-ray line emission in that regime. Application of the Field stability criterion [226] indicates that a photoionized gas may become unstable when recombination cooling of H-like and He-like ions is important. The T and ξ ranges where the instability occurs depend on the metal abundances and the local radiation spectrum [227], and, from the theoretical point of view, depends on the atomic rates used [228]. Within a range of *pressure ionization parameters* [175] $\Xi = P_{\text{rad}}/P_{\text{gas}}$, where P_{rad} is the radiation pressure, thermal equilibrium is achieved by three distinct temperatures, only two of which are stable to perturbations in temperature. Physically, the instability causes a steep temperature gradient as the gas is forced to “move” between thermally stable regimes, requiring the formation of a transition region joining the hot and cold phases whose size could be determined by thermal conduction. The method by which the thermal instability is treated can significantly affect the predicted spectrum [79]. One issue relevant to iron K fluorescence emission is that the steep transition region may comprise the iron L-shell ions. Therefore, even if the effects of RAD were nil, iron L-shell ions may have insufficient optical depth to contribute substantially to the overall iron K spectrum.

7.3.2. Alternative X-ray Signatures of Relativistic Effects

Prior to the launch of *Chandra* and *XMM-Newton*, the soft X-ray spectrum (~ 1 keV) was generally modeled as a power-law attenuated by an ionized absorber [230] – the *warm absorber* model. A radical departure from this model was suggested in [231], where it was proposed that spectral features observed in the 5–35 Å band of the Seyfert 1 galaxies MCG–6-30-15 and Mrk 766 could be explained as relativistically broadened emission lines from H-like carbon, nitrogen, and oxygen. Fitting parameters – disk inclination, disk emissivity profile – were found to be roughly consistent with those found for the iron $K\alpha$ line [27]. An analysis of a 130 ks grating observation with *XMM-Newton* of Mrk 766 [232] led to the conclusion that a relativistic line interpretation provides a better fit to the data than the warm absorber model. A similar conclusion was found for the Seyfert 1 galaxy NGC 4051 [233]. If correct, these spectral features, formed by radiative recombination onto bare nuclei, could provide additional “handles” that would allow tighter constraints to be placed on models of the accretion disk structure in the relativistic regime. Since the sites of formation H-like lines are spatially distinct from the formation sites of fluorescence lines a broader range of parameter space would be accessible.

Still, numerous absorption lines from ionized species in the *Chandra* grating spectrum of MCG–6-30-15, also noted in [231], indicated at least some influence from a warm absorber. In fact, the relativistic disk interpretation in its entirety was disputed in [234]. In the model proposed there, absorption in addition to two warm absorber components is provided by a dust component containing FeO_2 , which is embedded in the warm absorber. The warm absorber model found additional support from theoretical disk models, which showed that the line equivalent widths required by the relativistic disk interpretation far exceeded theoretical predictions [221]. An additional problem is the high nitrogen to oxygen ratio required to account for the N VII feature, although a Bowen-like mechanism has been suggested as an explanation [235]. A further criticism of the relativistic disk line model is that reflection models predict emission from iron L-shell ions [221] that is not observed in the data. Radiation transport calculations using a Monte Carlo approach indicate no strong iron $L n \rightarrow 2$ emission, however [178].

In subsequent work [236] it was argued that the warm absorber model used in the *Chandra* interpretation of MCG–6-30-15 does not adequately describe the *XMM* Reflection Grating Spectrometer data, which has a better response at longer wavelengths. Further analysis [237] of the *XMM* data of MCG–6-30-15 showed that fits obtained with a composite model, involving both relativistic disk lines and a warm absorber, yield ambiguous results; if a warm absorber is added to the best-fitting disk line model, then relatively little absorption is required; if relativistic lines are added to the best-fitting warm absorber model, then only weak emission lines are required. Given the potential importance of relativistic recombination line emission, there is hope that these issues will be resolved decisively in the near future.

Another class of relativistic signatures has been proposed recently. The magnetic flare model [239] of the hot corona and hard X-ray continuum observed in accretion disks posits the existence of many small-scale, hot ($T > 10^8$ K) magnetic loops. Following loop emergence, Compton cooling of loop material, through the interaction with softer disk photons, results in hard X-ray flaring events. Disk irradiation by these relatively localized flares produce fluorescence emission that is concentrated in the region of the disk near the flare [238]. In other words, regions of the disk that are small in both radial and azimuthal extent, and which radiate intense transient fluorescence emission are predicted by this model. The transiently fluorescing region will continue to orbit the black hole, and will emit iron lines that are narrow compared to the case of full disk irradiation. The centroid energy is determined by the gravitational redshift associated with a small range of annuli, and by the Doppler effect appropriate to the instantaneous projected velocities over a narrow range of azimuth. If the lifetime of such a region is sufficiently long, the centroid energy could be observed to change over the time scale of an observation. It has been shown how the line flux received from such a “hot spot” changes with position along the orbit, owing to the effects of relativistic beaming and light bending [240]. Narrow spectral

features lying at energies below 6.4 keV have indeed been reported, e.g., [162] [241] [242]. As pointed out in [243], however, inferring disk parameters from these kinds of data push the limits of current observational capabilities.

8. Concluding Remarks

The theory of accretion onto black holes has been in development for at least thirty years. Owing to the complex physics governing accretion, it is probably safe to predict that decades of additional research will be required before the theory is considered complete. Answers to outstanding questions concerning accretion onto black holes will not come without access to better data, and lie beyond the capabilities of current instrumentation. The current generation of X-ray observatories, *Chandra* and *XMM-Newton* are helping to identify the various avenues of inquiry [244] that will motivate future observations with, for example, NASA's planned *Constellation-X* mission and ESA's planned *XEUS* mission.

In the meantime, on the theoretical side, referring back to Shapiro and Teukolsky's quote in §1, an attack on the full inhomogeneous, non-axisymmetric, time-dependent, relativistic accretion disk problem with coupled radiative transfer is not far beyond the horizon. In any case, it seems evident that disk reflection models, with their emphasis on radiation flow, and MHD simulations, with their emphasis on time-dependent gas flow, will need to be merged at some point in the not-too-distant future.

Einstein developed the General Theory of Relativity at a time when it was not demanded by astronomical observations. Only Einstein's physical intuition demanded it. From Schwarzschild's solution, to the theory of stellar collapse, to the quasar model, to the discovery of Cyg X-1, to the supermassive black hole at the Galactic center, to the identification of relativistically modified X-ray emission lines, we now find that General Relativity is fully acknowledged to be an indispensable component of the various theoretical formalisms used to describe black hole astrophysics. One wonders if Einstein's skepticism regarding the existence of black holes would have remained intact in light of the current weight of evidence.

In addition to the special and general relativity theories, Einstein's Nobel prize winning work on the photoelectric effect, his introduction of the A and B coefficients, his advances in statistical mechanics, his influence on de Broglie, Schrodinger, and Dirac, and many other of his contributions to theoretical physics, figure prominently in modern research on the topics discussed in this paper.

Acknowledgements

We thank Gordon Drake and Peter Beiersdorfer for their advice and encouragement. Our appreciation to Chris Mauche, whose careful reading of the text led to improvements in the overall presentation. Thanks also to Rob Fender, Mario Jimenez-Garate, Tim Kallman, Ben Mathiesen, Paul Nandra, Martin Pessah, Randy Ross, and Masao Sako for contributions. An anonymous referee contributed several helpful suggestions. Work at LLNL was performed under the auspices of the U.S. Department of Energy by the University of California Lawrence Livermore National Laboratory under contract No. W-7405-Eng-48.

References

1. A. Pais, *Subtle is the Lord* (Oxford University Press; 1982).
2. R. Giacconi, H. Gursky, F.R. Paolini, and B.B. Rossi, *Phys. Rev. Lett.* **9**, 439 (1962).
3. M. Schmidt, *Nature* **197**, 1040 (1963).
4. A. Hewish, S.J. Bell, J.D.H. Pilkington, P.F. Scott, and R.A. Collins, *Nature* **217**, 709 (1968).
5. M. Nauenberg and G.J. Chapline, *Ap. J.* **179**, 277 (1973).
6. C.E. Rhoades and R. Ruffini, *Phys. Rev. Lett.* **32**, 324 (1974).

7. I.D. Novikov, in *Theory of Black Hole Accretion Disks*, eds., M.A. Abramowicz, G. Bjornsson, and J.E. Pringle (Cambridge University Press), p. 41 (1998).
8. C.W. Allen, *Astrophysical Quantities, Second Edition* (The Athlone Press, University of London; 1963).
9. A.C. Fabian, W.N. Brandt, R.G. McMahon, and I.M. Hook, *M.N.R.A.S.* **291**, L5 (1997).
10. S.L. Shapiro and S.A. Teukolsky, *Black Holes, White Dwarfs, and Neutron Stars* (John Wiley and Sons; 1983).
11. M. Elvis, et al., *M.N.R.A.S.* **183**, 129 (1978).
12. M. Oda, P. Gorenstein, H. Gursky, E. Kellogg, E. Schreier, H. Tananbaum, and R. Giacconi, *Ap. J.* **166**, L1 (1971).
13. M. van der Klis, in *X-Ray Binaries*, ed., W.H.G. Lewin, J. van Paradijs, and E.P.J. van den Heuvel (Cambridge University Press: Cambridge), p. 252 (1995).
14. H. Kuneida, T.J. Turner, H. Awaki, K. Koyama, R.F. Mushotzky, and Y. Tsusaka, *Nature* **345**, 786 (1990).
15. R.F. Mushotzky, et al., *Ap. J.* **235**, 377 (1980).
16. N.E. White, *Adv. Space Res.* **3**, 9 (1984).
17. M.M. Basko, *Ap. J.* **223**, 268 (1978).
18. P.W. Guilbert and M.J. Rees, *M.N.R.A.S.* **233**, 475 (1988).
19. A.P. Lightman and T.R. White, *Ap. J.* **233**, 57 (1988).
20. K. Nandra, in *X-ray Astronomy: Stellar Endpoints, AGN, and the Diffuse X-ray Background*, eds., N. White, G. Malaguti, and G. Palumbo (American Institute of Physics), p. 264 (2001).
21. A.C. Fabian, M.J. Rees, L. Stella, and N.E. White, *M.N.R.A.S.* **238**, 729 (1989).
22. K. Chen, J.P. Halpern, and A.V. Filippenko, *Ap. J.* **339**, 742 (1989).
23. P. Barr, N.E. White, and C.G. Page, *M.N.R.A.S.* **216**, 65 (1985).
24. H. van der Woerd, N.E. White, and S.M. Kahn, *Ap. J.* **344**, 320 (1989).
25. T.R. Kallman and N.E. White, *Ap. J.* **341**, 955 (1989).
26. Y. Tanaka, et al., *Nature* **375**, 659 (1995).
27. K. Nandra, I.M. George, R.F. Mushotzky, T.J. Turner, and T. Yaqoob, *Ap. J.* **477**, 602 (1997).
28. R.F. Mushotzky, C. Done, and K.A. Pounds, *ARA&A* **31**, 717 (1993).
29. M. Elvis, *Ap. J.* **545**, 63 (2000).
30. L. Titarchuk, D. Kazanas, and P.A. Becker, *Ap. J.* **598**, 411 (2003).
31. M. van der Klis, *Ann. Rev. Astron. Astrophys.* **38**, 717 (2001).
32. J. McClintock and R.A. Remillard, in *Compact Stellar X-ray Sources*, eds., W.H.G. Lewin and M. van der Klis (Cambridge University Press; 2003).
33. A.C. Fabian, K. Iwasawa, C.S. Reynolds, and A.J. Young, *P.A.S.P.* **112**, 1145 (2000).
34. C.S. Reynolds and M.A. Nowak, *Phys. Rep.* **377**, Issue 6, 389 (2003).
35. J.R. Oppenheimer and G.M. Volkoff, *Phys. Rev.* **55**, 374 (1939).
36. J.R. Oppenheimer and H. Snyder, *Phys. Rev.* **56**, 455 (1939).
37. F. Hoyle and R.A. Lyttleton, *Proc. Camb. Phil. Soc.* **35**, 405 (1939).
38. A. Treves, L. Maraschi, and M. Abramowicz, *Accretion: A Collection of Influential Papers* (World Scientific Publishing Co. Pte. Ltd; 1989).
39. J. Frank, A. King, and D. Raine, *Accretion Power in Astrophysics, Second Edition*, (Cambridge: Cambridge University Press; 1992).
40. O. Blaes, in *Accretion Disks, Jets, and High Energy Phenomena in Astrophysics*, ed., V. Beskin, et al., Les Houches Summer School, **78**, 137 (2004).
41. K. Davidson and J.P. Ostriker, *Ap. J.* **179**, 585 (1973).
42. S.L. Shapiro, *Ap. J.* **180**, 531 (1973).
43. V.F. Shvartsman, *Soviet Astr.* **15**, 37 (1971).
44. P. Meszaros, *A&A* **44**, 59 (1975).
45. S.H. Lubow and F.H. Shu, *Ap. J.* **198**, 383 (1975).
46. F. Verbunt and E.P.J. van den Heuvel, in *X-Ray Binaries*, ed., W.H.G. Lewin, J. van Paradijs, and E.P.J. van den Heuvel (Cambridge University Press: Cambridge), p. 457 (1995).
47. R.P. Kraft, *Ap. J.* **135**, 408 (1961).
48. J.E. Pringle and M.J. Rees, *A&A* **21**, 1 (1972).
49. N.I. Shakura and R.A. Sunyaev, *A&A* **24**, 337 (1973).

50. M.A. Abramowicz, B. Czerny, J.-P. Lasota, and E. Szuszkiewicz, *Ap. J.*, **332**, 646 (1988).
51. X. Chen and R.E. Taam, *Ap. J.* **412**, 254 (1993).
52. C. Luo and E.P. Liang, *Ap. J.* **498**, 307 (1998).
53. S. Ichimaru, *Ap. J.* **214**, 840 (1977).
54. R. Narayan and I. Yi, *Ap. J.* **452**, 710 (1995).
55. Y. Tanaka and W.H.G. Lewin, in *X-Ray Binaries*, ed., W.H.G. Lewin, J. van Paradijs, and E.P.J. van den Heuvel (Cambridge University Press: Cambridge), p. 126 (1995).
56. Y. Tanaka and N. Shibazaki, *ARA&A*, **34**, 607 (1996).
57. R.D. Blandford and M.C. Begelman, *M.N.R.A.S.* **303**, 1 (1999).
58. E. Quataert, E. and A. Gruzinov, *Ap. J.* **539**, 809 (2000).
59. M.A. Malkan, *Ap. J.* **268**, 582 (1983).
60. J.H. Krolik, in *Theory of Black Hole Accretion Disks*, ed. M.A. Abramowicz, G. Bjornsson, and J.E. Pringle (Cambridge University Press), p. 134 (1998).
61. X. Chen, M.A. Abramowicz, J. Lasota, R. Narayan, and I. Yi, *Ap. J.*, **443**, L61 (1995).
62. S.A. Balbus and J.F. Hawley, *Rev. Mod. Phys.* **70**, 1 (1998).
63. J.F. Hawley, C.F. Gammie, and S.A. Balbus, *Ap. J.* **440**, 742 (1995).
64. G.A. Shields, *Nature* **272**, 706 (1978).
65. M.A. Malkan and W.L.W. Sargent, *Ap. J.* **254**, 22 (1982).
66. M. Elvis, et al., *Ap. J. Suppl.*, **95**, 1 (1994).
67. B. Czerny and M. Elvis, *Ap. J.* **321**, 305 (1987).
68. N.E. White, L. Stella, and A.N. Parmar, *Ap. J.* **324**, 363 (1988).
69. R.R. Ross, A.C. Fabian, and S. Minshige, *M.N.R.A.S.* **258**, 189 (1992).
70. L. Maraschi and S. Molendi, *Ap. J.* **353**, 452 (1990).
71. J. Poutanen, J.H. Krolik, and F. Ryde, *M.N.R.A.S.*, **292**, L21 (1997).
72. A.S. Kompaneets, *Soviet Physics JETP* **4**, 730 (1957).
73. G.B. Rybicki and A.P. Lightman, *Radiative Processes in Astrophysics* (Wiley-Interscience; 1979).
74. P.J.E. Peebles, *Principles of Physical Cosmology* (Princeton University Press; 1993).
75. G.S. Bistnovatyii-Kogan, Y.B. Zeldovich, and R.A. Sunyaev, *Sov. Astron. AJ* **15**, 17 (1971).
76. A.A. Zdziarski, *Ap. J.* **289**, 514 (1985).
77. R. Svensson, in *Radiation Hydrodynamics in Stars and Compact Objects*, IAU Coll. No. 89, eds. D. Mihalas and K.-H. Winkler (Springer-Verlag), p. 325 (1986).
78. G. Ghisellini and F. Haardt, *Ap. J.* **429**, L53 (1994).
79. M.A. Jimenez-Garate, J.C. Raymond, D.A. Liedahl, and C.J. Hailey, *Ap. J.* **558**, 448 (2001).
80. D.A. Liedahl, in *X-Ray Spectroscopy in Astrophysics*, eds J. van Paradijs and J. Bleeker, Springer Lecture Notes in Physics, p. 189 (1999).
81. M.A. Bautista, T.R. Kallman, L. Angelini, D.A. Liedahl, and D.P. Smits, *Ap. J.* **509**, 848 (1998).
82. J.B. Kingdon and G.J. Ferland, *Ap. J.* **516**, L107.
83. I.M. George and A.C. Fabian, *M.N.R.A.S.* **249**, 352 (1991).
84. Q.Z. Liu, J. van Paradijs, and E.P.J. van den Heuvel, *A&A Suppl.* **147**, 25 (2000).
85. Q.Z. Liu, J. van Paradijs, and E.P.J. van den Heuvel, *A&A* **368**, 1021 (2000).
86. P. Charles, in *Theory of Black Hole Accretion Disks*, ed. M.A. Abramowicz, G. Bjornsson, and J.E. Pringle (Cambridge University Press), p. 1 (1998).
87. C.T. Bolton, *Nature*, **235**, 271 (1972).
88. E.P.J. van den Heuvel, in *ESA, Environment Observation and Climate Modelling Through International Space Projects* (SEE N93-2387808-88), (1992).
89. G.E. Brown and H.A. Bethe, *Ap. J.* **423**, 659 (1994).
90. F.X. Timmes, S.E. Woosley, and T.A. Weaver, *Ap. J.* **457**, 834 (1996).
91. E. Agol, M. Kamionkowski, L.V.E. Koopmans, and R.D. Blandford, *Ap. J.* **576**, L131 (2002).
92. M.R. Garcia, J.E. McClintock, R. Narayan, P. Callanan, D. Barret, and S.S. Murray, *Ap. J.* **553**, 47 (2001).
93. A.M. Stirling, et al., *M.N.R.A.S.*, **327**, 1273 (2001).
94. R.P. Fender, *M.N.R.A.S.* **322**, 377 (2001).
95. G.E. Romero, M.M. Kaufman Bernadó, and I.F. Mirabel, *A&A*, **393**, L61 (2002).
96. D.F. Torres, G.E. Romero, J.A. Combi, P. Benaglia, H. Andernach, and B. Punsly, *A&A* **370**, 468

- (2001).
97. D.F. Torres, G.E. Romero, X. Barcons, and Y. Lu, *Ap. J.*, in press, astro-ph/0503186 (2005).
 98. J.B. Dove, J. Wilms, M. Maisack, and M.C. Begelman, *Ap. J.*, **487**, 759 (1997).
 99. A.A. Esin, J.E. McClintock, and R. Narayan, *Ap. J.*, **489**, 865 (1997).
 100. A.A. Esin, R. Narayan, W. Cui, J.E. Grove, and S. Zhang, *Ap. J.*, **505**, 854 (1998).
 101. R.P. Fender, T.M. Belloni, and E. Gallo, *M.N.R.A.S.* **335**, 1105 (2004).
 102. J.M. Miller, et al., *Ap. J.*, **578**, 348 (2002).
 103. A. Martocchia, et al., *A&A* **387**, 215 (2002).
 104. J.M. Miller, et al., *Ap. J.* **577**, L15 (2002).
 105. J.M. Miller, et al., *Ap. J.* **570**, L69 (2002).
 106. J.H. Krolik, *AGN: From the Central Black Hole to the Galactic Environment* (Princeton University Press; 1999).
 107. L. Woltjer, in *Active Galactic Nuclei – Saas-Fee Advanced Course 20*, eds., T.J.-L. Courvoisier and M. Mayor (Springer-Verlag), p. 1 (1990).
 108. R. Antonucci, *Ann. Rev. Astron. Astrophys.* **31**, 473 (1993).
 109. H. Netzer, in *Active Galactic Nuclei - Saas-Fee Advanced Course 20*, eds., T.J.-L. Courvoisier and M. Mayor (Springer-Verlag), p. 57 (1990).
 110. R.F. Mushotzky, in *New Visions of the X-ray Universe*, astr-ph/0203310 (2002).
 111. R.F. Mushotzky, L.L. Cowie, A.J. Barger, and K.A. Arnaud, *Nature* **404**, 459 (2000).
 112. G. Hasinger, et al., *A&A* **365**, 45 (2001).
 113. M. Miyoshi, J. Moran, J. Herrnstein, L. Greenhill, N. Nakai, P. Diamond, and M. Inoue, *Nature* **373**, 127 (1995).
 114. L. Ferrarese L. and H. Ford, *Space Science Reviews* **116**, 523 (2005).
 115. J. Magorrián, et al., *A.J.* **115**, 2285 (1998).
 116. J. Kormendy and K. Gebhardt, in *20th Texas Symposium on Relativistic Astrophysics*, AIP Conference Proceedings, Vol. 586, ed., J.C. Wheeler, p. 363 (2001).
 117. F. Melia and H. Falcke, *Ann. Rev. Astron. Astrophys.* **39**, 309 (2001).
 118. R. Schodel, et al., *Nature* **419**, 694 (2002).
 119. A.M. Ghez, *Ap. J.* **586**, L127 (2003).
 120. A.M. Ghez, S. Salim, S.D. Hornstein, A. Tanner, M. Morris, E.E. Becklin, and G. Duchene, *Ap. J.* **620**, 744 (2005).
 121. D.F. Torres, S. Capozziello, and G. Lambiase, *Phys. Rev.* **D62**, 104012 (2000).
 122. J. Kormendy and D. Richstone, *Ann. Rev. Astron. Astrophys.* **33**, 581 (1995).
 123. J. Wilms, C.S. Reynolds, M.C. Begelman, J. Reeves, S. Molendi, R. Staubert, and E. Kendziorra, *M.N.R.A.S.* **328**, L27 (2001).
 124. A.C. Fabian, et al., *M.N.R.A.S.* **335**, L1 (2002).
 125. K.O. Mason, G. Branduardi-Raymont, P.M. Ogle, M.J. Page, E.M. Puchnarewicz, and N.J. Salvi, *Adv. Space Res.* **34**, 2610 (2004).
 126. K. Nandra, I.M. George, R.F. Mushotzky, T.J. Turner, and T. Yaqoob, *Ap. J.* **523**, L17 (1999).
 127. C.S. Reynolds, in *Probing the Physics of Active Galactic Nuclei*, ASP Conference Proceedings, Vol. 224, eds., B.M. Peterson, R.W. Pogge, and R.S. Polidan, p. 105 (2001).
 128. I.F. Mirabel, et al., *Nature* **358**, 215 (1992).
 129. I.F. Mirabel and L.F. Rodriguez, *Nature* **392**, 673 (1998).
 130. R.P. Fender and T. Maccarone, in *Cosmic Gamma-ray Sources*, eds., K.S. Cheng, et al., p. 205 (2003).
 131. B.J. Sams, A. Eckart, and R. Sunyaev, *Nature* **392**, 673 (1998).
 132. M. Rees, *Nature* **211**, 468 (1966).
 133. I.F. Mirabel, *A&A* **330**, L9 (1998).
 134. H. van der Laan, *Nature* **211**, 1131 (1966).
 135. A.P. Marscher et al., *Nature* **417**, 625 (2002).
 136. C.M. Miller and E.J.M. Colbert, *International Journal of Modern Physics D* **13**, 1 (2004).
 137. S. Weinberg, *Gravitation and Cosmology* (John Wiley and Sons; 1972).
 138. B.F. Schutz, *A First Course in General Relativity* (Cambridge University Press; 1985).
 139. L. Stella, *Nature* **344**, 747 (1990).
 140. A.J. Young, R.R. Ross, and A.C. Fabian, *M.N.R.A.S.* **300**, L11 (1998).

141. C.S. Reynolds, A.J. Young, M.C. Begelman, and A.C. Fabian, *Ap. J.* **514**, 164 (1999).
142. J.C. Lee, A.C. Fabian, C.S. Reynolds, W.N. Brandt, and K. Iwasawa, *M.N.R.A.S.* **318**, 857 (2000).
143. J. Chiang, et al., *Ap. J.* **528**, 292 (2000).
144. C.S. Reynolds, *Ap. J.* **533**, 811 (2000).
145. G. Miniutti and A.C. Fabian, *M.N.R.A.S.* **349**, 1435 (2004).
146. J.M. Bardeen, W.H. Press, and S.A. Teukolsky, *Ap. J.* **178**, 347 (1972).
147. J.M. Bardeen, *Nature* **226**, 64 (1970).
148. R.P. Kerr, *Phys. Rev. Lett.* **11**, 237 (1963).
149. K.S. Thorne, *Black Holes and Time Warps: Einstein's Outrageous Legacy* (W.W. Norton and Company; 1994).
150. R.H. Boyer and R.W. Lindquist, *J. Math. Phys.* **8**, 265 (1967).
151. K.S. Thorne, *Ap. J.* **191**, 507 (1974).
152. E.F. Taylor and J.A. Wheeler, *Exploring Black Holes: Introduction to General Relativity* (Addison Wesley Longman; 2000).
153. R. Penrose, *Riv. Nuovo Cimento*, **1**, 252 (1969).
154. I. Ciufolini and E.C. Pavlis, *Nature* **431**, 958 (2004).
155. I.D. Novikov and K.S. Thorne, in *Black Holes*, ed., C. DeWitt and B. DeWitt (Gordon and Breach: New York; 1972).
156. A.P. Lightman, W.H. Press, R.H. Price, and S.A. Teukolsky, *Problem Book in Relativity and Gravitation* (Princeton University Press; 1975).
157. B. Aschenbach, *A&A* **425**, 1075 (2004).
158. A. Laor, *Ap. J.* **376**, 90 (1991).
159. K.A. Arnaud, in *Astronomical Data Analysis Software and Systems V*, ASP Conf. Ser. Vol. 101, p. 17, eds., G.H. Jacoby and J. Barnes (1996).
160. J.C. Houck, *High Resolution X-ray Spectroscopy with XMM-Newton and Chandra*, ed., G. Branduardi-Raymont, published electronically and stored on CD (2002).
161. K. Iwasawa, et al., *M.N.R.A.S.* **282**, 1038 (1996).
162. K. Iwasawa, A.C. Fabian, A.J. Young, H. Inoue, and C. Matsumoto, *M.N.R.A.S.* **306**, L19 (1999).
163. Y. Dabrowski, A.C. Fabian, K. Iwasawa, A.N. Lasenby, and C.S. Reynolds, *M.N.R.A.S.* **288**, L11 (1997).
164. C.S. Reynolds and M.C. Begelman, *Ap. J.* **488**, 109 (1997).
165. J.H. Krolik and J.F. Hawley, *Ap. J.* **573**, 754 (2002).
166. K. Rauch and R.D. Blandford, *Ap. J.* **421**, 46 (1994).
167. K. Beckwith and C. Done, *M.N.R.A.S.* **352**, 353 (2004).
168. M. Dovciak, V. Karas, and T. Yaqoob, *Ap. J. Suppl.* **153**, 205 (2004).
169. L.-X. Li, E.R. Zimmerman, R. Narayan, and J.E. McClintock, *Ap. J. Suppl.* **157**, 335 (2005).
170. C.W. Misner, K.S. Thorne, and J.A. Wheeler, *Gravitation* (W.H. Freeman and Co., San Francisco; 1973).
171. A.C. Fabian, et al., *M.N.R.A.S.* **277**, L11 (1995).
172. G.J. Ferland, K.T. Korista, D.A. Verner, J.W. Ferguson, J.B. Kingdon, and E.M. Verner, *P.A.S.P.* **110**, 761 (1998).
173. T.R. Kallman and J.H. Krolik, XSTAR v1.43, HEASARC (NASA/GSFC), Greenbelt, MD (1999).
174. J.H. Krolik and T.R. Kallman, *Ap. J.*, **286**, 366 (1984).
175. J.K. Krolik, C.F. McKee, and C.B. Tarter, *Ap. J.* **249**, 422 (1981).
176. I. Hubeny, in *Spectroscopic Challenges of Photoionized Plasmas*, ASP Conference Series, Vol. 197, p. 175, eds., G. Ferland and D. Savin (2001).
177. A.-M. Dumont and S. Collin, in *Spectroscopic Challenges of Photoionized Plasmas*, ASP Conference Series, Vol. 197, p. 231, eds., G. Ferland and D. Savin (2001).
178. C.W. Mauche, D.A. Liedahl, B.F. Mathiesen, M.A. Jimenez-Garate, and J.C. Raymond, *Ap. J.* **606**, 168 (2004).
179. R.R. Ross and A.C. Fabian, *M.N.R.A.S.* **358**, 211 (2005).
180. K. Davidson and H. Netzer, *Rev. Mod. Phys.* **51**, 715 (1979).
181. J.P. Halpern and J.E. Grindlay, *Ap. J.* **242**, 1041 (1980).
182. T.R. Kallman and R. McCray, *Ap. J. Suppl.* **50**, 263 (1982).
183. T.R. Kallman, in *Spectroscopic Challenges of Photoionized Plasmas*, ASP Conference Series, Vol. 247,

- p. 175, eds., G. Ferland and D. Savin (2001).
184. C.B. Tarter, W. Tucker, and E.E. Salpeter, *Ap. J.* **156**, 943 (1969).
185. T.R. Kallman, P. Palmeri, M. Bautista, C. Mendoza, and J.H. Krolik, *Ap. J. Suppl.* **155**, 675 (2004).
186. K.A. Nandra, K.A. Pounds, G.C. Stewart, A.C. Fabian, and M.J. Rees, *M.N.R.A.S.* **236**, 39 (1989).
187. M. Matsuoka, L. Piro, M. Yamauchi, and T. Murakami, *Ap. J.* **361**, 440 (1990).
188. J.C. Weisheit, *Ap. J.* **190**, 735 (1974).
189. J.S. Kaastra and R. Mewe, *A&A Suppl.* **97**, 443 (1993).
190. P. Palmeri, C. Mendoza, T.R. Kallman, M.A. Bautista, and M. Melendez, *A&A* **410**, 359 (2003).
191. D.A. Liedahl, *Atomic Data for X-ray Astronomy*, 25th Meeting of the IAU, Joint Discussion 17, 22 July 2003, Sydney, in press (2005).
192. A. Kinkhabwala, et al., *Ap. J.* **575**, 732 (2002).
193. P.S. Wojdowski, D.A. Liedahl, M. Sako, S.M. Kahn, and F. Paerels, *Ap. J.* **582**, 959 (2003).
194. W. Bambynek, et al., *Rev. Mod. Phys.* **44**, 716 (1972).
195. V.L. Jacobs, G.A. Doschek, J.F. Seely, and R.D. Cowan, *Phys. Rev. A* **39**, 2411 (1989).
196. L.L. House, *Ap. J. Suppl.* **155**, 21 (1969).
197. P. Palmeri, C. Mendoza, T.R. Kallman, and M.A. Bautista, *A&A* **403**, 1175 (2003).
198. R.D. Cowan, *The Theory of Atomic Structure* (Berkeley, Los Angeles, London: University of California Press), p. 589 (1981).
199. M.O. Krause, *J. Phys. Chem. Ref. Data* **8**, 307 (1979).
200. E. Anders and N. Grevesse, *Geochimica et Cosmochimica Acta* **53**, 197 (1989).
201. G. Matt, A.C. Fabian, and C.S. Reynolds, *M.N.R.A.S.* **289**, 175 (1997).
202. M. Sako, D.A. Liedahl, S.M. Kahn, and F. Paerels, *Ap. J.* **525**, 921 (1999).
203. R.R. Ross, A.C. Fabian, and W.N. Brandt, *M.N.R.A.S.* **278**, 1082 (1996).
204. D.L. Band, R.I. Klein, J.I. Castor, and J.K. Nash, *Ap. J.* **362**, 90 (1990).
205. D.A. Liedahl, in *X-ray Diagnostics of Astrophysical Plasmas*, ed., R.K. Smith, (American Institute of Physics), p. 99 (2005).
206. S. Nayakshin and T.R. Kallman, *Ap. J.* **546**, 406 (2001).
207. R.R. Ross and A.C. Fabian, *M.N.R.A.S.* **261**, 74 (1993).
208. G. Matt, A.C. Fabian, and R.R. Ross, *M.N.R.A.S.* **262**, 179 (1993).
209. P.T. Zycki, J.H. Krolik, A.A. Zdziarski, and T.R. Kallman, *Ap. J.* **437**, 597 (1994).
210. K.A. Pounds, K. Nandra, G.C. Stewart, I.M. George, and A.C. Fabian, *Nature* **344**, 132 (1990).
211. G. Matt, G.C. Perola, and L. Piro, *A&A* **245**, 75 (1991).
212. G. Matt, G.C. Perola, L. Piro, and L. Stella, *A&A* **257**, 63 (1992).
213. F. Meyer and E. Meyer-Hofmeister, *A&A* **106**, 34 (1982).
214. S. Mineshige and Y. Osaki, *P.A.S.J.* **35**, 377 (1983).
215. J.K. Canizzo and J.C. Wheeler, *Ap. J. Suppl.* **40**, 1 (1984).
216. Y.-K. Ko and T.R. Kallman, *Ap. J.* **374**, 721 (1991).
217. Y.-K. Ko and T.R. Kallman, *Ap. J.* **431**, 273 (1994).
218. J.C. Raymond, *Ap. J.* **412**, 267 (1993).
219. A. Rozanska and B. Czerny, *Acta Astronomica* **46**, 233 (1996).
220. D.R. Ballantyne and R.R. Ross, *M.N.R.A.S.* **332**, 777 (2002).
221. D.R. Ballantyne, R.R. Ross, and A.C. Fabian, *M.N.R.A.S.* **336**, 867 (2002).
222. S. Nayakshin, D. Kazanas, and T.R. Kallman, *Ap. J.* **537**, 83 (2000).
223. M.A. Jimenez-Garate, J.C. Raymond, and D.A. Liedahl, *Ap. J.* **581**, 1297 (2002).
224. J. Buff and R. McCray, *Ap. J.* **189**, 147 (1974).
225. G.B. Field, D.W. Goldsmith, and H.J. Habing, *Ap. J.* **155**, L149 (1969).
226. G.B. Field, *Ap. J.* **142**, 531 (1965).
227. C.J. Hess, S.M. Kahn, and F.B.S. Paerels, *Ap. J.* **478**, 94 (1997).
228. D.W. Savin, et al., *Ap. J. Suppl.* **123**, 687 (1999).
229. G. Matt, A.C. Fabian, and R.R. Ross, *M.N.R.A.S.* **280**, 823 (1996).
230. J.P. Halpern, *Ap. J.* **281**, 90 (1984).
231. G. Branduardi-Raymont, M. Sako, S.M. Kahn, A.C. Brinkman, J.S. Kaastra, and M.J. Page, *A&A* **365**, L140 (2001).
232. K.O. Mason, et al., *Ap. J.* **582**, 95 (2003).

233. P.M. Ogle, K.O. Mason, M.J. Page, N.J. Salvi, F.A. Cordova, I.M. McHardy, and W.C. Priedhorsky, *Ap. J.* **606**, 151 (2004).
234. J.C. Lee. et al., *Ap. J.* **554**, L13 (2001).
235. M. Sako, *Ap. J.* **594**, 1108 (2003).
236. M. Sako, et al., *Ap. J.* **596**, 114 (2003).
237. A.K. Turner, A.C. Fabian, S. Vaughan, and J.C. Lee, *M.N.R.A.S.* **346**, 833 (2003).
238. S. Nayakshin and D. Kazanas, *Ap. J.* **553**, L141 (2001).
239. A.A. Galeev, R. Rosner, and G.S. Vaiana, *Ap. J.* **229**, 318 (1979).
240. M. Dovciak, S. Bianchi, M. Guainazzi, V. Karas, and G. Matt, *M.N.R.A.S.* **350**, 745 (2004).
241. T.J. Turner, et al., *Ap. J.* **574**, L123 (2002).
242. T. Yaqoob, I.M. George, T.R. Kallman, U. Padmanabhan, K.A. Weaver, and T.J. Turner, *Ap. J.* **596**, 85 (2003).
243. K. Iwasawa, G. Miniutti, and A.C. Fabian, *M.N.R.A.S.* **355**, 1073 (2004).
244. F.B.S. Paerels and S.M. Kahn, *ARA&A* **41**, 291 (2003).